[American Journal of Science, Vol. 321, January-February, 2021, P. 235–296, DOI 10.2475/01.2021.07]

UNRAVELLING THE *P-T*-t HISTORY OF THREE HIGH-GRADE METAMORPHIC EVENTS IN THE EPUPA COMPLEX, NW NAMIBIA: IMPLICATIONS FOR THE PALEOPROTEROZOIC TO MESOPROTEROZOIC EVOLUTION OF THE CONGO CRATON

SÖNKE BRANDT*,†, REINER KLEMD*, HANQIANG XIE**, and PATRICK BOBEK*

ABSTRACT. **The Epupa Complex of northern Namibia constitutes the south-western margin of the Archean Congo Craton of central Africa. We present new petrological and geochronological data for metasedimentary migmatites that decode the poorly-known Paleoproterozoic to Mesoproterozoic evolution of this remote part of the craton. Detrital magmatic zircons with concordant $^{207}Pb/^{206}Pb$ ages between 1898 and 1774 Ma are interpreted to demonstrate the formation of the metasedimentary protoliths through reworking of Paleoproterozoic granitoids of a magmatic arc in a back-arc basin. SHRIMP U-Pb zircon analyses of metamorphic rims around the detrital grains linked with constraints from pseudosection modelling revealed three distinct high-grade metamorphic events in the migmatites. Late Paleoproterozoic regional HT-LP metamorphism between 1740 and 1720 Ma constitutes the oldest event and only affected the rocks of the northernmost part of the Epupa Complex (Eyao Unit). Heating to mid-amphibolite facies peak *P-T* conditions of 720 °C and 4 kbar caused the partial replacement of early biotite-sillimanite by garnet-cordierite assemblages during melt-producing reactions in metapelites. The near-isobaric heating-cooling *P-T* paths and the high geothermal gradient (60 °C/km) are consistent with HP-LP metamorphism in a back-arc basin setting with up-rising basic melt as heat source. Early Mesoproterozoic (1530 Ma) HT-LP metamorphism is recorded by rare Mg-rich Opx-Crd rocks that are restricted to the westernmost part of the Eyao Unit. Near-isobaric *P-T* paths culminate at granulite facies peak-conditions of 830 °C and 2 kbar. This local HP-LP event is interpreted to record contact metamorphism related to the coeval emplacement of early-Mesoproterozoic granitoids or the emplacement of intimately associated gabbros. Metapelitic Grt-Bt-Sil migmatites record the third high-grade metamorphic event that was active at *ca.* 1330 Ma and is restricted to the southern part of the Epupa Complex (Orue Unit). Sillimanite pseudomorphs after kyanite and late cordierite coronas around garnet indicate a clockwise *P-T* path during regional upper-amphibolite facies metamorphism that peaks at lower crustal conditions of 770 °C and 7.5 kbar. The clockwise *P-T* path is interpreted to reflect crustal thickening through magmatic accretion of basic melts that produced the coeval Kunene Intrusive Complex, the largest massif-type anorthosite in the world.**

The metamorphic events detected in the migmatites record a change of the geotectonic position of the Epupa Complex from a convergent continental margin during the late Paleoproterozoic to an intracratonic position in the Mesoproterozoic. The migmatites of the Eyao Unit were affected by an intense hydrothermal alteration during the Pan-African orogeny (*ca.* 520 Ma) that also caused the partial re-setting of the U-Pb zircon isotope system.

Key words: Epupa Complex, Congo Craton, pseudosections, P-T-t path, migmatite, Paleoproterozoic, amphibolite facies, HT-LP metamorphism

* GeoZentrum Nordbayern, Friedrich-Alexander-Universität (FAU) Erlangen-Nürnberg, Schlossgarten 5, 91054 Erlangen, Germany

** Beijing SHRIMP Centre, Institute of Geology, Chinese Academy of Geological Sciences, 26 Baiwanzhuang Road, 100037 Beijing, China

† Corresponding author: soenke.brandt@fau.de; Tel: +49 09131 85 26071; Fax +49 9131 85-23734

INTRODUCTION

Metamorphic rocks that underwent (ultra)high-temperature-low-pressure ((U)HT-LP) metamorphism are an important component of mobile belts worldwide throughout Archean to Phanerozoic times. Temperatures and pressures of (U)HT-LP metamorphism are generally in the range 500 to 1150 °C and 2 to 7 kbar, respectively, and metamorphic thermal gradients reported for regions of HT-LP metamorphism are > 150°C/kbar (De Yoreo and others, 1991; Kelsey and Hand, 2015). Such high thermal gradients require extra heat input by magmatism. However, the tectonic regimes and heat sources related to (U)HT-LP metamorphism are often controversial (for example, Clark and others, 2011; Drüppel and others, 2013; Kelsey and Hand, 2015; Bial and others, 2015; He and others, 2018; Jung and others, 2019). Discrimination between the various possible tectonic settings in which HT-LP metamorphism can be generated, including extensional settings such as mid-ocean ridges, back arc basins, and continental rifts as well as convergent plate margins, continent-continent collision zones, magmatic arcs, and accretionary wedges (for example, De Yoreo and others, 1991; Zheng and Chen, 2017), requires the determination of precise *P-T-t-* paths and the detection of associated heat sources.

In this study, we focus on the evolution of metapelitic Grt-Crd and Grt-Bt-Sil migmatites, and restitic Opx-Crd rocks from the Epupa Complex in northern Namibia. The Epupa Complex constitutes the south-western continental margin of the Archean Congo Craton of central Africa and was affected by Mesoproterozoic UHT metamorphism (1520–1450 Ma, Seth and others, 2003), and by younger upper-amphibolite facies metamorphism (1370–1310 Ma, Seth and others, 2003) in its southern part (fig. 1A). Both high-grade metamorphic events are interpreted to be related to the two-stage emplacement of the anorthositic Kunene Intrusive Complex (KIC) (Brandt and others, 2003, 2007; Brandt and Klemd 2008), the largest anorthosite massif in the world, with anorthosite emplacement at *ca.* 1500 Ma (Bybee and others, 2019), and between 1385 ± 25 and 1319 ± 13 Ma (Mayer and others, 2004; Drüppel and others, 2007). Granitic orthogneisses and metagabbros, exposed along the Kunene River in the northern part of the Epupa Complex (fig. 1A), yielded Paleoproterozoic emplacement ages of 1836 to 1783 Ma (Kröner and others, 2015), and migmatitic paragneisses contain detrital zircons with concordant Pb^{207}/Pb^{207} ages between 2075 and 1820 Ma. Contacts between orthogneisses and paragneisses are not exposed, but assuming that the metasediments were intruded by the granitic protoliths of the orthogneisses, Kröner and others (2015) suggested deposition of the sediments at *ca.* 1800 Ma, broadly synchronous with granitoid emplacement. Although metamorphic zircon had not been not studied, Kröner and others (2015) suggested that the metasediments, metagranitoids, and metagabbros were probably affected by the same *ca.* 1760 Ma deformation and migmatization event, which was detected for metagranitoids from the Etengwa area in the southern part of the Epupa Complex (Kröner and others, 2010; fig. 1).

To characterize this assumed Paleoproterozoic event, we deciphered the *P-T-t* history of Grt-Crd migmatites and associated high-grade metasediments of the northern part of the Epupa Complex that were apparently intruded by the granitoids. *In-situ* zircon SHRIMP dating was used to determine the timing of high-grade metamorphism and partial melting. The age data were linked with the *P-T* paths of high-grade metamorphism that were reconstructed by integrating textural observations, mineral chemical and geothermobarometric data with a series of calculated phase diagrams in the MnNCKFMASHTO system. To elucidate a possible poly-metamorphic evolution we also studied samples from the southern part of the Epupa Complex that were thought to record both Paleoproterozoic and Mesoproterozoic metamorphic zircon. The results of the study will contribute to a better understanding

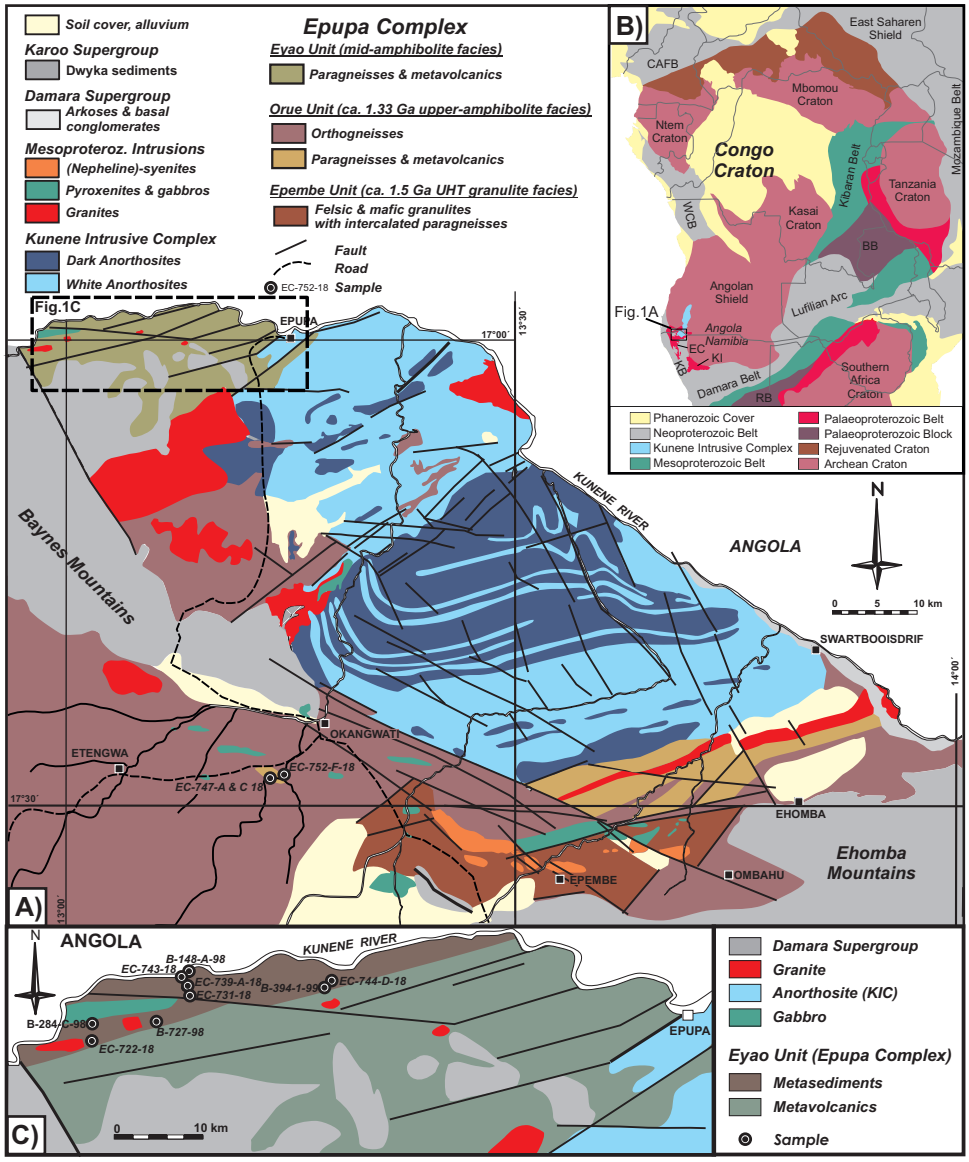

Fig. 1. (A) Simplified geological map of the Epupa Complex in the study area (modified after Köstlin, ms, 1967; Menge, 1998; Brandt and others, 2003; Brandt and Klemd, 2008) showing the tectonic units of the Epupa Complex in the study area (upper-amphibolite facies Orue Unit, UHT granulite facies Epembe Unit and granulite facies Eyao Unit and the location of the samples from the Orue Unit. (B) Precambrian tectonic framework of south-central Africa showing the exposed shield areas of the Congo Craton (Kasai Craton, Angolan Shield, Ntem Craton and Mbomou Craton), which were once joined with the Saõ Francisco Craton of Brazil (modified from Jelsma, and others, 2018). The Epupa Complex is situated at the south-western margin of the Congo Craton. (KB: Kaoko Belt, EC: Epupa Complex, KI: Kamanjab Inlier, BB: Bangweulu Block, RB: Rehoboth Block, WCB: West Congo Belt, CAFB: Central African Fold Belt). (C) Detailed geological map of the Eyao Unit (see fig. 1A for location of the map) showing the localities of the samples studied by EPMA and/or SHRIMP zircon dating.

of the, so far poorly known, Paleoproterozoic evolution of the south-western part of the Congo Craton and highlight the geodynamic significance of (U)HT-LP metamorphism.

GEOLOGICAL SETTING

Together with the Kamanjab and Grootfontein Inliers, the Epupa Complex of north-western Namibia constitutes a Paleoproterozoic belt at the south-western continental margin of the Angolan Shield, the southern segment of the Archean Congo Craton of central Africa (Jelsma and others, 2018; fig. 1B). Granitic orthogneisses with emplacement ages of 1860 to 1760 Ma dominate both, the Epupa Complex and the Kamanjab inlier (Kröner and others, 2010, 2015; Kleinhanns and others, 2015). The calc-alkaline composition of the granitoid protoliths of the Epupa Complex suggest their formation in a Cordilleran-type active continental margin environment (Kröner and others, 2015). Granitoid emplacement was almost immediately followed at *ca.* 1760 Ma by high-grade metamorphism and anatexis that was documented for meta-granitoids exposed west of Okangwati (Kröner and others, 2010). The data document that the south-western margin of the Angolan shield was involved in the Eburnean Orogeny (*ca.* 2000 ± 200 Ma, Cahen and others, 1984) whose geodynamic significance in the Congo Craton remains largely unknown, because large regions of southern Angola and northern Namibia are geologically still unexplored. The high-grade metamorphic Epupa Complex rocks were intruded by anorthosites of the Kunene Intrusive Complex (fig. 1A), the largest anorthosite complex in the world (Ashwal and Twist, 1994). The two generations of anorthosites show no evidence of a tectono-metamorphic overprint (Drüppel and others, 2001): younger 'Dark Anorthosites' intruded older 'White Anorthosites'. Recently, a 1500 Ma age was detected for anorthosites of the Angolan part of the KIC (Bybee and others, 2019) that is probably related to the emplacement of the White Anorthosites. Emplacement of the Dark Anorthosite is significantly younger and lasted from 1385 Ma (1385 ± 25 Ma and 1385 ± 7 Ma U–Pb zircon ages from Namibia; Drüppel and others, 2007) and Angola (McCourt and others, 2013) to 1319 ± 28 Ma, as defined by a Sm–Nd mineral bulk-rock age that marks the end of anorthosite activity (Mayer and others, 2004). Anorthosite magmatism was associated with the intrusion of undeformed gabbros and *ca.* 1375 Ma granitoids (Red Granites; Mayer and others, 2004; Drüppel and others, 2007). In the late Neoproterozoic, the western margin of the Epupa Complex was affected by the Pan-African orogeny and partially incorporated into the NNW–SSE-trending Kaoko Belt (for example, Trompette, 1994; fig. 1B). In the eastern part, comprising the study area, unmetamorphosed Neoproterozoic sediments of the Damara Supergroup unconformably overlie the Epupa Complex rocks.

The Epupa Complex rocks exposed south of the KIC were affected by two discrete Mesoproterozoic high-grade metamorphic events (fig. 1A): Granulites of the Epembe Unit were affected by early Mesoproterozoic (1520–1450 Ma, Seth and others, 2003) UHT metamorphism with peak metamorphic conditions of ~ 970 °C at ~ 9.5 kbar (Brandt and others, 2003, 2007). Mid-Mesoproterozoic (1370–1310 Ma, Seth and others, 2005) upper-amphibolite facies metamorphism with conditions of 700 to 750 °C at 5.5 to 6.7 kbar caused widespread migmatization in the rocks of the Orue Unit (Brandt and Klemd, 2008). Similar temperatures of 750 °C but lower pressures of 4.5 kbar were detected for a strongly altered Grt-Crd migmatite from a volcano-sedimentary sequence that is exposed along the Kunene River in the northern part of the Epupa Complex (Brandt and Klemd, 2008). However, emplacement ages between 1835 and 1760 Ma for granitoids apparently intruding the gneisses and migmatites suggest that the rocks of the volcano-sedimentary sequence were affected by a pre-1835 Ma high-grade metamorphic event in this area (Kröner and others, 2015). Evidence for a Mesoproterozoic overprint, as documented for the Epupa rocks exposed south of the KIC, is absent. Therefore, we define the volcano-sedimentary sequence exposed for about 30 km along the Kunene as a discrete rock unit in the

Epupa Complex, termed the Eyao Unit. The sequence continues into Angola where it is named Schist-Quartzite-Amphibolite Complex in the western part and Gneiss-Migmatite-Granite Complex in the eastern part (De Carvalho and others, 2000).

Field relationships.—The Eyao Unit is composed of interlayered mafic and felsic gneisses in the southern to south-eastern part whereas migmatitic metasediments dominate the northern to north-western part (fig. 1C). Undeformed Neoproterozoic sediments of the Damara Supergroup cover the rocks of the Eyao Unit to the south (fig. 1C). Several WNW-ESW trending mylonitic faults and a major broadly E-W trending, subvertical, dextral strike-slip mylonitic fault, transect the volcano-metasedimentary sequence. Granitic orthogneisses with Paleoproterozoic emplacement ages occur in both sequences and were usually affected by extensive migmatization. Intrusive contacts between the metagranitoids and the metasediments were not observed. In the westernmost part of the Eyao Unit a large (6 km in length) gabbro complex intruded the volcano-metasedimentary sequence. In addition, undeformed granites intruded the volcano-sedimentary sequence and the orthogneisses, and crosscut the foliation of the gneisses and migmatites. Paragneiss xenoliths in the granites document the intrusive character of the granites (fig. 2A). Similar granites exposed downstream along the Kunene River yielded 1530 to 1520 Ma emplacement ages (Kröner and others, 2015), coeval with the emplacement of the White Anorthosites. Fine-grained, weakly-banded quartzo-feldspathic gneisses (peak assemblage: Kfs-Pl-Qz±Bt±Hbl) interlayered with fine-grained amphibolites (peak assemblage: Hbl-Pl±Qz±Cpx) constitute the metavolcanic sequence (fig. 2B). Based on chemical data the sequence was interpreted to result from bimodal volcanism (Brandt, ms, 2003). Biotite-bearing migmatites of metagraywacke composition dominate the strongly deformed metasedimentary sequence of the Eyao Unit. Lenses and layers of calc-silicate rocks and quartzites are intercalated and former basaltic dikes were transformed to garnet-free amphibolites (peak assemblage: Hbl–Pl±Qz), forming boudinaged lenses in the Bt migmatites (fig. 2C). Rare migmatitic cordierite-bearing metapelites constitute dark layers in the light-gray Bt-migmatites (fig. 2D). The rocks of the volcano-sedimentary sequence show prominent, steeply inclined NW- and SE-dipping foliation planes. Leucosomes of the migmatites are mainly concordant to the foliation but discordant leucosomes also occur (fig. 2E). Garnet is very rare in both the metagraywacke-type Bt migmatites and the metapelitic Crd migmatites, and may also form cm-sized grains in the leucosomes (fig. 2F). Coarse-grained weakly-deformed orthopyroxene-cordierite rocks are exposed in isolated outcrops south of the gabbro complex in the westernmost part of the Eyao Unit.

The studied western part of the Orue Unit is mainly composed of migmatitic orthogneisses of granodioritic composition (fig. 2G). Several gabbro complexes intruded the orthogneisses and form bodies that are elongated parallel to the regional E-W-trending foliation trend (fig. 1A). Migmatitic metasediments are restricted to an area south of Okangwati (fig. 1A). Direct contacts between the surrounding orthogneiss and the paragneisses are not exposed. Grt-Bt-bearing migmatites of graywacke composition dominate the metasedimentary sequence. Rare metapelitic migmatites comprise large garnet porphyroblasts in the biotite-rich paleosomes and the quartzo-feldspathic leucosomes (fig. 2H). Garnet is rimmed by a greenish corona of cordierite. Cm-sized sillimanite grains mimic the outline of former kyanite (fig. 2H). Slightly higher *P-T* conditions of 750 °C and 7.5 kbar as for the eastern part of the Orue Unit were estimated for a Grt-Bt-Sil migmatite from this western part of the Orue Unit area (Brandt and Klemd, 2008). The sample is exceptional as it preserves *ca.* 1.75 Ga and 1.34 Ga concordant zircon (Seth and others, 2005), which may indicate a poly-metamorphic evolution.

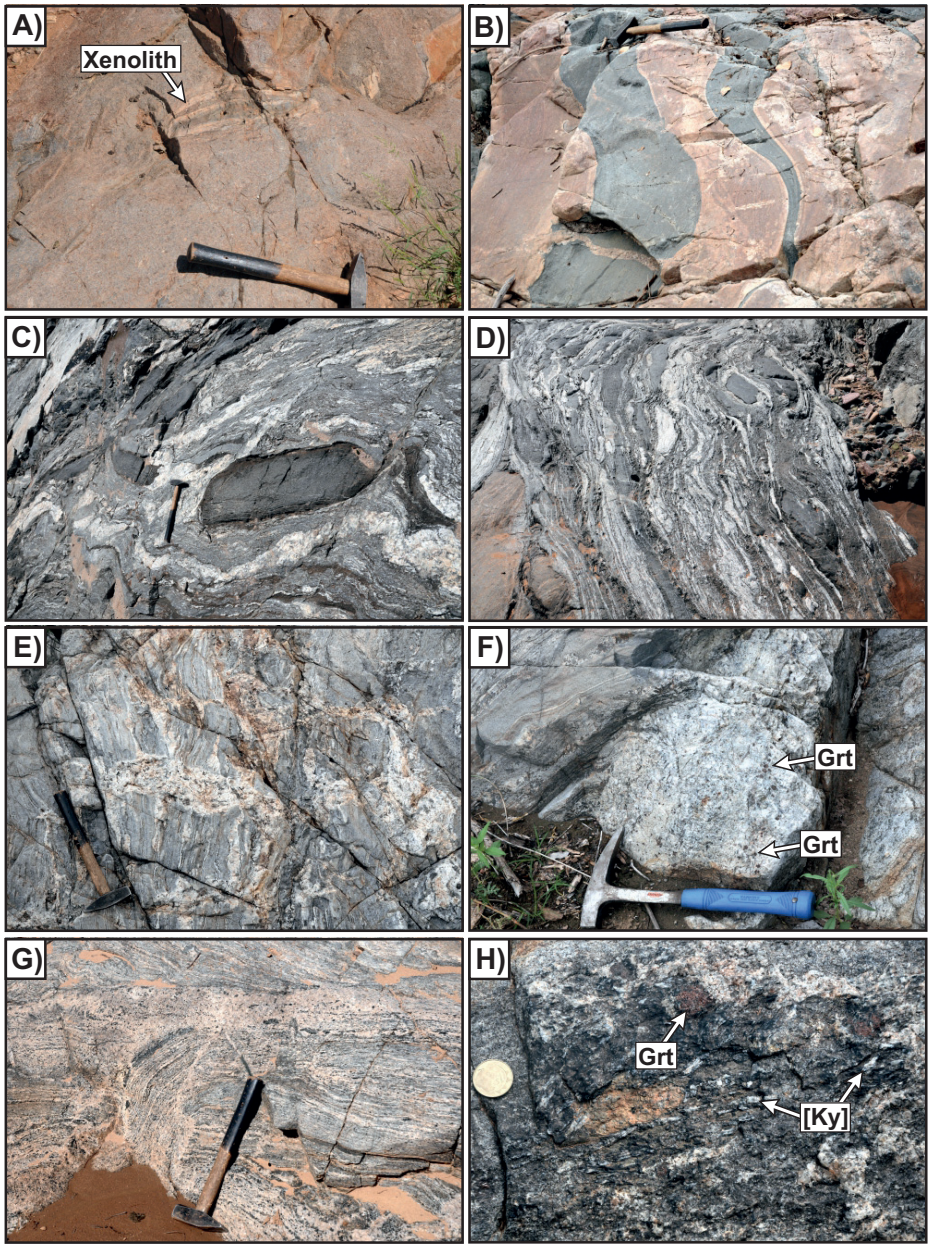

Fig. 2. Photographs illustrating field relationships in the Epupa Complex. (A) Paragneiss xenolith in undeformed Mesoproterozoic granite of the Eyao Unit (Loc: EC-716). (B) Interlayered felsic gneisses and amphibolites of the Eyao Unit. Their protoliths are interpreted to originate from bimodal volcanism. (Loc: EC-711). (C) Strongly deformed sequence of migmatitic paragneisses of the Eyao Unit with boudinaged amphibolite layer (Loc: EC-713). (D) Sequence of migmatitic paragneisses of the Eyao Unit with intercalated dark layers of metapelitic garnet-cordierite migmatites (Loc: EC-713). (E) Broad discordant leucosomes in pelitic migmatite of the Eyao Unit (Loc: EC-742). (F) Garnet-bearing leucosome in pelitic migmatite of the Eyao Unit (Loc: EC-740). (G) Migmatitic orthogneiss with concordant and discordant hornblende-bearing leucosomes (Loc. EC-752). (H) Garnet-bearing pelitic migmatite of the Orue Unit. Garnet porphyroblasts are rimmed by a greenish cordierite coronas and large sillimanite pseudomorphs outline the shape of former kyanite (Loc: EC-747).

PETROGRAPHY

The observed reaction textures and mineral assemblages in the Eyao and Orue Unit aluminous metasediments are related to three stages of the metamorphic evolution (table 1). The prograde evolution is recorded by mineral inclusions in coarse-grained peak-metamorphic minerals while, the retrograde evolution is deduced from rare corona textures.

Eyao Unit

(Grt)-Crd migmatites.—Metapelites of the Eyao Unit preserve the peak-assemblage cordierite–biotite–ilmenite-K-feldspar–plagioclase–quartz with or without additional garnet and sillimanite (table 1). A migmatitic texture is defined by concordant biotite-free garnet- and/or cordierite-bearing quartzo-feldspathic leucosomes alternating with cordierite-biotite-sillimanite-rich paleosomes. Aligned biotite and sillimanite are preserved in the least altered samples and define a S_1 foliation in the paleosomes. Biotite-sillimanite-rich layers were usually largely replaced by cordierite that was later altered to pinite during late hydrothermal alteration (fig. 3A). Sillimanite is rarely preserved in the metapelites (figs. 3A and 3B). In most samples sillimanite is preserved only as inclusion trails in the cores of polycrystalline cordierite aggregates, and is thus always separated from matrix biotite by inclusion-free cordierite rims (fig. 3C). Green spinel may occur in the quartz-absent core domains of the cordierite aggregates. Subhedral cordierite also occurs in the K-feldspar–plagioclase–quartz matrix of the metapelites (fig. 3C). Biotite and sillimanite are also enclosed by K-feldspar. White mica is preserved only as very rare inclusions in quartz or K-feldspar. Ilmenite is generally restricted to cordierite-bearing domains. Skeletal biotite-quartz intergrowths at leucosome–paleosome contacts suggest leucosome-formation through dehydration melting of biotite. The textures and inclusions suggest the formation of the cordierite–K-feldspar–ilmenite peak-assemblage through partial replacement of early sillimanite–white mica-biotite–quartz assemblages during melt-producing reactions. Garnet is a minor phase (up to 6 vol%) and forms either strongly resorbed poikiloblastic porphyroblasts (up to 5 mm), which are wrapped by the Bt-Sil layers (figs. 3A and 3B) or, more often, small euhedral to subhedral grains (<2 mm) that often occur along the margins of the Bt-Sil-Crd domains (fig. 3D) and also as inclusions in cordierite. Rare corroded biotite, white mica and quartz, enclosed by garnet, indicate partial to complete consumption of the inclusion phases during the growth of garnet, leading to the observed melt-present, peak-assemblage garnet-cordierite-biotite-ilmenite-K-feldspar-plagioclase with or without relic sillimanite and quartz.

Retrograde reaction textures are rare. Garnet may be surrounded by coronas of biotite (fig. 3D) or biotite-white mica intergrowths. In addition, white mica porphyroblasts overgrow the S_1 foliation. Strong sericitization of the feldspars and sillimanite as well as usually complete pinitization of cordierite document very intense alteration. Alteration of biotite is evident from widespread chloritization that is accompanied by the formation of ilmenite rims around biotite and by sagenite growth.

(Grt)-Bt migmatites.—The metagraywackes show a migmatitic character defined by biotite-rich paleosomes and concordant leucosomes that may contain garnet (fig. 2F). Garnet forms porphyroblasts or, more commonly, small grains in the paleosomes and is set in a granoblastic matrix of biotite, K-feldspar, plagioclase, quartz, and ilmenite. Elongated biotite defines the S_1 foliation. Abundant inclusions of biotite, plagioclase, ilmenite, and quartz in garnet suggest an early assemblage of Bt-Pl-Ilm-Qz.

Intergrowths of biotite, white mica, chlorite, and quartz form coronas around garnet or, in the case of complete garnet consumption, Bt-WM-Pl-Qz pseudomorphs after garnet. Biotite is surrounded by a corona of white mica and ilmenite.

TABLE 1

Mineral assemblages in aluminous metasediments of the Epupa Complex

	inclusions (prograde)									***matrix (peak-metamorphic)***												***coronas (retrograde)***					
Eyao Unit																											
Metapelites	*No. of samples*	Bt	WM	Sil	Ky	Pl	Qz	Ilm	Rt	Grt	Opx	Crd	Bt	Spl	Ky	Sil	Kfs	Pl	Qz	Ilm	Bt	Crd	Qz	Pl	WM	Chl
Grt-Crd-Bt-Sil migmatite	16	1,2,3,4,6	1,6	2,3,4,6	-	1,6	1,2,3,4	2	-	x	-	x	x	x	-	x	x	x	x	x	x	-	x	-	x	x
Grt-Crd-Bt migmatite	15	2,3,4,6	1,6	2,3,6	-	1,6	1,2,3,4	-	-	x	-	x	x	x	-	-	x	x	x	x	x	-	x	-	x	x
Crd-Bt migmatite			3,6	2,3,6	-	3,6	2,3,4	2	-	-	-	x	x	x	-	-	x	x	x	x	x	-	x	-	x	x
Metagreywackes																											
Bt migmatite	7	1,3,4,6	-	-	-	1,6	1,3,4	1	-	-	-	-	x	-	-	-	x	x	x	x	x	-	x	-	x	x
Grt-Bt migmatite	5	1,3,4,6	-	-	-	1,6	1,3,4	1	-	x	-	-	x	-	-	-	x	x	x	x	x	-	x	-	x	x
Opx-Crd rocks																											
Opx-Crd-Pl	3	2,4,5	-	-	-	-	2,4,5	x	x	-	x	x	-	-	-	-	-	x	x	x	x	-	-	-	-	-
Opx-Crd	1	2,5	-	-	-	-	2,5	2,5	-	-	x	x	-	-	-	-	-	-	x	x	x	-	-	-	-	-
Orue Unit																											
Metapelites																											
Grt-Bt-Sil migmatite	10	1,3,4,6	6	3,4,6	4	1,6	1	1	1	x	-	-	x	x	(x)	x	x	x	x	x	x	x	x	x	x	x	x

Inclusions in (1) Grt, (2) Crd, (3) Kfs, (4) Pl, (5) Opx, (6) Qz, (x) Sil pseudomoph after Ky.

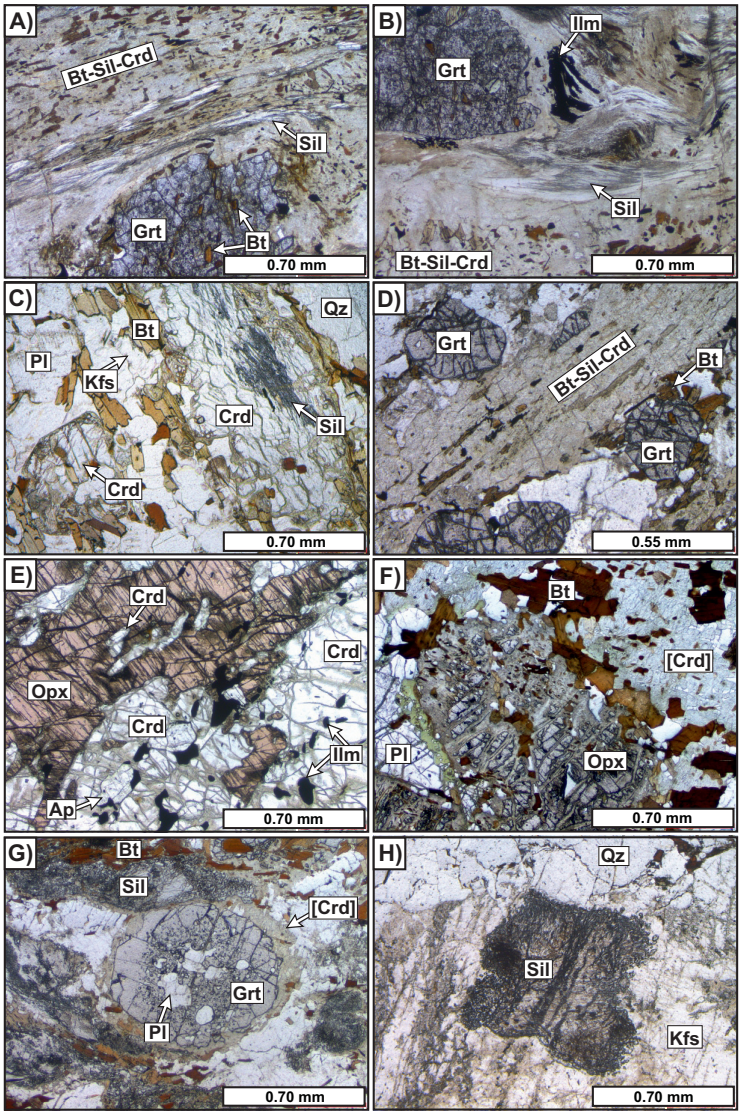

Fig. 3. Photomicrographs illustrating the evolution of the Grt-Crd migmatites and Opx-Crd rocks of the Eyao Unit and the Grt-Bt-Sil migmatites of the Orue Unit (plane polarized light). (A) Garnet porphyroblast with inclusions of biotite is surrounded by a biotite-sillimanite foliation that is largely replaced by cordierite (EC-739-A-18). (B) Sillimanite-rich layer with minor ilmenite around porphyroblastic garnet (EC-739-A-18). (C) Polycrystalline cordierite separates fibrolitic sillimanite inclusion trails from matrix biotite. Subhedral cordierite also occurs in the matrix together with abundant K-feldspar, biotite and plagioclase (B-148-A-2). (D) Largely altered cordierite-rich domain that formed at the expense of an early biotite-sillimanite layer. Euhedral to subhedral garnet occurs along the margins of the cordierite–rich domain. Garnet is partially replaced by biotite (EC-739-B-18). (E) Coexisting orthopyroxene and cordierite with partly preserved straight grain boundaries. Cordierite encloses ilmenite and apatite whereas orthopyroxene encloses cordierite and ilmenite (EC-722-18). (F) Largely altered orthopyroxene with corona of biotite. Cordierite with inclusions of biotite is completely altered to pinite (B-284-C-98). (G) Poikiloblastic garnet porphyroblast with numerous inclusions of plagioclase, quartz and biotite. Garnet is resorbed and rimmed by a greenish corona of pinitized cordierite and surrounded by a biotite-sillimanite foliation (EC-752-F-18). (H) Sillimanite resembling the outline of former kyanite (EC-752-F-18).

Opx-Crd rocks.—The Opx-Crd rocks are characterized by cm-sized anhedral orthopyroxene, coexisting with coarse-grained, anhedral cordierite (fig. 3E). Textural equilibrium between cordierite and orthopyroxene is evident from preserved sharp grain boundaries. Cordierite and orthopyroxene are situated in a matrix of minor quartz, abundant ilmenite, and, in some samples, apatite or rare plagioclase. A weak straight foliation is developed in some samples through elongated orthopyroxene and cordierite grains (fig. 3E). Ilmenite shows exsolution of magnetite. Rare inclusions in orthopyroxene are cordierite, biotite, ilmenite, and quartz whereas cordierite encloses orthopyroxene, biotite, ilmenite, and quartz, (fig. 3E). The lack of matrix biotite suggests its replacement during the formation of the Opx-Crd-Ilm peak-assemblage through partial melting reactions. The quartz-poor and K-feldspar-free mineralogy is consistent with the Si-poor residual composition and suggests that the Opx-Crd rocks represent restites of uncommon Mg-rich metasediments, which had formed through removal of the anatectic melt. Retrograde biotite may form coronas around orthopyroxene (fig. 3F). Most samples are affected by strong alteration that caused the usually complete pinitization of the cordierite and the widespread replacement of orthopyroxene (fig. 3F). Zircon appears as an abundant accessory phase, whereas monazite is very rare.

Orue Unit

Grt-Bt-Sil migmatites.—Metapelites of the western part of the Orue Unit are characterized by the peak-assemblage Grt-Bt-Sil-Kfs-Pl-Ilm-Qz coexisting with anatectic melt. The migmatitic texture of the rocks is defined by concordant garnet-bearing quartzofeldspathic leucosomes alternating with biotite-sillimanite-rich paleosomes. Aligned biotite and sillimanite of the paleosomes define a straight foliation and are hosted by a quartzo-feldspathic matrix of flame-perthitic K-feldspar, plagioclase, quartz, and rare ilmenite. Sub- to anhedral porphyroblastic garnet of the paleosomes is wrapped by the biotite-sillimanite foliation (fig. 3G). Garnet shows inclusion-rich cores that are surrounded by inclusion-poor rims (fig. 3G). Prograde mineral inclusions in the garnet cores are abundant quartz and plagioclase, and rare biotite, ilmenite and rutile; the latter of which is not preserved in the matrix. Biotite and sillimanite occur as inclusions in plagioclase, quartz, and K-feldspar. In a few samples small white mica is preserved as inclusions in quartz and in one sample euhedral kyanite occurs in plagioclase. Kyanite of the matrix is completely transformed to sillimanite, pseudomorphing the former outline of kyanite (fig. 3H). The inclusions and pseudomorphs record a prograde assemblage of garnet-biotite-white mica-kyanite/sillimanite-rutile-K-feldspar-plagioclase-quartz. Accessory minerals are apatite, zircon, and monazite.

Coronas of pinitized cordierite around garnet in the presence of sillimanite record the retrograde metamorphic evolution (fig. 3G). In addition, thin plagioclase coronas occur around garnet in the presence of sillimanite and quartz. Biotite-white mica intergrowths replace garnet along fissures. Sericitization of the feldspars and pinitization of cordierite document intense late alteration that also caused widespread chloritization of biotite in several samples.

MINERAL CHEMISTRY

Eight samples (six of the Eyao Unit and two of the Orue Unit) were investigated by electron probe micro-analysis (EMPA). The samples of the Eyao Unit include three Grt-Crd migmatites (EC-731-18, EC-739-A-18, EC-743-18), two Opx-Crd rocks (EC-722-18, B-284-C-98) and one Grt-Bt migmatite (EC-744-D-18). In addition, two Grt-Bt-Sil migmatites of the Orue Unit (EC-747-A-18, EC-752-F-18) were selected for EPMA.

Garnet.—Garnet of the aluminous metasediments is almandine-rich, with moderate pyrope and spessartine, and usually low grossular components (fig. 4, table 2).

Most garnets of the Eyao Unit Grt-Crd migmatites are unzoned with uniform compositions ($Alm_{75-79}Prp_{7-11}Grs_{2-3}Sps_{9-13}$) and low to moderate X_{Mg} values of 0.08–0.12 (fig. 4). Rare porphyroblastic garnet displays zoning with Ca and Mn continuously decreasing and almandine, pyrope and X_{Mg} increasing from the core ($Alm_{61}Prp_{6}Grs_{12}Sps_{20}$; X_{Mg}: 0.08) towards the rims ($Alm_{78}Prp_{10}Grs_{3}Sps_{9}$; X_{Mg}: 0.12), which show the highest X_{Mg}. The composition of the rims resembles the composition of the unzoned grains. In contrast, garnet of metapelite sample EC-743-18 is more magnesian and zoned with the X_{Mg} decreasing from the core ($Alm_{72}Prp_{15}Grs_{3}Sps_{10}$; X_{Mg}: 0.17) to the rims ($Alm_{74-75}Prp_{12-10}Grs_{2-3}Sps_{10-12}$; X_{Mg}: 0.14–0.12). Garnet of the Eyao Unit Grt-Bt migmatite is slightly more magnesian and shows zoning with Mg-rich cores and domains ($Alm_{70-74}Prp_{12-17}Grs_{2-3}Sps_{10-12}$; X_{Mg}: 0.14–0.19), and increasing Mn content to the rims and in altered domains ($Alm_{74-76}Prp_{8-9}Grs_{2-3}Sps_{13-17}$; X_{Mg}: 0.08–0.12).

Garnet of the Orue Unit Grt-Bt-Sil migmatites is more magnesian (fig. 4). Grains of sample EC-747-A-18 are usually unzoned $Alm_{69-72}Prp_{23-25}Grs_{1-2}Sps_{3-4}$; X_{Mg}: 0.24–0.26. Only the outmost rims show an abrupt increase of the Mn and Fe content and decrease of the Mg content ($Alm_{77-80}Prp_{11-15}Grs_{1-2}Sps_{7}$; X_{Mg}: 0.12–0.16), indicating resorption by coronitic cordierite. Garnet of sample EC-752-F-18 preserves zoning with the grossular content continuously decreasing from the core ($Alm_{67-70}Prp_{21-23}Grs_{4-8}Sps_{2-3}$; X_{Mg}: 0.24–0.25) towards the rims ($Alm_{74-75}Prp_{19-20}Grs_{3-4}Sps_{3}$; X_{Mg}: 0.20–0.25).

Biotite.—Biotite of the studied samples shows a large compositional variation (fig. 5; table 3). The large spread in Ti results from variable, but generally intense, chloritization during alteration, which is also evident from low K contents.

Regarding their peak-assemblage, matrix biotite of the Eyao Unit Grt-Crd migmatites should plot in the Grt-Crd-Sil-Kfs field in the X_{Mg} v. Ti diagram of Robinson and others (1982). However, probably due to strong alteration and the uncommon Fe-rich bulk rock composition most biotites of the Grt-Crd migmatites plot outside any fields in the diagram. Matrix biotite (X_{Mg}: 0.27–0.41, Ti p.f.u.: 0.22–0.46), biotite inclusions in garnet (X_{Mg}: 0.29–0.40, Ti p.f.u. 0.21–0.44), and biotite in contact with garnet (X_{Mg}: 0.40; Ti p.f.u. 0.40–0.41) display similar Fe-rich compositions with moderate (EC-731-18, EC-739-A-18) to high Ti content (EC-743-18).

Matrix biotite of the Eyao Unit Grt-Bt migmatite is slightly more magnesian (fig. 5). Matrix biotite (X_{Mg}: 0.40–0.48; Ti p.f.u. 0.26–0.30) has higher Ti contents than coronitic biotite resorbing garnet (X_{Mg}: 0.43–0.47; Ti p.f.u. 0.15–0.19).

Biotite inclusions in cordierite of the Eyao Unit Opx-Crd rocks displays the highest X_{Mg} values of the studied samples (EC-722-18: X_{Mg}: 0.76–0.78; B-284-C-98: X_{Mg}: 0.56–0.59) and have moderate Ti contents (Ti p.f.u. 0.25–0.31), and plot in the Grt-Crd-Sil-Kfs field (fig. 5). Coronitic biotite around orthopyroxene and cordierite is slightly more magnesian and more titaniferous (B-284-C-98: X_{Mg}: 0.61–0.72, 0.30–0.44 Ti p.f.u.) than the biotite inclusions of the samples.

Matrix biotite (X_{Mg}: 0.43–0.49, Ti: 0.38–0.51) of the Orue Unit Grt-Bt-Sil migmatites are more magnesian than biotite of the Eyao Unit Grt-Crd-Bt-Sil migmatites and show variable Ti contents. Consistent with the muscovite-free peak assemblage, part of the matrix biotite of sample EC-752-F-18 plots in the Sil-Kfs field (fig. 5). Strong alteration caused resetting of the Ti content of matrix biotite of sample EC-747-A-18 (X_{Mg}: 0.39–0.43; Ti p.f.u. 0.16–0.29). The Ti-content is similar to that of more magnesian coronitic biotite (X_{Mg}: 0.49–0.51; Ti p.f.u. 0.25–0.27) formed at the expense of garnet during retrogression.

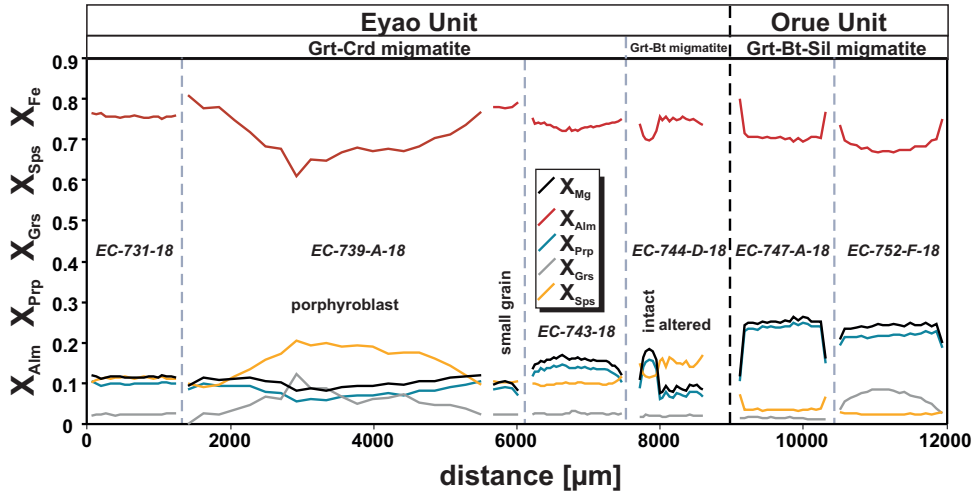

Fig. 4. Zoning profiles of garnet in the migmatitic metasediments of the Epupa Complex. Each profile extends from rim to rim through the core of garnet grains. Garnet of the Orue Unit metapelites is more magnesian and has less manganese than garnet of the Eyao Unit metapelites.

Orthopyroxene.—Orthopyroxene of the Opx-Crd rocks is unzoned, Ca-free, and Mg-rich (X_{Mg}: B-284-C-98: 0.64–0.68, EC-722-18: 0.74–0.78; table 4). The Al_2O_3 contents are low (B-284-C-98: up to 2.35 wt.%, EC-722-18: up to 2.55 wt.%).

Cordierite.—Fresh matrix cordierite is preserved only in the Eyao Unit Opx–Crd sample EC-722-18 and is highly magnesian and unzoned (X_{Mg}: 0.86–0.88; table 4). The Na_2O contents range between 0.27 and 0.73 weight percent and high totals of 99 to 100 weight percent suggest the lack of water in the structural channels. Cordierite of the Opx-Crd rock B-284-C-98 and the Eyao Unit Grt-Crd migmatites is completely altered to pinite as evidenced by high K contents, and low Si and Al contents (table 4). Assuming that the X_{Mg} was not significantly modified by alteration, the matrix cordierite of the Eyao Unit Grt-Crd migmatites is less magnesian (X_{Mg}: 0.39–0.53) than the cordierite of the Opx-Crd rock.

Completely pinitized coronitic cordierite around garnet of the Orue Unit Grt-Bt-Sil migmatite is more magnesian (X_{Mg}: 0.57–0.59) than cordierite of the Eyao Unit Grt-Crd-Bt-Sil migmatite.

Ilmenite and magnetite.—Matrix ilmenite of the Opx-Crd rocks has moderate MnO (1.6–3.4 wt.%) and variable Fe_2O_3 (EC-722-18: 5–9 wt.%, B-284-C-98: 0–3.1 wt.%) contents, as calculated from ideal stoichiometry (table 4). Ilmenite of the Grt-Crd migmatites has high MnO contents (6.0–7.7 wt.%) but no Fe_2O_3.

Magnetite exsolution lamellae from the ilmenite of the Opx-Crd rocks contain high proportions of TiO_2 (10.7–19.5 wt.%) as well as traces of Cr_2O_3 (0.15–0.28 wt.%) and MnO (0.18–0.25 wt.%).

Feldspar.—Matrix plagioclase of the Grt-Crd migmatites, the Opx-Crd rocks, and the Grt-Bt-migmatites of the Eyao Unit is unzoned oligoclase (An_{12-31}, table 5). Alkali feldspar of the Grt-Bt-migmatites and Grt-Crd migmatites is usually nearly pure orthoclase ($Or_{89-96}Ab_{11-4}An_{0-1}$).

Matrix plagioclase of Grt-Bt-Sil migmatite EC-752-F-18 is unzoned oligoclase (An_{25-30}) whereas plagioclase enclosed by garnet is unzoned andesine (An_{35-37}). Matrix feldspar of Grt-Bt-Sil migmatite EC-747-A-18 is unzoned albite (An_{10-09}).

TABLE 2

Representative microprobe analyses of garnet

Rock unit	**Eyao Unit**								**Orue Unit**			
Rock type	*Grt-Crd migmatite*						*Grt-Bt migmatite*		*Grt-Bt-Sil migmatite*			
Sample	EC-731-18	EC-739-A-18			EC-743-18		EC-744-D-18		EC-747-A-18		EC-752-F-18	
Analysis	grt1-15	grt1-8	grt1-2	grt2-4	grt1-11	grt1-3	grt4-4	grt4-12	grt1-13	grt1-1	grt1-1	grt1-18
Texture	blast	porphyroblast		small	blast		blast		blast		blast	
Position	core	core	rim	core	core	rim	intact domain	altered	core	rim	core	rim
wt.%												
SiO_2	37.53	37.29	37.61	37.72	37.23	37.21	37.90	37.38	38.58	37.48	38.58	38.47
TiO_2	0.07	0.03	0.06	0.07	0.00	0.00	0.00	0.00	0.02	0.00	0.03	0.03
Al_2O_3	21.13	21.43	21.43	21.40	21.21	21.18	21.77	21.15	21.68	21.13	22.08	22.17
Cr_2O_3	0.03	0.01	0.01	0.01	0.00	0.01	0.01	0.00	0.00	0.00	0.02	0.02
MgO	2.67	1.42	2.53	2.24	3.71	2.61	4.09	1.95	6.47	2.68	5.64	5.82
CaO	0.75	4.41	0.96	0.88	0.93	0.94	0.79	0.79	0.59	0.59	3.09	1.45
MnO	4.88	9.09	4.12	4.58	4.46	5.17	5.19	6.63	1.70	3.26	1.12	1.18
FeO	33.99	27.79	34.55	35.06	32.10	33.71	31.97	33.76	32.67	35.62	31.37	32.06
total	101.06	101.47	101.26	101.96	100.89	100.87	101.75	101.70	101.79	100.77	101.91	101.20
normalized to 12 oxygens												
Si	3.00	2.98	3.01	3.00	3.00	2.99	2.99	3.00	3.00	3.01	2.98	2.99
Ti	0.00	0.00	0.00	0.00	0.00	0.00	0.00	0.00	0.00	0.00	0.00	0.00
Al	1.99	2.02	2.02	2.01	2.01	2.01	2.02	2.00	1.98	2.00	2.01	2.02
Cr	0.00	0.00	0.00	0.00	0.00	0.00	0.00	0.00	0.00	0.00	0.00	0.00
Mg	0.32	0.17	0.30	0.27	0.44	0.31	0.48	0.23	0.75	0.32	0.65	0.68
Ca	0.06	0.38	0.08	0.08	0.08	0.08	0.07	0.07	0.05	0.05	0.26	0.12
Mn	0.33	0.61	0.28	0.31	0.30	0.35	0.35	0.45	0.11	0.22	0.07	0.08
Fe	2.28	1.86	2.31	2.33	2.16	2.27	2.11	2.26	2.12	2.39	2.03	2.09
total	7.99	8.01	8.00	7.99	8.00	8.01	8.00	8.01	8.01	7.99	8.01	7.99
X_{Mg}	0.12	0.08	0.12	0.10	0.17	0.12	0.19	0.09	0.26	0.12	0.24	0.25
Prp	10.6	5.6	10.1	8.9	14.9	10.4	16.0	7.7	24.7	10.7	21.6	23.0
Grs	2.1	12.5	2.8	2.5	2.7	2.7	2.2	2.2	1.6	1.7	8.5	4.1
Sps	11.1	20.4	9.4	10.3	10.2	11.7	11.5	14.9	3.7	7.4	2.5	2.7
Alm	76.1	61.5	77.7	78.2	72.3	75.3	70.2	75.1	70.0	80.1	67.5	70.2

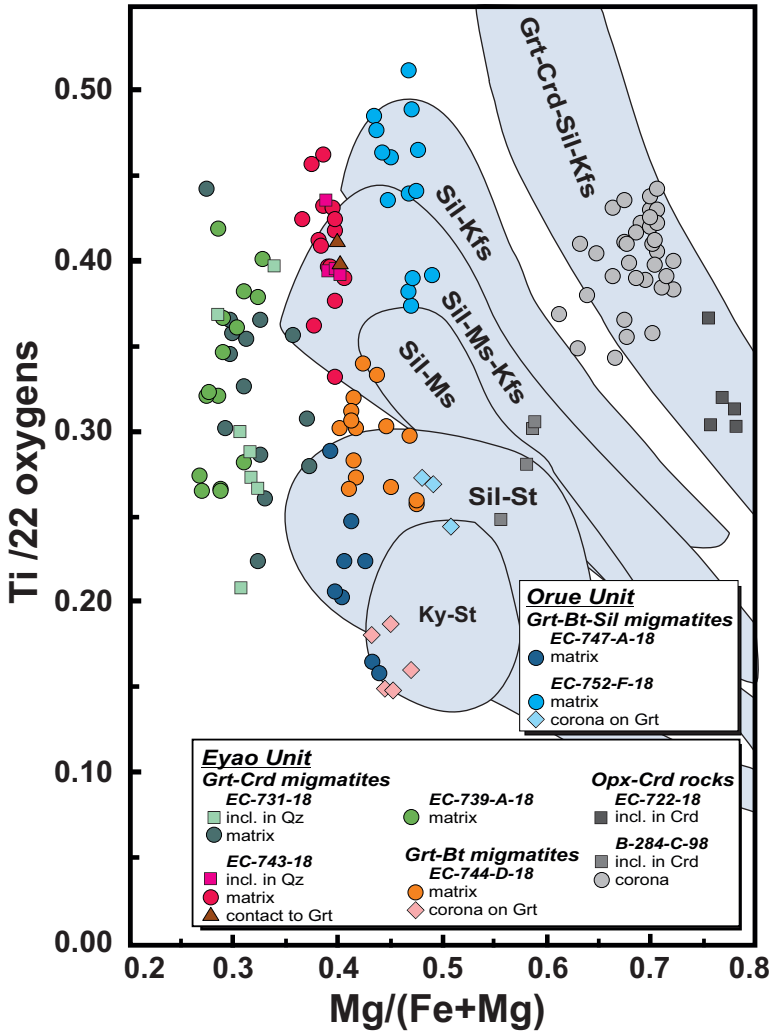

Fig. 5. Composition of biotite in the migmatitic metasediments and the Opx-Crd rocks of the Epupa Complex illustrated for Mg/(Fe+Mg) vs. Ti a.p.f.u. (22 oxygens). The shaded fields indicate the compositional range of biotite from metamorphic zones in New England (Robinson and others, 1982).

METAMORPHIC EVOLUTION OF THE EYAO AND ORUE UNIT

Results from conventional geothermobarometry are combined with constraints from pseudosection modeling in the MnNCKFMASHTO system to characterize the geodynamic evolution of the Eyao and Orue Units.

Geothermobarometry

The thermobarometric calculations were performed with mineral chemical data given in tables 2–5. The results and applied thermobarometers are summarized in table 6. Peak-metamorphic *P-T* conditions were calculated by combining the compositions of the flat core plateaus of the garnet that were homogenized during peak metamorphism (EC-731-18, EC-747-A-18), the unzoned matrix plagioclase, and the matrix

TABLE 3

Representative microprobe analyses of biotite

Rock unit	Eyao Unit											Orue Unit		
Rock type	*Opx-Crd rocks*			*Grt-Crd migmatites*								*Grt-Bt migmatites*	*Grt-Bt-Sil migmatites*	
Sample	EC-722-18	B-284-C-98		EC-731-18		EC-739-A-18	EC-743-18			EC-744-D-18		EC-747-A-18	EC-752-F-18	
Analysis	bt1-1	bt8-7	bt7-3	bt2-1	bt6-2	bt1-5	bt5-1	bt4-2	bt3-1	bt3-3	bt2-5	bt1-2	bt5-2	bt3-2
Texture	incl. in Crd	incl. in Crd	corona on Crd	incl. in Qz	matrix	matrix	incl. in Qz	matrix	contact Grt	matrix	corona on Grt	matrix	matrix	corona on Grt
wt.%														
SiO_2	40.03	34.73	37.39	32.80	35.19	34.39	35.10	34.54	35.41	35.25	33.88	36.72	36.80	36.72
TiO_2	2.82	2.40	3.48	3.10	3.84	3.61	3.42	3.67	3.50	2.63	1.23	1.96	4.16	2.21
Al_2O_3	15.03	14.41	15.13	18.65	18.28	18.91	18.58	18.26	18.93	18.91	18.46	18.30	18.29	20.41
Cr_2O_3	0.00	0.12	0.12	0.00	0.00	0.03	0.00	0.04	0.00	0.00	0.01	0.00	0.01	0.03
FeO	10.62	19.16	13.64	26.80	25.34	24.25	21.27	22.64	21.37	21.07	18.57	20.34	19.66	17.20
MnO	0.02	0.17	0.16	0.35	0.33	0.37	0.16	0.23	0.18	0.21	0.13	0.21	0.13	0.10
MgO	18.54	14.84	15.07	6.11	5.38	5.46	8.03	7.33	7.95	7.97	8.42	8.46	8.77	9.93
CaO	0.00	0.04	0.06	0.09	0.02	0.00	0.06	0.02	0.01	0.01	0.01	0.03	0.05	0.04
Na_2O	0.30	0.20	0.17	0.02	0.07	0.21	0.12	0.05	0.05	0.07	0.07	0.10	0.10	0.16
K_2O	8.35	6.85	9.45	6.66	9.00	9.21	9.56	9.35	10.03	10.12	9.00	9.92	9.59	9.90
total	95.70	92.91	94.66	94.60	97.45	96.44	96.29	96.11	97.42	96.23	89.79	96.03	97.55	96.71
normalized to 22 O														
Si	5.76	5.40	5.59	5.18	5.38	5.31	5.35	5.31	5.34	5.38	5.47	5.57	5.47	5.43
Al^{IV}	2.24	2.60	2.41	2.82	2.62	2.69	2.65	2.69	2.66	2.62	2.53	2.43	2.53	2.57
Al^{VI}	0.30	0.04	0.26	0.64	0.68	0.75	0.68	0.62	0.70	0.78	0.98	0.84	0.67	0.99
Ti	0.30	0.28	0.39	0.37	0.44	0.42	0.39	0.42	0.40	0.30	0.15	0.22	0.46	0.25
Cr	0.00	0.01	0.01	0.00	0.00	0.00	0.00	0.00	0.00	0.00	0.00	0.00	0.00	0.01
Fe	1.28	2.49	1.70	3.54	3.24	3.13	2.71	2.91	2.69	2.69	2.51	2.58	2.44	2.13
Mn	0.00	0.02	0.02	0.05	0.04	0.05	0.02	0.03	0.02	0.03	0.02	0.03	0.02	0.01
Mg	3.97	3.44	3.36	1.44	1.23	1.26	1.82	1.68	1.79	1.81	2.03	1.91	1.94	2.19
Ca	0.00	0.01	0.01	0.02	0.00	0.00	0.01	0.00	0.00	0.00	0.00	0.00	0.01	0.01
Na	0.08	0.06	0.05	0.01	0.02	0.06	0.04	0.01	0.01	0.02	0.02	0.03	0.03	0.05
K	1.53	1.36	1.80	1.34	1.76	1.81	1.86	1.83	1.93	1.97	1.85	1.92	1.82	1.87
total	15.47	15.71	15.60	15.40	15.41	15.49	15.53	15.52	15.54	15.60	15.56	15.54	15.39	15.50
X_{Mg}	0.76	0.58	0.66	0.29	0.27	0.29	0.40	0.37	0.40	0.40	0.45	0.43	0.44	0.51

TABLE 4

Representative microprobe analyses of orthopyroxene, cordierite, ilmenite and magnetite

mineral	**Orthopyroxene**		**Cordierite**				**Illmenite**				**Magnetite**
Rock unit	**Eyao Unit**					**Orue unit**	**Eyao Unit**				
Rock type	*Opx-Crd rock*		*Opx-Crd rock*	*Grt-Crd migmatite*		*Grt-Bt-Sil migmatite*	*Grt-Crd migmatite*		*Opx-Crd rock*		*Opx-Crd rock*
Sample	EC-722-18	B-284-C-98	EC-722-18	EC-731-18	EC-743-18	EC-752-18	EC-731-18	EC-739-A-18	EC-722-18	B-284-C-98	EC-722-18
Analysis	opx1-3	opx2-5	crd4-3	crd1-4 (altered)	crd1-3 (altered)	crd1-3 (altered)	ilm1-3	ilm1-1	ilm1-17	ilm2-4	mag1-16
Texture	matrix	matrix	matrix	matrix	matrix	Corona on Grt	matrix	matrix	matrix	matrix	exsolution line
wt.%											
SiO_2	54.17	52.68	51.32	48.40	46.49	45.52	0.04	0.02	0.01	0.02	0.05
TiO_2	0.10	0.09	0.00	0.01	0.00	0.03	53.19	52.50	50.30	52.81	16.09
Al_2O_3	2.48	2.27	33.97	31.71	31.82	31.48	0.29	0.01	0.02	0.00	0.09
Cr_2O_3	0.01	0.09	0.00	0.02	0.00	0.00	0.02	0.02	0.05	0.19	0.24
Fe_2O_3	nc	nc	nc	nc	nc	nc	0.00	0.00	5.96	0.00	35.94
FeO	16.78	22.2	3.08	4.15	5.48	4.31	41.64	38.41	43.36	43.71	44.66
MnO	0.26	0.22	0.07	0.04	0.05	0.02	5.22	7.67	1.53	3.39	0.35
MgO	27.32	23.19	11.80	1.79	3.52	3.27	0.01	0.02	0.17	0.08	0.07
CaO	0.12	0.15	0.02	0.04	0.11	0.04	0.05	0.02	0.02	0.09	0.00
Na_2O	0.00	0	0.55	0.12	0.12	0.14	0.00	0.03	0.03	0.00	0.00
K_2O	0.00	0.00	0.03	10.63	9.38	9.57	0.01	0.04	0.00	0.00	0.01
total	101.23	100.89	100.85	96.89	96.97	94.37	100.46	98.73	101.43	100.29	97.50
	normalized to 6 oxygen			*normalized to 18 oxygen*				*normalized to*	*4 cations*		*norm. to 3 cations*
Si	1.94	1.94	5.03	5.25	5.06	5.07	0.00	0.00	0.00	0.00	0.00
Ti	0.00	0.00	0.00	0.00	0.00	0.00	2.00	2.01	1.89	2.00	0.47
Al	0.10	0.10	3.93	4.05	4.08	4.13	0.02	0.00	0.00	0.00	0.00
Cr	0.00	0.00	0.00	0.00	0.00	0.00	0.00	0.00	0.00	0.01	0.01
Fe^{3+}	nc	nc	nc	nc	nc	nc	0.00	0.00	0.22	0.00	1.05
Fe^{2+}	0.50	0.68	0.25	0.38	0.50	0.40	1.74	1.64	1.81	1.84	1.45
Mn	0.01	0.01	0.01	0.00	0.00	0.00	0.22	0.33	0.06	0.14	0.01
Mg	1.45	1.27	1.73	0.29	0.57	0.54	0.00	0.00	0.01	0.01	0.00
Ca	0.00	0.01	0.00	0.00	0.01	0.00	0.00	0.00	0.00	0.00	0.00
Na	0.00	0.00	0.10	0.02	0.03	0.03	0.00	0.00	0.00	0.00	0.00
K	0.00	0.00	0.00	1.47	1.30	1.36	0.00	0.00	0.00	0.00	0.00
total	4.01	4.01	11.06	11.47	11.56	11.55	3.99	3.99	4.0	4.00	3.00
X_{Mg}	0.74	0.65	0.87	0.43	0.53	0.57					

Nc: not calculated.

TABLE 5

Representative microprobe analyses of feldspar

Rock unit	Eyao Unit					Orue Unit			Eyao Unit	
Rock type	*Opx-Crd rock*	*Grt-Crd migmatite*			*Grt-Bt migmatite*	*Grt-Bt-Sil migmatite*			*Grt-Crd migmatite*	*Grt-Bt migmatite*
Sample	B-284-C-98	EC-731-18	EC-739-A-18	EC-743-18	EC-744-D-18	EC-747-A-18	EC-752-F-18		EC-739-A-18	EC-744-D-18
Analysis	pl2-3	pl2-10	pl1-4	pl2-3	pl3-6	pl1-4	pl4-5	pl5-5	kfs1-5	kfs1-2
Texture	matrix	matrix	matrix	matrix	matrix	matrix	incl. in Grt	matrix	matrix	matrix
Position	core	core	core	core	core	core	core	core	core	core
wt.%										
SiO_2	62.12	64.43	60.59	61.68	64.10	65.84	59.00	61.79	65.09	64.45
TiO_2	0.01	0.00	0.00	0.00	0.00	0.00	0.00	0.00	0.00	0.00
Al_2O_3	24.82	23.53	25.71	25.18	23.50	22.84	26.30	24.30	19.66	19.64
FeO	0.07	0.01	0.00	0.02	0.04	0.05	0.17	0.01	0.06	0.00
MnO	0.00	0.02	0.00	0.01	0.00	0.01	0.04	0.00	0.01	0.02
MgO	0.01	0.02	0.00	0.00	0.00	0.00	0.00	0.00	0.01	0.01
CaO	6.37	4.83	6.61	5.73	3.75	1.98	7.59	5.69	0.08	0.05
Na_2O	7.90	8.83	8.13	8.41	9.68	11.09	7.28	8.45	1.19	0.40
K_2O	0.29	0.16	0.21	0.36	0.21	0.12	0.08	0.38	15.21	16.13
total	101.58	101.82	101.25	101.39	101.28	101.92	100.46	100.61	101.30	100.69
normalized to 8 oxygens										
Si	2.72	2.80	2.67	2.70	2.80	2.85	2.62	2.73	2.96	2.96
Al	1.28	1.20	1.33	1.30	1.21	1.16	0.00	0.00	1.05	1.06
Ti	0.00	0.00	0.00	0.00	0.00	0.00	1.38	1.27	0.00	0.00
Fe	0.00	0.00	0.00	0.00	0.00	0.00	0.01	0.00	0.00	0.00
Mn	0.00	0.00	0.00	0.00	0.00	0.00	0.00	0.00	0.00	0.00
Mg	0.00	0.00	0.00	0.00	0.00	0.00	0.00	0.00	0.00	0.00
Ca	0.30	0.22	0.31	0.27	0.18	0.09	0.36	0.27	0.00	0.00
Na	0.67	0.74	0.69	0.72	0.82	0.93	0.63	0.72	0.10	0.04
K	0.02	0.01	0.01	0.02	0.01	0.01	0.00	0.02	0.88	0.94
total	4.99	4.97	5.02	5.01	5.01	5.04	5.00	5.01	5.01	5.00
An	30.3	23.0	30.6	26.8	17.4	8.9	36.4	26.5	0.4	0.2
Ab	68.0	76.1	68.2	71.2	81.4	90.5	63.2	71.4	10.5	3.6
Or	1.6	0.9	1.1	2.0	1.2	0.6	0.5	2.1	89.1	96.2

TABLE 6

Summary of calculated thermobarometric data for pelitic migmatites of the Epupa Complex

		Mineral composition					P (kbar)	Temperature (°C)					T (°C)	Pressure (kbar)				
		Grt		Bt		Pl		*Grt-Bt*				*Ti-in-Bt*		*GASP*			*Grt-Bt-Pl-Qz*	
sample	analyses	X_{Mg}	X_{Grs}	X_{Mg}	Ti pfu	X_{An}	(ref)	B	PL	KR	H	Hen	(ref)	NH	KN	PH	W(Mg)	W(Fe)
Eyao Unit																		
EC-731-18	grt1-2, bt6-2, pl2-10	0.12	0.021	0.27	0.44	0.23	*4.0*	707	716	712	732	698	*720*	3.9	4.6	4.1	-	-
EC-739-A-18	grt1-2, bt1-5, pl1-4	0.12	0.028	0.29	0.42	0.31	*4.0*	706	712	699	721	692	*720*	3.4	4.2	3.7	-	-
EC-743-18	grt1-11, bt4-2, pl2-3	0.17	0.027	0.37	0.42	0.27	*4.0*	734	729	728	732	699	*720*	-	-	-	3.3	3.4
EC-744-D-18	grt4-4, bt3-3, pl3-6	0.19	0.022	0.40	0.30	0.17	*4.0*	717	716	700	722	649	*720*	-	-	-	5.2	5.2
Orue Unit																		
EC-747-A-18	grt1-13, bt1-2	0.26	0.020	0.43	0.22	0.09	*8.0*	840	825	794	819	599	*780*	-	-	-	-	-
EC-752-F-18	grt1-18, bt5-3, pl2-3	0.25	0.040	0.47	0.51	0.27	*8.0*	797	787	775	786	726	*780*	7.9	8.6	8.2	-	-

Calibrations:

B, Bhattacharya and others (1992); PL, Perchuk and Lavrent'eva (1983); KR, Kleemann and Reinhardt (1994); H, Holdaway (2000); Hen, Henry and others (2005); NH, Newton and Haselton (1981); KN, Koziol and Newton (1988); PH, Powell and Holland (1988); W(Mg) and W(Fe), Wu et al. (2004).

biotite. In case of retrograde zoned garnet (EC-743-18, EC-744-D-18) the most magnesian core composition was used that is interpreted to reflect most closely the composition during peak metamorphism. For prograde zoned garnet of Grt-Crd migmatite EC-739-A-18 and Grt-Bt-Sil migmatite EC-752-F-18 the inner rim composition, which is interpreted to represent the peak metamorphic conditions, was used for the calculations, as the core formed during the prograde evolution and the outer rim was affected by post-peak Fe-Mg exchange with biotite. Due to the intense alteration the most Fe-rich matrix biotite was selected for the calculations. Nonetheless, due to the retrograde overprint of biotite, which is evident from widespread chloritization, and the concomitant Ti exsolution, and the garnets showing retrograde zoning, the calculated temperatures represent minimum values (for example, Frost and Chacko, 1989). Cordierite of the migmatites was not considered in the calculations, since it is completely altered in the Grt-Crd migmatites.

As Grt-Bt thermometry is nearly, and Ti-in-biotite thermometry is completely, independent of the applied pressure, we first calculated the peak temperatures (for reference pressures of 4 kbar (Eyao Unit) and 8 kbar (Orue Unit)). The estimated Grt-Bt temperatures were then used as reference values for the strongly temperature-dependent pressure calculations.

Eyao Unit.—The Grt-Bt temperatures mainly cluster between 700 and 730 °C (for the reference pressure of 4 kbar) that correspond to the mid-amphibolite facies, and GASP as well as Grt-Bt-Pl-Qz pressures between 3.5 to 5 kbar (for a reference temperature of 720 °C). The Ti- in biotite temperatures are slightly lower than the Grt-Bt data (table 6) and mainly cluster at *ca.* 700 °C. The lower temperatures are interpreted to result from Ti-exsolution from biotite, which is evident from the formation of sagenite or ilmenite at biotite margins.

Orue Unit.—The two metapelites of the Orue Unit yield higher, upper amphibolite facies Grt-Bt temperatures of 760 to 840 °C (for a reference pressure of 8 kbar) than the Eyao Unit migmatites. The Ti-in-biotite temperatures are slightly (sample EC-752-F-18) to much (sample EC-747-A-18) lower than the Grt-Bt data (table 6), presumably as a result of the moderate (sample EC-752-F-18) to intense (sample EC-747-A-18) alteration of the biotite. Higher GASP pressures of *ca.* 8 kbar than estimated for the Eyao Unit samples were calculated for the Grt-Bt-Sil migmatite EC-752-F-18 of the Orue Unit (for a reference temperature of 780 °C). The metapelite sample EC-747-A-18 was excluded from the calculations because of the low Ca content of albite-rich feldspar (X_{An}: 0.08–0.10). Plagioclase with low Ca ($X_{An} < 0.17$) is known to yield erroneous pressure estimates (for example, Holdaway, 2001).

Pseudosection Modeling

To constrain the *P-T* evolution in the studied parts of the Epupa Complex, phase diagrams were calculated in the system MnNCKFMASHTO for six metapelitic migmatites and one Opx-Crd rock (figs. 6A–6F) using the THERIAK-DOMINO software (version 04.02.2017, De Capitani and Brown, 1987) and the latest version of the Holland and Powell (2011) thermodynamic dataset (filename: tc-ds62.tx). Ax models used are of White and others (2014a) for garnet, biotite, cordierite, orthopyroxene, staurolite, ilmenite, chloritoid, and chlorite, White and others (2014b) for white mica and melt, Holland and Powell (2003) for feldspar, and White and others (2002) for spinel. Due to a range of sources of error, the uncertainity on the absolute position of phase boundaries is typically up to 50 °C and 1 kbar at 1 sigma (Palin and others, 2016). Since we used the same database and *a-x* relations for all calculations these absolute uncertainties are reduced to around 20 °C and 0.2 kbar (Powell and Holland, 2008.

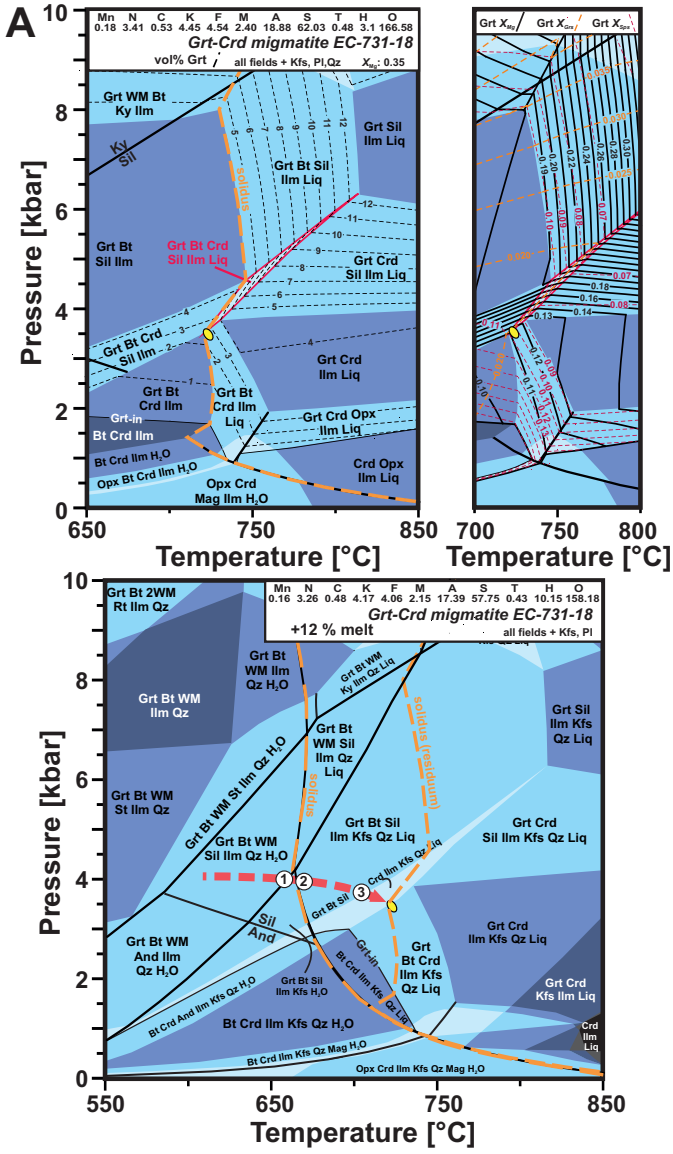

Fig. 6. *P-T* pseudosections in the system MnO-Na_2O-CaO-K_2O-FeO-MgO-Al_2O_3-SiO_2-TiO_2-H_2O-O_2 (MnNCKFMASTHO) or MnO-FeO-MgO-Al_2O_3-SiO_2-TiO_2-H_2O-O_2 (MnFMASTHO) with inferred *P-T* paths. The bulk rock composition is given as the normalized mole-proportions of the MnNCKFMASTHO or MnFMASTHO components. Pseudosections were calculated for the residual composition (upper diagram) and for the melt-reintegrated (lower diagram) composition (except for the restitic Opx-Crd rock-Fig 6E). The yellow ellipsoids mark the peak-*P-T*-conditions as constrained from the analyzed composition of garnet, cordierite or orthopyroxene. Inferred *P-T* path segments are indicated as stippled bold red lines and the solidus as stippled orange lines. In the melt-reintegrated diagram the solidus of the residuum composition is also shown for comparison. The numbers on the *P-T* paths refer to textural relationships described in the text. Mineral abbreviations are from Whitney and Evans (2010) with additional WM (white mica). (A) Grt-Crd migmatite EC-731-18 of the Eyao Unit. Field with red outline represent the inferred peak-metamorphic assemblage of the sample in the diagram for the residual composition that is contoured for the modal amount of garnet. The portion between 700–800 °C of the pseudosection is contoured in a separate diagram for the *X*Mg, *X*Grs and *X*Sps of garnet.

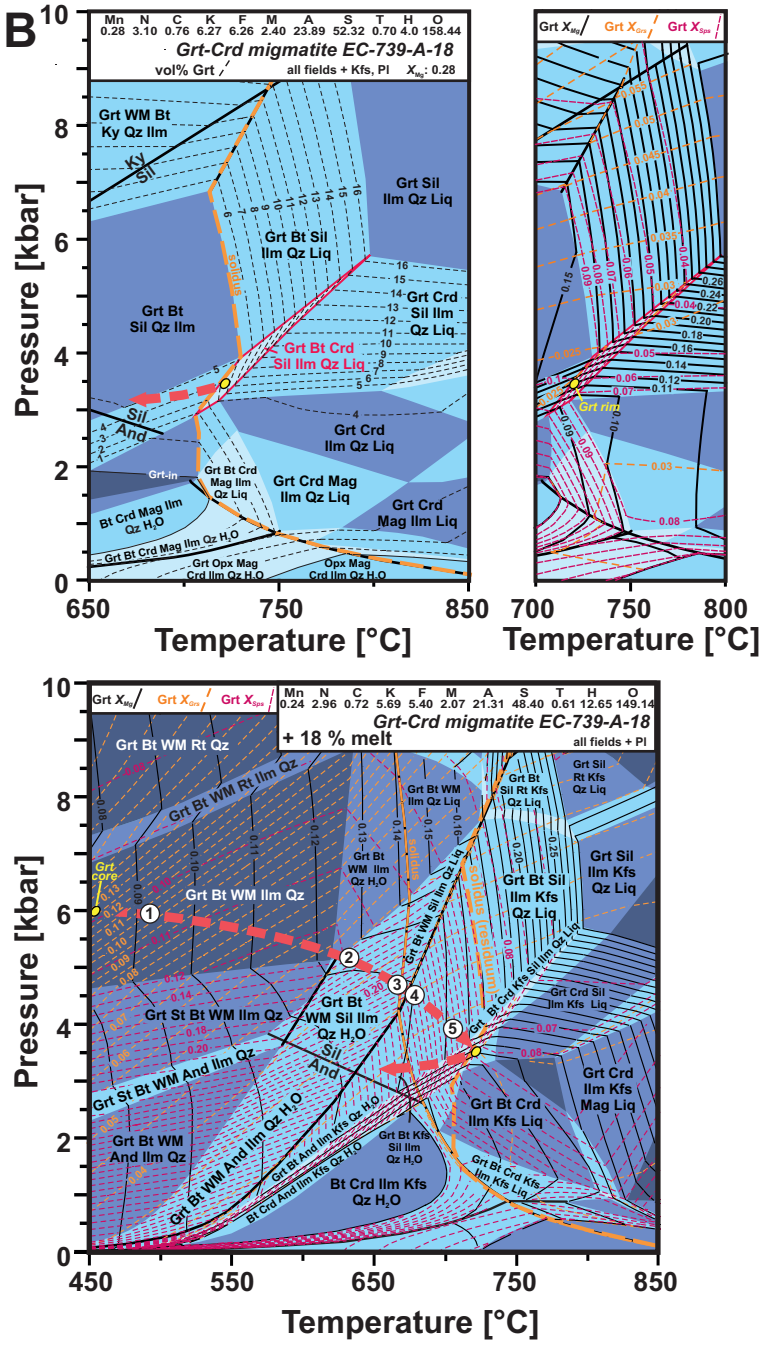

Fig. 6. Continued. (B) Grt-Crd migmatite EC-739-A-18 of the Eyao Unit. Field with red outline represent the inferred peak-metamorphic assemblage of the sample in the diagram for the residual composition that is contoured for the modal amount of garnet. The portion between 700–800 °C of the pseudosection is contoured in a separate diagram for the *X*Mg, *X*Grs and *X*Sps of garnet. The melt reintegrated pseudosection is also contoured for the composition of garnet.

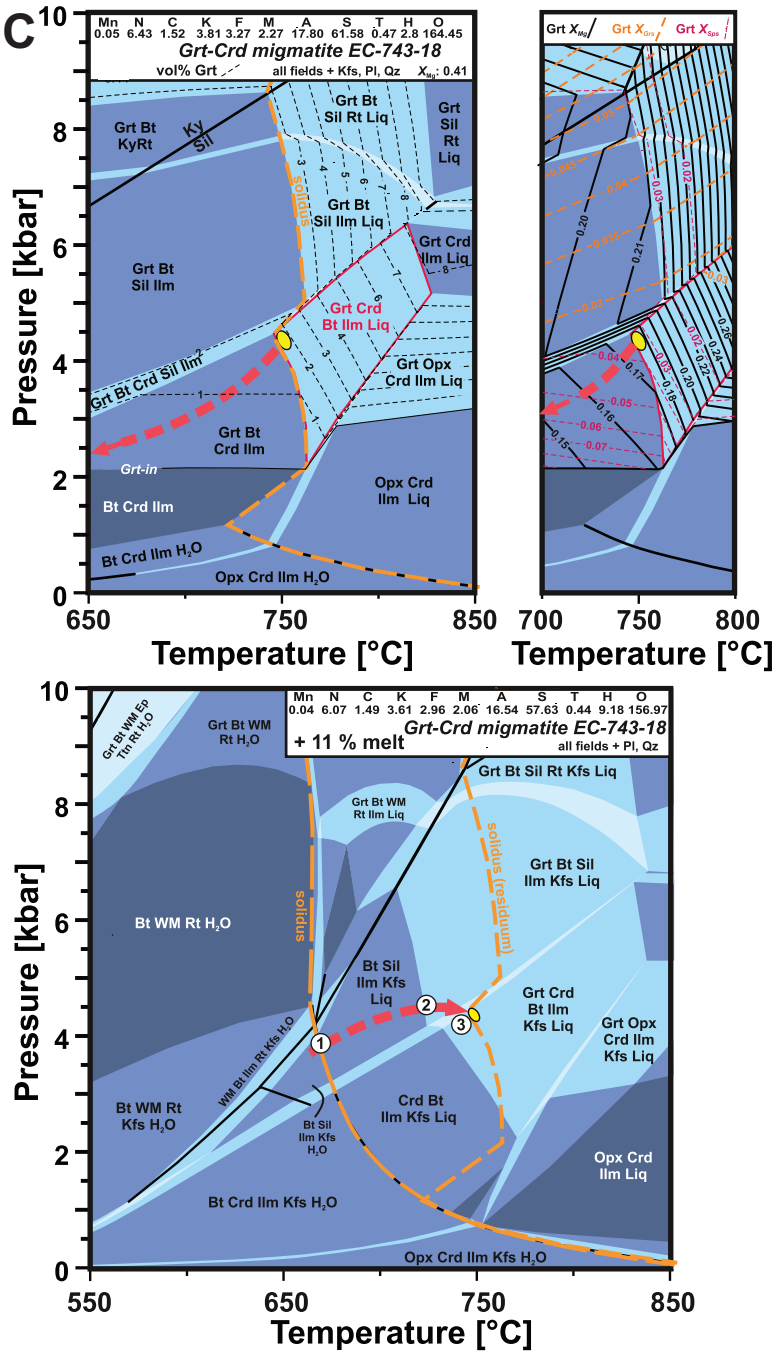

Fig. 6. Continued. (C) Grt-Crd migmatite EC-739-A-18 of the Eyao Unit. Field with red outline represent the inferred peak-metamorphic assemblage of the sample in the diagram for the residual composition that is contoured for the modal amount of garnet. The portion between 700–800 °C of the pseudosection is contoured in a separate diagram for the *X*Mg, *X*Grs and *X*Sps of garnet.

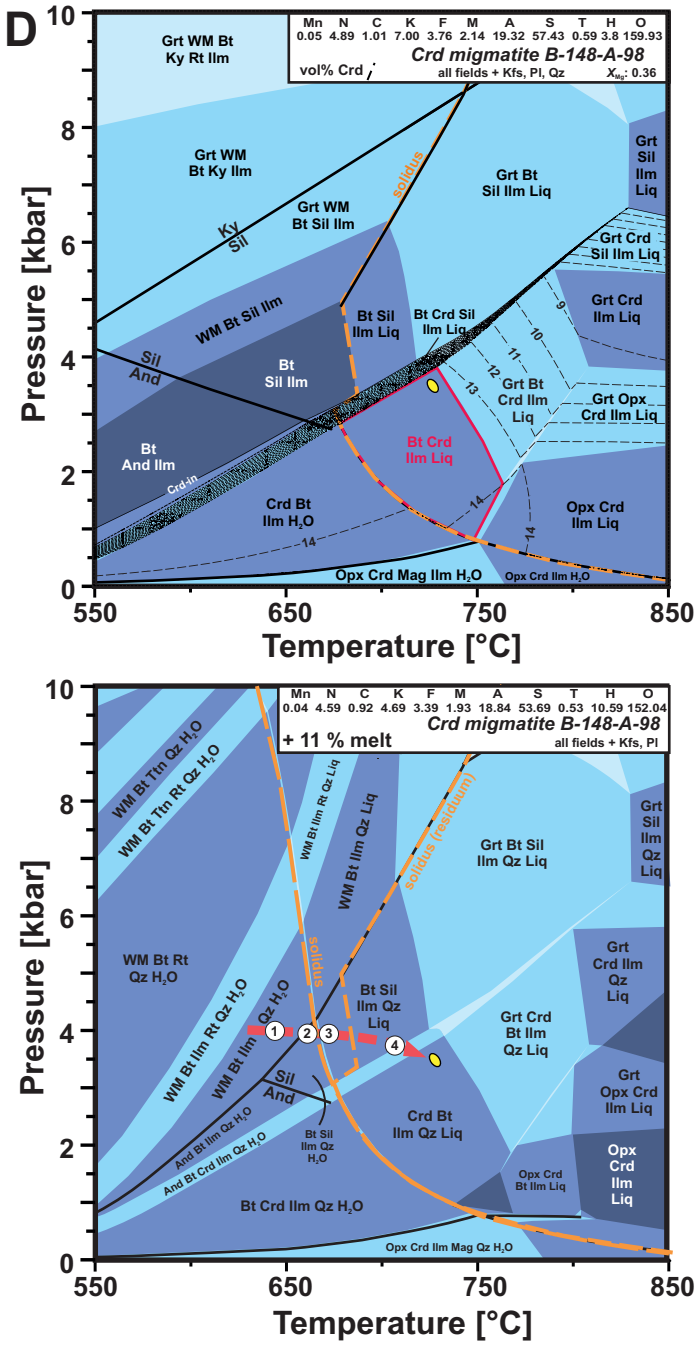

Fig. 6. Continued. (D) Crd migmatite B-148-A-98 of the Eyao Unit. Field with red outline represent the inferred peak-metamorphic assemblage of the sample in the diagram for the residual composition that is contoured for the modal amount of cordierite.

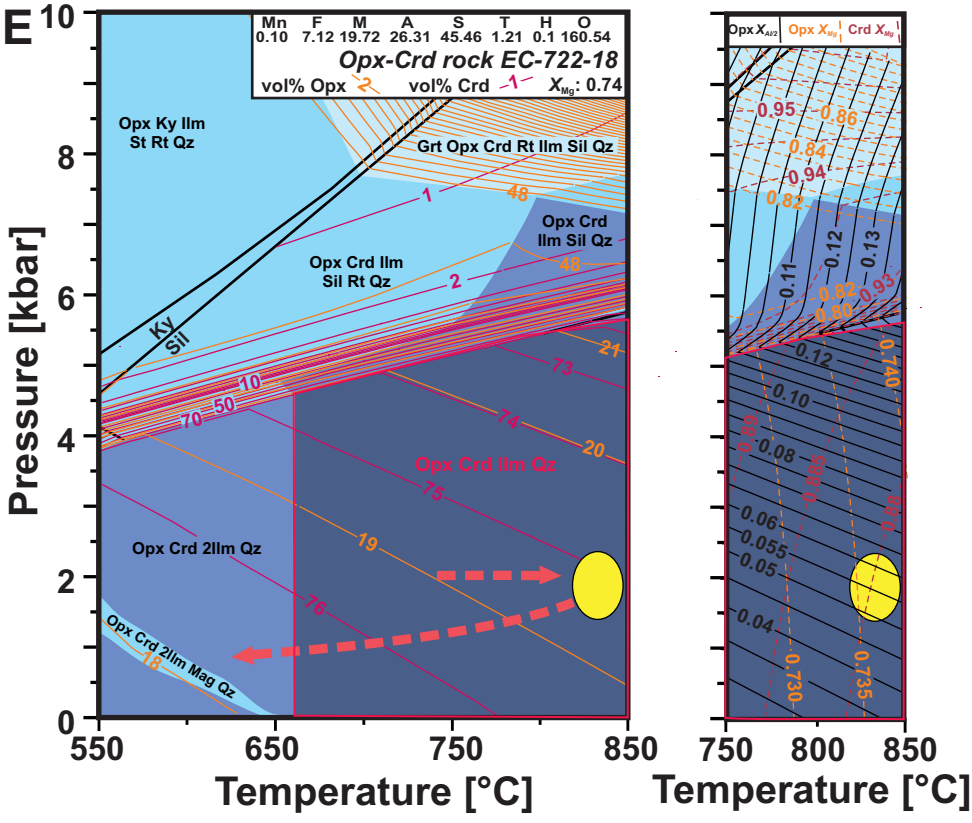

Fig. 6. Continued. (E) Opx-Crd rock EC-722-18 of the Eyao Unit (note different temperature scale) Field with red outline represent the inferred peak-metamorphic assemblage of the sample in the diagram that is contoured for the modal amount of cordierite and orthopyroxene. The portion between 750–850 °C of the pseudosection is contoured in a separate diagram for the *X*Mg and *X*Al/2 of orthopyroxene and *X*Mg in cordierite.

The estimated bulk rock compositions of the studied rocks (table A1) can be adequately expressed in the system MnNCKFMASHTO, since other components (for example, Zn, Cr) are present at trace element level and are not expected to have a significant impact on the topology of the pseudosections. The Ca content was adjusted to the presence of usually minor amounts of apatite.

The samples are affected by variably intense alteration, which is evident from pinitization, chloritization, saussuritization, and sericitization. This is also expressed by the high LOI (loss on ignition) values (table A1), indicating the infiltration of H_2O during the post-peak evolution or interaction with fluids released during crystallization of the melt. Consequently, the amount of H_2O in the bulk compositions was adjusted from the measured LOI value for all samples. The water contents used for the *P-T* pseudosection modelling were estimated by comparison of the observed mineral assemblages with those predicted on temperature versus molecular proportion of H diagrams (*T-H* diagrams) calculated for anhydrous ($H = 0$ mol%) to hydrous ($H =$ 10 mol%) conditions (see Raith and others, 2016; Jung and others, 2019 for details on the modeling). The diagrams were calculated for pressures of 4 (Eyao Unit) or 8 kbar (Orue Unit), based on the results of the thermobarometric calculations. The H value of the migmatites was constrained so that the observed peak-metamorphic assemblage

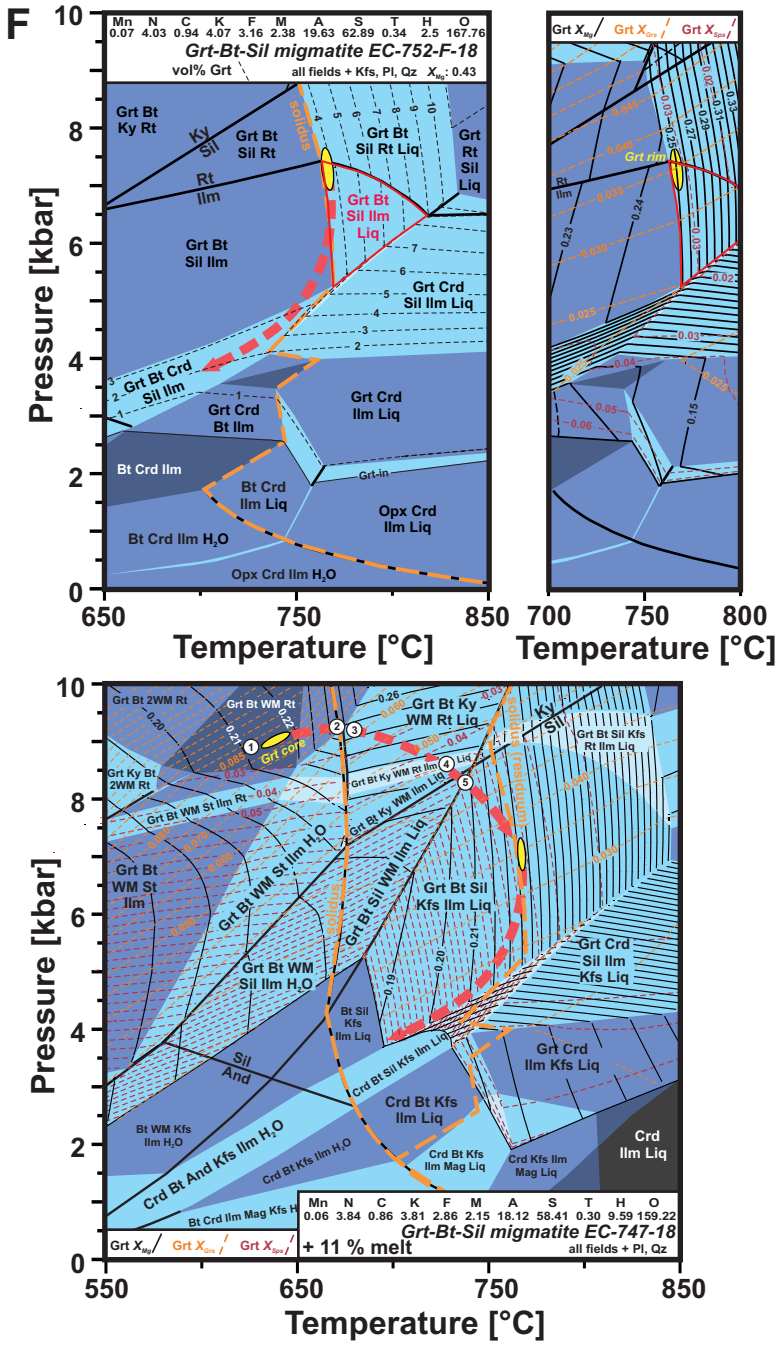

Fig. 6. Continued. (F) Grt-Bt-Sil migmatite EC-752-F-18 of the Orue Unit. Field with red outline represent the inferred peak-metamorphic assemblage of the sample in the diagram for the residual composition that is contoured for the modal amount of garnet. The portion between 700–800 °C of the pseudosection is contoured in a separate diagram for the *X*Mg, *X*Grs and *X*Sps of garnet. The melt reintegrated pseudosection is also contoured for the composition of garnet.

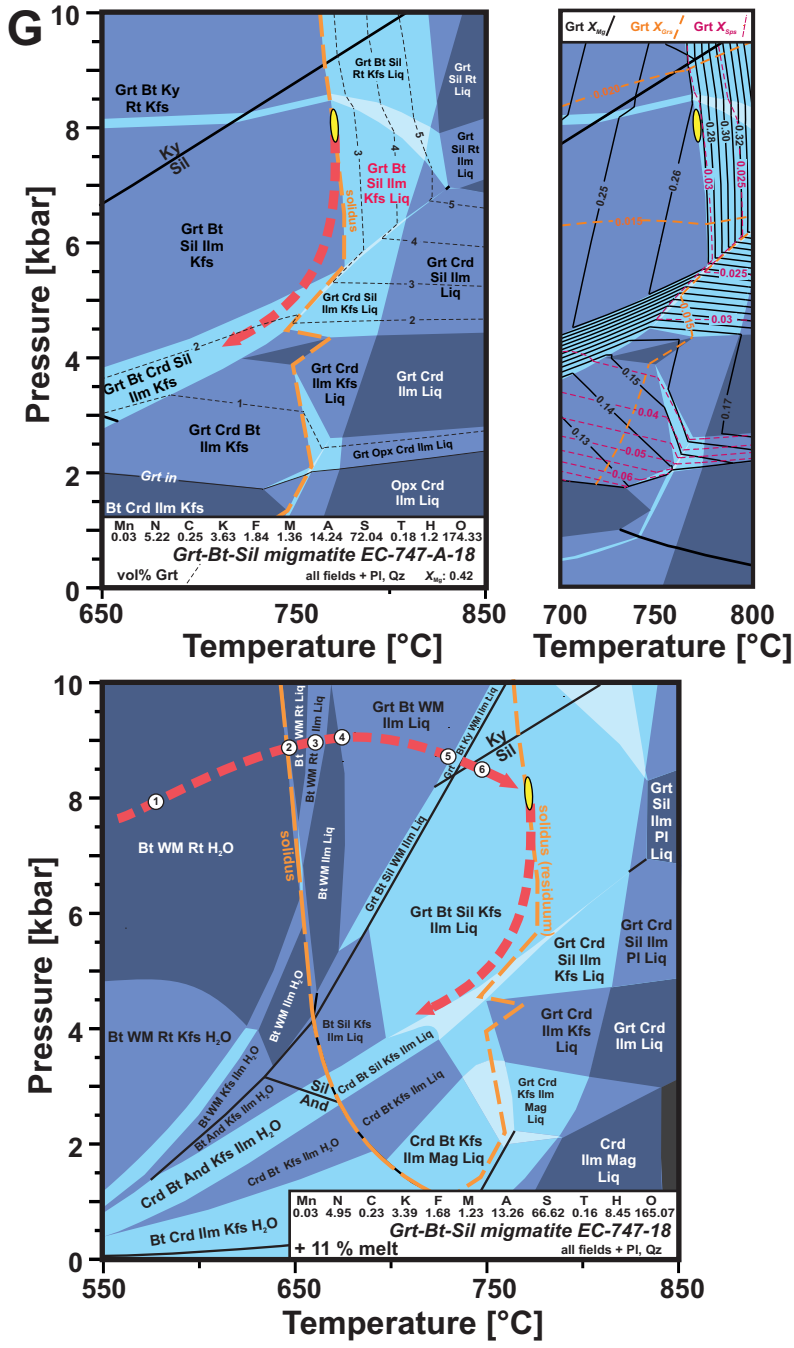

Fig. 6. Continued. (G) Grt-Bt-Sil migmatite EC-747-A-18 of the Orue Unit. Field with red outline represent the inferred peak-metamorphic assemblage of the sample in the diagram for the residual composition that is contoured for the modal amount of garnet. The portion between 700–800 °C of the pseudosection is contoured in a separate diagram for the *X*Mg, *X*Grs and *X*Sps of garnet.

is stable just above the solidus to reflect the conditions, where this assemblage is in equilibrium with anatectic melt (for example, White and others, 2007; Korhonen others, 2010). Isolines for the X_{Mg} of garnet were calculated to further refine the H value.

The appropriate O contents for the calculation of the *P–T* diagrams were evaluated for each sample using *T–M*$_O$ diagrams calculated at 4 (Eyao Unit) or 8 kbar (Orue Unit), and applying the adjusted H values (see Raith and others, 2016; Jung and others, 2019 for details on the modelling). M_O is equivalent to Fe^{3+}, representing the conversion of all Fe calculated as FeO to Fe_2O_3. The appropriate O (equivalent to the Fe^{3+}/Fe^{total} ratio) value was constrained by comparison of the observed peak metamorphic assemblage with those predicted from the *T–M*$_O$ diagrams (for example, Korhonen and others, 2010, Raith and others, 2016; Jung and others, 2019).

The migmatitic textures of the studied samples imply the loss of melt during the prograde evolution. Therefore, a set of *P-T* pseudosections was calculated at first using the bulk composition measured from the XRF data of the samples. As presumably some melt was removed during the prograde *P-T* evolution, the measured bulk compositions are residual, and therefore, these *P-T* pseudosections are valid for constraining the peak conditions and the early retrograde evolution of the rocks. To refine the *P-T* conditions during peak metamorphic conditions, the calculated phase diagrams were gridded with isopleths for the X_{Mg}, X_{Grs} and X_{Sps} of the garnet (metapelitic migmatites), as well as the X_{Mg} and $X_{Al/2}$ of the orthopyroxene (Opx-Crd rock), and for the modal amounts (estimated by point counting) of garnet (metapelitic migmatites) as well as cordierite and orthopyroxene (Opx-Crd rock and Crd migmatite).

To account for the melt loss, further *P-T* pseudosections were calculated after reintegrating melt to the measured residual bulk compositions, a reliable method to reconstruct a plausible prograde history for the melt-depleted migmatites by means of phase equilibria modeling (for example, Indares and others, 2008; White and others, 2014a; Bartoli, 2017). As the calculated peak-temperatures are only slightly above the solidus of the residual bulk rocks, we considered a simple scenario of melt loss in a single step at the intersection of the solidus for the residual composition with a presumed prograde *P–T* path following the method of Indares and others (2008). The composition of the melt, which was stable at the intersection (table 7), was calculated by THERIAK, and an amount of that melt, sufficient to just saturate the solidus in H_2O at a reference pressure of 3.5 kbar (Grt-Crd migmatites of the Eyao Unit), 2 kbar (Opx-Crd rocks of the Eyao Unit), or 8 kbar (Orue Unit), was added to the bulk composition (see Indares and others, 2008 for details of the method). The amount of reintegrated melt ranges from 11 to 18 mole percent. Mineral inclusion assemblages provide some evidence for the prograde segment of the *P–T* paths that were further refined for two samples (EC-739-A-18, EC-752-F-18) containing prograde zoned garnet through the application of garnet composition isopleths. The restitic compositions of the Opx-Crd rock preclude the estimation of the melt-composition and hence the reintegration of the lost melt.

Eyao Unit

Pseudosections were calculated for the three Grt-Crd migmatites (EC-731-18, EC-739-A-18, EC-743-18) and the Opx-Crd rocks EC-722-18. A garnet-free cordierite migmatite, which was collected during an earlier field campaign (sample B-148-A-98), was included in the calculations to study possible variations of the peak *P-T* conditions in the Eyao Unit.

Grt-Crd migmatite EC-731-18.—The inferred peak-metamorphic assemblage Grt-Crd-Sil-Bt-Kfs-Ilm-Pl-Qz coexisting with melt of sample EC-731-18 is stable in a narrow field

TABLE 7

Residual and melt-reintegrated bulk rock composition and composition and amount of reintegrated melt

	EC-731-18			EC-739-A-18			B-148-A-98			EC-743-18			EC-747-A-18			EC-752-F-18		
	residual bulk rock mol%	melt wt%	reintegrated bulk rock mol%	residual bulk rock mol%	melt wt%	reintegrated bulk rock mol%	residual bulk rock mol%	melt wt%	reintegrated bulk rock mol%	residual bulk rock mol%	melt wt%	reintegrated bulk rock mol%	residual bulk rock mol%	melt wt%	reintegrated bulk rock mol%	residual bulk rock mol%	melt wt%	reintegrated bulk rock mol%
SiO_2	62.03	56.12	56.81	53.14	56.17	48.40	57.43	53.95	53.69	61.58	55.83	57.63	72.04	50.07	66.62	62.89	50.55	58.41
TiO_2	0.48	0.00	0.42	0.71	0.00	0.61	0.59	0.00	0.53	0.47	0.00	0.43	0.18	0.00	0.16	0.34	0.00	0.30
Al_2O_3	18.88	10.73	17.07	24.27	10.64	21.31	19.32	10.05	17.84	17.80	10.99	16.54	14.24	10.68	13.26	19.63	10.66	18.12
FeO	4.54	0.26	3.96	6.36	0.23	5.40	3.76	0.09	3.39	3.27	0.47	2.96	1.85	0.44	1.68	3.16	0.39	2.86
MgO	2.40	0.04	2.09	2.44	0.04	2.07	2.14	0.02	1.93	2.27	0.10	2.06	1.36	0.12	1.23	2.38	0.10	2.15
Mn	0.18	0.00	0.16	0.28	0.00	0.24	0.05	0.00	0.04	0.05	0.00	0.04	0.03	0.00	0.03	0.07	0.00	0.06
CaO	0.53	0.17	0.47	0.77	0.21	0.67	1.01	0.15	0.92	1.52	0.20	1.49	0.25	0.12	0.23	0.94	0.29	0.86
Na_2O	3.41	2.70	3.23	3.15	2.47	2.96	4.89	2.57	4.59	6.43	2.88	6.07	5.22	3.74	4.95	4.03	3.12	3.84
K_2O	4.45	3.71	4.11	6.37	3.89	5.69	7.00	3.54	6.47	3.81	3.70	3.61	3.63	2.70	3.39	4.07	3.24	3.81
H_2O	3.10	26.27	11.68	2.50	26.36	12.65	3.80	29.62	10.59	2.80	25.83	9.18	1.20	32.13	8.45	2.50	31.65	9.59
total	100.00	100.00	100.00	100.00	100.00	100.00	100.00	100.00	100.00	100.00	100.00	100.00	100.00	100.00	100.00	100.00	100.00	100.00
T (°C)		721			715			690			745			770			765	
P (kbar)		3.5			3.5			3.5			4.5			8			7.5	
melt (mol %)			12			18			11			11						11

at H values > 2.5 mole percent (fig. A1.A). A value of 3.1 mole percent H was constrained through the XMg of the garnet (0.12) and the location of the solidus. Using this H value, a Fe^{3+}/Fe^{tot} ratio of 0.05, equivalent to 0.11 mole percent O, was estimated for the magnetite-free peak-assemblage, which is stable only at very low Fe^{3+}/Fe^{tot} (fig. A1.B).

The *P–T* pseudosection for the moderately Mg-rich metapelite EC-731-18 (bulk rock *X*Mg: 0.35) is characterized by the solidus at 720 to 750 °C (fig. 6). Garnet is present almost throughout the entire studied *P–T* space (except at very low pressures) and cordierite is stable up to pressures of 6 kbar. The peak-metamorphic assemblage Grt-Crd-Sil-Bt-Kfs-Ilm-Pl-Qz coexisting with melt is stable in a very narrow *P–T* field of 720 to 810 °C and 3.5 to 6.2 kbar. The estimated low modal abundance of garnet (4 vol%) is in agreement with the modeled value (3–4 vol% Grt) at the peak *P-T* conditions. The composition of garnet in the assemblage (*X*Mg: 0.12; *X*Grs: 0.02; X_{Sps}: 0.10–0.11) documents peak *P–T* conditions of 720 °C and 3.5 kbar, just within the stability field of the peak assemblage, and consistent with *P-T* data calculated by geothermobarometry (*ca.* 720 °C, 4 kbar; table 6). Due to the lack of garnet or cordierite replacement textures the retrograde evolution of the sample remains speculative.

In the melt-reintegrated pseudosection, calculated with 12 mole percent melt, the solidus is lowered to temperatures of *ca.* 660 to 670 °C and the stability of the micas is expanded whereas the stability of garnet is shifted to slightly higher pressures. Microtextures suggest that the Grt-Crd-bearing peak-assemblage formed through near-isobaric heating at low pressures (fig. 6): 1) Inclusions of white mica in K-feldspar document the almost complete replacement of early white mica through K-feldspar and additional sillimanite probably under subsolidus conditions of *ca.* 650 °C and 4 kbar; 2) Garnet-bearing leucosomes in the migmatitic sample record subsequent crossing of the solidus and entry into the Grt-Sil-Bt-Ilm-Kfs-Pl-Qz-Liq field at slightly higher temperatures of ~660 °C through continued heating; 3) Biotite-sillimanite-rich layers that are surrounded by cordierite-garnet assemblages indicate the subsequent partial replacement of the biotite-sillimanite assemblage. The formation of the coexisting Grt-Crd peak-assemblage records entry into the narrow Grt-Crd-Sil-Bt-Ilm-Kfs-Pl-Qz-Liq field at a temperature of ~700 °C through continued near-isobaric heating at 4 to 3.5 kbar in the sillimanite stability field.

Grt-Crd migmatite EC-739-A-18.—In the T-H diagram, the interpreted peak-metamorphic assemblage Grt-Crd-Sil-Bt-Kfs-Ilm-Pl-Qz-melt of sample EC-739-A-18 is stable at H values > 2.5 mole percent (fig. A1.C). A value of 4 mole percent H was constrained by correlating the X_{Mg} of the garnet (0.12) with the H value just above the solidus. The observed magnetite-free peak assemblage is stable only at very low Fe^{3+}/Fe^{tot} (fig. S1D) and a Fe^{3+}/Fe^{tot} ratio of 0.05, equivalent to 0.16 mole percent O, was used for the calculation of the P–T-pseudosection.

The *P–T* pseudosection for the metapelite EC-739-A-18 resembles that of sample EC-731-18 and is characterized by the solidus at 700 to 750 °C (fig. 6B). However, due to the slightly less magnesian composition (bulk rock X_{Mg}: 0.28), the stability of cordierite is reduced to > 5.5 kbar, compared to that of the metapelite EC-731-18 (bulk rock X_{Mg}: 0.35), and the garnet stability is expanded to low pressures. The peak-metamorphic assemblage Grt-Crd-Sil-Bt-Kfs-Ilm-Pl-Qz coexisting with melt is stable in a narrow *P–T* field of 700 to 800 °C and 3 to 5.5 kbar. The composition of the peak-metamorphic garnet rims (*X*Mg: 0.12; *X*Grs: 0.025; X_{Sps}: 0.09–0.10) refines the peak *P–T* conditions to 3.5 kbar and 720 °C. These conditions are consistent than those calculated by the geothermobarometry (*ca.* 710 °C and 4 kbar, table 6) and almost identical to those estimated by pseudosection modeling for sample EC-731-18. Furthermore, the modeled modal abundance of garnet at these conditions (4–5 vol% Grt) is in good agreement with the garnet abundance estimated by point counting

(6 vol% Grt). Rare Bt-WW-Qz intergrowths resorbing garnet suggest post-peak cooling to subsolidus conditions, but the lack of more *P-T* sensitive reaction textures prevents the reconstruction of a precise retrograde evolution.

Reintegration of 18 mole percent melt lowers the solidus to temperatures of *ca.* 660 °C in the pseudosection. The stability of white mica and biotite is expanded and staurolite becomes stable. By integrating the microtextures with the composition of prograde zoned garnet we constrained a possible *P-T* path for the prograde evolution: 1) inclusions of white mica, biotite, ilmenite, and quartz in garnet suggest an early mica-rich subsolidus assemblage Grt-Bt-WM-Ilm-Qz that is stable in a large field at 4.5 to 7 kbar and < 570 °C. The core composition of the garnet (*X*Mg: 0.08-0.09; *X*Grs: 0.125) is consistent with initial garnet growth under greenschist facies conditions (*ca.* 6 kbar, 450 °C). The spessartine content is higher (*X*Mg: 0.20) than the modeled value in the Grt-Bt-WM-Ilm-Qz field (X_{Sps}: 0.10). Since the measured value plots in the stability field of staurolite, which was not observed in this sample, the high Mn content is thought to be the result of re-equilibration during the further evolution; 2) the lack of white mica in the matrix that contains abundant sillimanite records the progressive replacement of white mica through Sil-forming reactions and entry into the Grt-Bt-WM-Sil-Ilm-Pl-Qz field through heating and minor decompression; 3) garnet-bearing leucosomes record the crossing of the solidus at *ca.* 660 °C, and 4) at slightly higher temperatures white mica was completely replaced as a matrix phase by K-feldspar (and additional sillimanite); 5) cordierite-garnet assemblages around the Bt-Sil-rich layers, and garnet and cordierite in the leucosomes of the migmatitic rock suggest the formation of the melt-bearing Grt-Crd peak-assemblage through biotite-sillimanite-breakdown melting reactions and entry into the narrow Grt-Crd-Bt-Sil-Ilm-Kfs-Pl-Qz-Liq field during further heating to peak-*P-T* conditions. The preservation of biotite and sillimanite provides an up-temperature limit.

Grt-Crd migmatite EC-743-18.—The T-H diagram documents the stability of the observed peak metamorphic assemblage Grt-Crd-Bt-Ilm-Kfs-Pl-Qz-Liq of sample EC-743-18 at H contents > 1.7 mole percent and temperatures of 670 to 760 °C (fig. S1E). Using the intersection of the solidus with the estimated XMg of garnet (0.17), a H value of 2.5 mole percent was constrained for further modeling. Using this value, the peak assemblage is stable at a temperature of 750 to 800 °C. In the T-MO diagram the absence of magnetite records a very low Fe^{3+}/Fe^{tot} ratio of ~ 0.05 (fig. S1F), which is equivalent to an O value of 0.15.

Despite the different bulk rock composition (less aluminous) the topology of the *P–T* pseudosection for the relatively Mg-rich (bulk rock *X*Mg: 0.41) metapelite EC-743-18 (fig. 6C) is similar to those of the metapelites EC-731-18 and EC-739-A-18. Owing to the relatively low H content, the solidus is shifted to high temperatures of 750 to 760 °C. The sillimanite-free peak-metamorphic assemblage Grt-Crd-Bt-Kfs-Ilm-Pl-Qz coexisting with melt is stable in a large *P–T* field of 750 to 830 °C and 2 to 6.5 kbar. Peak temperatures of 750 °C, just within the stability field of the peak-assemblage, are estimated from the composition of the peak-metamorphic garnet (*X*Mg: 0.17; *X*Grs: 0.025). These temperature conditions are slightly higher than those calculated by the geothermobarometry (~730 °C, table 6). The discrepancy between the measured (0.11) and modeled (0.03–0.04) X_{Sps} is related either to re-equilibration of the Mn content in the small garnets or to chemical inhomogeneity in the sample. The wide spacing of the grossular isopleths in the field prevents a refinement of the peak pressures. Retrograde garnet zoning (*X*Mg: 0.17–0.14 at the rims) is consistent with post-peak subsolidus cooling in the Grt-Crd-Bt-Ilm Kfs-Pl-Qz field.

In the melt-reintegrated pseudosection, calculated with 11 mole percent melt, the solidus is lowered to temperatures of *ca.* 660 °C and the stability of biotite and white mica is expanded, whereas the stability of garnet is reduced to higher pressures and

temperatures: 1) The garnet-bearing leucosomes indicate crossing of the solidus through heating to temperatures > 650 °C at the partial breakdown of an early subsolidus Bt-Sil-Ilm-Qz assemblage, which is preserved as inclusions in the cores of the cordierite; 2) the formation of garnet records continued heating to > 720 °C; and 3) the growth of porphyroblastic cordierite through consumption of the Bt-Sil inclusion assemblage documents entry into the Grt-Crd-Bt-Kfs-Ilm-Pl-Qz-Liq field of the peak-assemblage. The growth of cordierite caused the almost complete replacement of sillimanite that is only preserved as inclusions in the cordierite cores.

Crd migmatite B-148-A-98.—The observed peak-metamorphic assemblage Crd-Bt-Kfs-Ilm-Pl-Qz coexisting with melt of the relatively magnesian and aluminous (bulk rock XMg: 0.36) metapelite sample B-148-18 is stable in a narrow stability field at 660 to 670 °C in the T-H diagram (fig. A1.G). The assemblage is stable just above the solidus at a low H value of 3.8 mole percent. The magnetite-free peak assemblage is formed at very low Fe^{3+}/Fe^{tot} (fig. A1.H) and we have used a value of 0.05, which is equivalent to 0.10 mole percent O, for the calculation of the P–T pseudosection.

The *P–T* pseudosection for this metapelite sample is shown in figure 6D. The main features of the pseudosection include the solidus at moderate temperatures of ~680 to 750 °C and the restricted stability of garnet. which is absent at pressures < 6 kbar and temperatures < 700 to 750 °C. The observed garnet-free peak-assemblage Crd-Bt-Kfs-Pl-Ilm-Qz coexisting with melt defines a broad stability field at 670 to 760 °C and 0.7 to 3.8 kbar. The estimated amount of cordierite (13 vol%) is consistent with the modeled content of cordierite in the field. The peak-metamorphic conditions of *ca.* 730 °C and 3.5 kbar, as constrained from the garnet-bearing pelitic migmatites, just fall in the stability field of the peak-assemblage. The exceptional lack of garnet in this sample is, hence, consistent with the overall *P-T* conditions in the Eyao Unit and is related to the bulk rock composition of the sample.

The suprasolidus portion of the melt-reintegrated pseudosection, calculated with 11 mole percent melt, is similar to the diagram calculated for the estimated composition. The solidus is shifted only slightly to higher temperatures at pressures > 3 kbar. Microtextures suggest near-isobaric heating during the prograde evolution: 1) Inclusions of white mica, biotite and ilmenite in quartz and K-feldspar record an early WM-Bt-Ilm-Kfs-Pl-Qz assemblage that is stable at subsolidus conditions; 2) heating caused the complete replacement of white mica that is only preserved as very rare inclusions and the formation of sillimanite; 3) crossing of the solidus at *ca.* 665 °C during continued heating caused the formation of anatectic melt in the migmatite; 4) sillimanite inclusion trails in the cores of poly-crystalline cordierite and in K-feldspar that also enclose biotite and quartz record the progressive replacement of biotite-sillimanite-assemblages by cordierite and K-feldspar during continued melting reactions, which are evident from cordierite-bearing leucosomes. The textures document entry into the narrow Crd-Sil-Bt-Ilm-Kfs-Pl-Qz-Liq field during heating in the sillimanite stability field. Sillimanite-free cordierite margins suggest complete consumption of matrix sillimanite during cordierite growth and hence entry into the Crd-Bt-Ilm-Kfs-Pl-Qz-Liq field through continued heating to peak-metamorphic conditions.

Opx-Crd rock EC-722-18.—Based on its feldspar- and almost biotite-free peak-assemblage, the highly magnesian and restitic (bulk-rock XMg: 0.74) Opx-Crd rock sample was modeled in the MnFMASHTO system. Calcium is completely incorporated in abundant apatite (*ca.* 3 vol%) that is not included in the modeling, Na is incorporated in cordierite that is not included in the cordierite a-x model, and K is mainly induced (except rare biotite inclusions) during the retrograde evolution as displayed by the biotite coronas around orthopyroxene and cordierite.

The observed anhydrous peak-metamorphic assemblage Opx-Crd-Ilm-Qz is stable at low H values of < 4 mole percent and the entire studied temperature range (550–950 °C) in the *T-H* diagram (fig. S1I). The horizontal isopleths of the *X*Mg in Opx in the *T-H* space prevent a precise estimation of the H value and therefore a low value of 0.1 H mole percent was used for the further calculations, since the very high totals of the cordierite analyses suggest near-anhydrous conditions during peak-metamorphism. The observed magnetite-free peak assemblage is stable in a very large field in the *T-*Fe^{3+}/Fe^{tot} binary diagram (fig. A1.J). Therefore, isopleths for the *X*Mg in orthopyroxene were calculated to refine the Fe^{3+}/Fe^{tot} ratio. The composition of orthopyroxene in the sample (*X*Mg: > 0.735) indicates a high Fe^{3+}/Fe^{tot} ratio (~17) and the equivalent value of 0.61 mol% O was used for the calculation of the *P–T*-pseudosection.

Owing to the highly magnesian composition the *P-T* pseudosection of the Opx-Crd rock (fig. 6E) is markedly different when compared to those of the Grt-Crd migmatites. The stability of cordierite is enlarged up to > 10 kbar at temperatures > 750 °C and the stability of garnet restricted to pressure > 7 kbar. Opx-Sil/Ky assemblages are stable at pressure > 6 kbar, which is typical for such highly-magnesian metapelites (for example, Brandt and others, 2011; Kelsey and Hand, 2015). The observed restitic magnetite-free Opx-Crd-Ilm-Qz peak-assemblage is stable in a large field at low pressures of 0 to 5.5 kbar and > 660 °C. Due to the composition of orthopyroxene (*X*Mg: 0.737, $X_{Al/2}$: < 0.055) and cordierite (X_{Mg}: 0.88) the peak *P-T* conditions are refined to *ca.* 830 °C and 2 kbar, corresponding to the granulite facies. The exsolution of magnetite from ilmenite is consistent with cooling into the stability field of magnetite, consistent with near isobaric cooling to < 650 °C. The estimated high modal amount of cordierite (75 vol%) and lower amount of coexisting orthopyroxene (19 vol%) are consistent with the modeled values at the deduced peak conditions.

Orue Unit

Grt-Bt-Sil migmatite EC-752-F-18.—The peak-metamorphic assemblage Grt-Bt-Sil-Kfs-Ilm-Pl-Qz coexisting with melt of sample EC-752-F-18 is stable at moderate H values between 1 to 3.2 mole percent at temperatures of 715 to 780 °C (fig. A1.K). A value of 2.5 mole percent H was constrained through the intersection of the isopleth of the analyzed garnet composition (XMg: 0.25) with the solidus of the peak-assemblage. Using this H value, a Fe^{3+}/Fe^{tot} ration of 0.05, equivalent to 0.08 mole percent O, was estimated for the magnetite-free peak assemblage, which is stable only at low Fe^{3+}/Fe^{tot} (fig. S1L).

The *P–T* pseudosection for the relatively Mg-rich metapelite EC-752-F-18 (fig. 6F) is similar to the diagrams calculated for the Grt-Crd migmatites of the Eyao Unit. The solidus is located at a temperature of *ca.* 750 °C. Owing to the more relatively magnesian composition (bulk rock *X*Mg: 0.43), the stability of cordierite is slightly expanded up to 7 kbar, compared to the metapelites of the Eyao Unit (bulk rock *X*Mg: 0.28–0.41). The inferred peak-metamorphic assemblage Grt-Bt-Sil-Kfs-Ilm-Pl-Qz coexisting with melt of metapelite EC-752-F-18 is stable in a narrow *P–T* field of 760 to 820 °C and 5.2 to 7.3 kbar, but the composition of the peak-metamorphic garnet rims (*X*Mg: 0.25; *X*Grs: 0.04-0.03; X_{Sps}: 0.03) refines the peak *P–T* conditions at 765 °C and 7.3 kbar. These conditions are consistent with the low modal abundance of garnet (Grt: 4 vol%), but are slightly lower than those calculated by the geothermobarometry (~780 °C at 8 kbar, table 6).

The development of cordierite coronas around garnet, separating it from sillimanite, record the growth of cordierite at the expense of garnet. The lack of cordierite-bearing leucosomes suggests the formation of coronitic cordierite at subsolidus conditions in the Grt-Crd-Sil-Ilm-Kfs-Pl-Qz field, consistent with decompression to < 5 kbar

subsequent to peak-metamorphism. Decompression agrees with the growth of plagioclase rims between garnet and sillimanite (progress of the GASP reaction).

In the melt-reintegrated pseudosection, calculated with 11 mol% melt, the solidus is lowered to temperatures of *ca.* 660 to 670 °C and the stability of white mica is significantly expanded. The sample preserves some evidence of the prograde segment of the *P–T* path, which may be reconstructed through constraints from the melt-reintegrated pseudosection: 1) Inclusions of biotite, rutile, and quartz in the poikiloblastic garnet cores, and high grossular contents in the garnet cores (*X*Grs: up to 0.085) suggest that the prograde evolution proceeded at elevated pressures > 7.5 kbar. The calculated X_{Mg} and X_{Sps} of the garnet core (*X*Mg: 0.216, X_{Sps}: 0.025) are also consistent with the modeled values in the Grt-Bt-WM-Rt-Pl-Qz field; 2) garnet-bearing leucosomes record crossing of the solidus at *ca.* 660 °C during subsequent heating that is also consistent with rimward decreasing grossular in the garnet; 3) kyanite inclusions in plagioclase as well as matrix kyanite, which was transformed to sillimanite, record further heating; and 4) the growth of matrix ilmenite at the expense of rutile documents that continued heating was associated by minor decompression; 5) the sillimanite pseudomorphs after kyanite document the subsequent crossing of the kyanite-sillimanite transformation during decompression-heating and additional sillimanite was formed together with K-feldspar in the matrix presumably through the complete replacement of white mica, resulting in the observed peak-assemblage Grt-Bt-Sil-Ilm-Kfs-Pl-Qz-Liq. Combining the prograde with the retrograde segment of the *P-T* path documents a clockwise evolution with post-peak decompression of about 3 kbar.

Grt-Bt-Sil migmatite EC-747-A-18.—In the binary T-H diagram the inferred peak-metamorphic assemblage Grt-Bt-Sil-Kfs-Ilm-Pl-Qz- melt of sample EC-747-A-18 is stable at H values > 0.6 mole percent and a temperature range of 700 to 760 °C (fig. S1M). A low value of 1.2 mole percent H was constrained by correlating the analyzed garnet core composition (XMg: 0.26) with the H value just above the solidus. The observed magnetite-free peak assemblage is stable only at low Fe^{3+}/Fe^{tot} (fig. A1.N). Consequently, a Fe^{3+}/Fe^{tot} ratio of 0.05, equivalent to 0.05 mole percent O, was used for the calculation of the P–T-pseudosection.

Despite the higher Si and lower Al and Ca contents of sample EC-747-A-18 the *P–T* pseudosection (fig. 6G) is similar to that of metapelite sample EC-752-F-18. Due to the low H content the solidus is located at high temperatures of 760 to 770 °C, and cordierite is stable up to 7 kbar at suprasolidus conditions and at 3 to 5.5 kbar at subsolidus conditions. Except at low pressure conditions, garnet is stable over the entire investigated *P–T* field. The observed peak-metamorphic assemblage Grt-Bt-Sil-Ilm-Kfs-Pl-Qz-Liq is stable just above the solidus in a narrow *P–T* field of 770 to 820 °C and 5.5 to 8.5 kbar. Using the analyzed garnet core compositions (*X*Mg:0.26, *X*Grs: 0.015–0.2, *X*Sps: 0.03-0.04), peak conditions are refined to 7.5 to 8.3 kbar and 770 °C, thus displaying slightly lower temperatures than calculated by geothermobarometry (~820°C). The low modal amount of garnet (3 vol%) is consisting with the modeled value at peak conditions in the field. Cordierite coronas around garnet and the lack of anatectic cordierite imply entry into the Grt-Crd-Bt-Sil-Ilm-Kfs-Pl-Qz stability field during post-peak decompression to P < 5 kbar at subsolidus condition (T< 750 °C).

Reintegration of 11 mole percent melt caused a lowering of the solidus to *ca.* 650 °C in the pseudosection and white mica becomes stable at subsolidus conditions. Constraints on the prograde *P–T* evolution are placed by interpreting the observed sequence of microtextures: 1) Rutile inclusions in feldspars and quartz, white mica in quartz, and biotite in garnet suggest an early Bt-WM-Rt assemblage; 2) heating caused partial melting through crossing of the solidus at *ca.* 650 °C; 3) inclusions of ilmenite record continued heating into the ilmenite-stability field; 4) at temperatures of 670 °C garnet enters the assemblage, and 5) at 720 °C and *ca.* 8.5 kbar kyanite formed,

probably at the progressive consumption of white mica; 6) continued heating caused the transformation of kyanite to sillimanite, evident from sillimanite pseudomorphs after kyanite, and additional sillimanite grows through the replacement of white mica, resulting in the observed peak-assemblage Grt-Bt-Sil-Ilm-Kfs-Pl-Qz-Liq. The reconstructed *P-T* path resembles the clockwise evolution of sample EC-752-F-18.

U-PB ZIRCON DATA

Eight samples were selected for SHRIMP U-Pb spot analyses. Sample location, rock type, and essential information on zircon morphology, chemistry and textures, their interpretation, and the zircon ages are given in table 8 and the entire U-Pb data set is presented in table 9. Zircons in the migmatite samples EC-731-18, EC-739-A-18, and B-394-1-99, the Opx-Crd rock EC-722-18, and the pelitic leucosome EC-727-18, are expected to provide constraints on the timing of partial melting and high-grade metamorphism in the Eyao Unit. In addition, inherited detrital zircon may preserve additional information on the age and sources of the sedimentary protoliths.

The Grt-Bt-Sil migmatite EC-747-A-18 and related leucosome sample EC-747-C-18 were selected to detect a possible poly-metamorphic evolution in the southern part of the Epupa Complex.

Eyao Unit

Grt-Crd migmatite EC-731-18.—A total of 26 spot analyses were undertaken on 22 zircon grains. Most of the usually euhedral to subhedral grains with aspect ratios of 1:2 to 1:4 display core-rim relationships (figs. 7A–7C). The cores are often surrounded by a narrow corona of highly luminescent zircon (figs. 7A and 7C) that is too narrow for analysis. This corona is followed by low-luminescent rims of strongly variable size, ranging from a few μm up to 100 μm. The cores usually show oscillatory zoning or sector-zoning, and high luminescence (figs. 7A and B). They have high Th/U ratios (0.28-1.30) and yield concordant to discordant $^{207}Pb/^{206}Pb$ ages ranging between 1898 ± 20 and 1786 ± 26 Ma (figs. 8A and 9A, ignoring > 1% discordant data). Three concordant core analyses define an age of 1877 ± 29 Ma (fig. 8B) and two other analyses an age of 1801 ± 17 Ma.

The weakly luminescent rims are unzoned or patchy-zoned and truncate the oscillatory zoning of the cores (figs. 7A and 7C) or form conformable to the cores (fig. 7B). Several rims show relics of a sector zoning (figs. 7A and 7C) that was modified by metamictization. The rims have very low Th/U ratios (0.07-0.01; fig. 9A) and yield mostly discordant $^{207}Pb/^{206}Pb$ ages (1771–1265 Ma) that define a Discordia with upper and lower intercepts at 1738 ± 20 Ma and 567 ± 57 Ma, respectively (fig. 8C).

Grt-Crd migmatite EC-739-A-18.—Nineteen spots on 18 zircon grains with aspect ratios of 1:3 to 1:1 were analyzed. CL images reveal distinct core-relationships in most zircons (figs. 7D–7F). Bright oscillatory-zoned zircon forms long to short-prismatic subhedral to euhedral grains (fig. 7D) or cores of zoned zircon (figs. 7E and 7F) with high Th/U ratios (0.28–1.23; fig. 9B). The $^{207}Pb/^{206}Pb$ ages range between 1828 ± 17 Ma to 1774 ± 16 Ma (ignoring > 1% discordant data, fig. 8D) and four concordant analyses define a Concordia age of 1786 ± 16 Ma (fig. 8E).

The cores of zoned grains are often resorbed and surrounded by a narrow highly luminescent corona that is followed by weakly luminescent unzoned or patchy-zoned rims of variable size (figs. 7D–7F). The rims often form euhedral to subhedral grains (fig. 7F) and have very low Th/U ratios (0.01–0.06; fig. 9B). Locally, relics of fine-scale oscillatory zoning are preserved (fig. 7F). The strongly discordant data of the zircon rims define an upper intercept at 1731 ± 77 Ma and a poorly defined lower intercept at 599 ± 160 Ma (fig. 8F).

TABLE 8

Sample locations, description of zircon textures under CL, the corresponding U-Pb ages of zircon growth and geological interpretation of the age data

Sample	Rock type	GPS coordinates	Zircon populations & textures under cathodoluminescence (CL)	Th/U	Ages (Ma)	Interpretation of zircon growth	Geological interpretation
EC-731 -18	Grt-Crd migmatite	S 16°59.095'	Two main populations of zircons were distinguished:				
		E 13°1.542'	(1) Resorbed cores (up to 150 µm in length) are moderately to highly luminescent and show oscillatory-zoning or growth-banding (Fig. 7A-C).	0.28-1.30	(1) Concordant $^{207}Pb/^{206}Pb$ ages 1898-1786 Concordia ages: 1877 ± 29 & 1801 ± 17	(1) Magmatic	(1) Detrital magmatic grains Deposition < 1800 Ma
			(2) Broad unzoned or patchy- to sector-zoned rims that truncate the early zoning form usually euhedral short- to long prismatic Cl-dark (U-rich) grains (Fig7A-C). A thin highly luminescent corona separate the two domains (Fig. 7A-C)	0.01-0.07	(2a) Upper-intercept age 1738 ± 20	(2a) Anatectic & metamorphic	(2a) Mid-amphibolite facies metamorphism & partial melting
					(2b) Lower-intercept age 567 ± 57	(2b) Fluid influx?	(2b) Hydrothermal overprint
EC-739 -A-18	Grt-Crd migmatite	S 16°59.043'	Two main zircon populations are identified:				
		E 13°1.540'	(1) Oscillatory-zoned or growth-banded highly luminescent subhedral to euhedral grains or cores (Fig. 7D-F)	0.28-1.23	(1) Concordant $^{207}Pb/^{206}Pb$ ages 1828-1774 Concordia age: 1786 ± 16	(1) Magmatic	(1) Detrital magmatic grains Deposition < 1774 Ma
			(2) Weakly luminescent, unzoned or patchy- to sector-zoned rims surround the cores and may form euhedral grains (Fig. 7D-F). A thin highly luminescent corona may occur between cores and rims (Fig. 7F)	0.01-0.06	(2a) Upper-intercept age 1731 ± 77	(2) Anatectic & metamorphic	(2a) Mid-amphibolite facies metamorphism & partial melt.
					(2b) Lower-intercept age 599 ± 160		(2b) Hydrothermal overprint
EC-727 -18	Leucosome of Grt-Crd migmatite	S 17°0.003'	CL images reveal two populations of zircon in the sample:				
		E 13°0.807'	(1) Rare, highly luminescent and oscillatory-zoned cores of zoned zircon or euhedral grains (Fig. 7G).	0.59-0.63	(1) Concordant $^{207}Pb/^{206}Pb$ age 1807 ± 17	(1) Magmatic	(1) Detrital magmatic grains Deposition < 1800 Ma
			(2) Unzoned or patchy- to oscillatory-zoned, weakly luminescent zircon forms rims around zoned zircon (Fig. 7G) and anhedral to subhedral grains (Fig. 7H & I).	0.01-0.07	(2a) Upper-intercept age 1722 ± 7.5	(2) Anatectic & metamorphic	(2a) Mid-amphibolite facies metamorphism & partial melting
					(2b) Lower-intercept age 468 ± 64		(2b) Thermal overprint
B-394 -1-99	Grt-Bt migmatite	S 16°59.258'	CL imaging reveals two distinct types of zircon:				
		E 13°5.023'	(1) Oscillatory-zoned and moderatel to highly luminescent zircon forms sub- to euhedral grains and cores of zoned zircon (Fig. 7J & K).	0.22-0.83	(1) Concordia age: 1837 ± 7	(1) Magmatic	(1) Detrital magmatic grains Deposition < 1830 Ma
			(2) Unzoned, weakly luminescent zircon rims surrounds and may resorb the oscillatory zoned domains (Fig. 7K & L). A thin highly luminescent corona may separate the two domains (Fig. 7K)	0.01-0.27	(2a) Upper-intercept age 1714 ± 180	(2) Anatectic & metamorphic	(2a) Mid-amphibolite facies meta.
					(2b) Lower-intercept age 495 ± 130		(2b) Fluid influx

TABLE 8
(continued)

Sample	Rock type	GPS coordinates	Zircon populations & textures under cathodoluminescence (CL)	Th/U	Ages (Ma)	Interpretation of zircon growth	Geological interpretation
EC-722-18	Opx-Crd rock	S 17°0.759'	Three distinct zircon populations are recognized:	0.73-1.22	(1) Concordant $^{207}Pb/^{206}Pb$ ages 1828-1780	(1) Magmatic	(1) Detrital magmatic grains
		E 12°58.907'	(1) Euhedral to anhedral, highly to poorly luminescent and oscillatory-zoned or growth-banded grains or cores (Fig. 7M-O).		(1a) Concordant $^{207}Pb/^{206}Pb$ age 1828 ± 14 (1b) Concordia age 1784 ± 9		Deposition < 1780 Ma
			(2) Unzoned, moderately luminescent rims may resorb the cores (Fig. 7N)	0.55	(2) Concordant $^{207}Pb/^{206}Pb$ age 1752 ± 30	(2) Metamorphic	(2) High grade metamorphism
			(3) A second and dominant generation of weakly luminescent, unstructured or sector-zoned rims may occur around the oscillatory-zoned grains (Fig. 7O).	0.07-0.35	(3) Concordia age 1533 ± 26	(3) Metamorphic	(3) Main granulite facies metamorphism
EC-747-A-18	Grt-Bt-Sil-migmatite	S 17°28.056'	All zircons show core-rim-relationships that are related to two populations of zircon:				
		E 13°14.547'	(1) Strongly resorbed small cores which are highly luminescent and oscillatory-zoned (Fig. 7P-R).	0.41-0.75	(1) Concordant $^{207}Pb/^{206}Pb$ ages: 1841-1696	(1) Magmatic	(1) Detrital magmatic grains: Deposition < 1700 Ma
			(2) Unzoned or sector-zoned rims may resorb the cores and from sub- to euhedral long- to short-prismatic grains (Fig. 7N).	0.01-0.06	(2) Upper-intercept age 1331 ± 8 (2) Concordia age 1323 ± 10	(2) Anatectic & metamorphic	(2) Upper-amphibolite facies metamorphism & partial melting
EC-747-C-18	Leucosome of Grt-Bt-Sil-migmatite	S 17°28.056'	CL revealed two generations of oscillatory-zoned zircon				
		E 13°14.547'	(1) Strongly resorbed small cores which are highly luminescent and oscillatory-zoned (Fig. 7S & T).	0.34-1.02	(1a) Concordant $^{207}Pb/^{206}Pb$ ages: 1851-1758 (1b) Concordant $^{207}Pb/^{206}Pb$ age: 1541	(1) Magmatic	(1) Detrital magmatic grains: Deposition < 1540 Ma ?
			(2) Oscillatory-zoned or growth-banded zircon with weak luminsecence may resorb the cores and/or forms sub- to euhedral long- to short-prismatic grains (Fig. 7S & U).	0.01-0.05	(2) Upper-intercept age 1334 ± 10 (2) Concordia age 1336 ± 5	(2) Anatectic & metamorphic	(2) Upper-amphibolite facies metamorphism & partial melting

TABLE 9

U-Pb zircon data of metasediments from the Epupa Complex

Spot	Texture	Zoning	U (ppm)	Pb (ppm)	$^{232}Th/^{238}U$	$^{206}Pb_c$ (%)	$^{206}Pb^*$ (ppm)	Isotopic ratios $^{207}Pb^*/^{206}Pb^*$	±1s (%)	$^{207}Pb^*/^{235}U$	±1s (%)	$^{206}Pb^*/^{238}U$	±1s (%)	rho[a]	Ages (Ma) $^{206}Pb/^{238}U$	±1s (Ma)	$^{207}Pb/^{206}Pb$	±1s (Ma)	disc.[b]
Grt-Crd migmatite EC-731-19																			
1.1	rim	sector	677	15	0.02	1.30	114	0.1075	0.75	2.57	2.6	0.1939	2.0	.767	1,142	21	1,554	32	26
2.1	core	oscillatory	122	74	0.62	0.94	35.3	0.1223	1.3	5.23	3.1	0.3323	2.2	.705	1,849	35	1,865	39	1
2.2	rim	sector	651	10	0.02	0.59	147	0.1086	1.2	3.72	2.5	0.2607	2.0	.822	1,493	27	1,687	26	11
3.1	rim	patchy	648	42	0.07	0.18	117	0.09824	0.67	2.79	2.2	0.2093	2.0	.927	1,225	23	1,561	15	22
4.1	core	oscillatory	119	80	0.70	0.04	35.6	0.1119	1.2	5.35	2.5	0.3477	2.2	.870	1,924	37	1,824	23	-5
4.2	rim	patchy	621	7	0.01	0.16	151	0.1049	0.88	4.02	2.2	0.2815	2.0	.905	1,599	29	1,687	18	5
5.1	core	oscillatory	92	116	1.30	2.62	26.8	0.1366	1.3	5.17	4.6	0.3296	2.3	.500	1,837	37	1,859	72	1
6.1	grain	oscillatory	63	68	1.11	0.30	17.8	0.1124	1.7	4.97	3.3	0.3286	2.3	.711	1,832	37	1,795	42	-2
7.1	rim	unzoned	696	15	0.02	1.00	119	0.1095	2.2	2.75	3.3	0.1979	2.1	.624	1,164	22	1,640	48	29
8.1	rim	unzoned	700	6	0.01	0.05	175	0.1038	0.54	4.15	2.1	0.2912	2.0	.962	1,648	29	1,686	11	2
9.1	core	oscillatory	172	113	0.68	0.51	47.9	0.1136	1.0	4.85	2.6	0.3220	2.1	.825	1,800	33	1,786	26	-1
10.1	rim	sector	623	4	0.01	0.05	149	0.1051	0.57	4.02	2.1	0.2785	2.0	.954	1,584	28	1,708	12	7
11.1	grain	oscillatory	164	95	0.60	0.05	50.8	0.1181	0.96	5.84	2.3	0.3603	2.1	.909	1,983	36	1,921	17	-3
12.1	core	oscillatory	193	123	0.66	0.11	57.7	0.1116	0.95	5.31	2.3	0.3482	2.1	.899	1,926	35	1,810	19	-6
13.1	core	sector	153	102	0.69	0.09	45.2	0.1170	1.0	5.49	2.4	0.3427	2.1	.888	1,900	35	1,898	20	0
14.1	core	oscillatory	185	158	0.88	3.16	38.3	0.1344	1.0	3.44	4.2	0.2332	2.1	.511	1,351	26	1,748	66	23
14.2	rim	sector	653	15	0.02	0.52	123	0.1018	0.66	2.92	2.2	0.2178	2.0	.899	1,270	23	1,573	18	19
15.1	rim	patchy	794	8	0.01	0.32	114	0.09187	0.69	2.05	2.2	0.1668	2.0	.904	994	18	1,407	18	29
16.1	rim	sector	515	7	0.01	0.47	143	0.1124	0.61	4.81	2.2	0.3220	2.0	.920	1,800	32	1,771	16	-2
17.1	core	oscillatory	119	76	0.66	0.75	26.5	0.1112	1.4	3.71	3.2	0.2572	2.2	.691	1,476	29	1,708	42	14
17.2	rim	unzoned	638	5	0.01	0.08	152	0.1046	0.60	3.97	2.1	0.2772	2.0	.950	1,577	28	1,695	12	7
18.1	core	oscillatory	139	38	0.28	0.50	34.2	0.1128	1.2	4.26	2.7	0.2847	2.1	.786	1,615	31	1,774	31	9
19.1	core	oscillatory	152	110	0.75	1.50	40.5	0.1203	1.2	4.53	3.1	0.3060	2.1	.680	1,721	32	1,754	42	2
20.1	rim	patchy	645	44	0.07	1.74	134	0.1187	0.81	3.38	2.8	0.2370	2.0	.718	1,371	25	1,689	37	19
21.1	rim	unzoned	737	10	0.01	0.25	91.1	0.08489	0.87	1.64	2.3	0.1435	2.0	.865	864	16	1,265	23	32
22.1	rim	sector	597	12	0.02	0.08	135	0.1031	0.59	3.70	2.1	0.2623	2.0	.952	1,501	27	1,668	12	10
Grt-Crd migmatite EC-739-A-18																			
1.1	grain	oscillatory	209	119	0.59	0.05	63.9	0.1139	0.73	5.57	3.3	0.3560	3.2	.971	1,963	55	1,856	14	-6
2.1	core	oscillatory	290	196	0.70	0.12	84.7	0.1111	0.65	5.15	3.3	0.3400	3.2	.976	1,885	53	1,800	13	-5
2.2	rim	unzoned	836	5	0.01	0.34	103	0.0825	0.67	1.56	3.4	0.1423	3.2	.954	858	26	1,187	20	28
3.1	core	oscillatory	134	160	1.23	0.39	36.3	0.1102	0.99	4.61	3.7	0.3130	3.4	.934	1,756	53	1,745	24	-1
4.1	grain	oscillatory	627	580	0.96	0.92	99.1	0.1099	0.62	2.56	3.6	0.1824	3.2	.897	1,080	32	1,659	29	35
5.1	grain	oscillatory	302	83	0.28	0.11	87.2	0.1127	0.88	5.17	3.4	0.3360	3.3	.960	1,866	53	1,828	17	-1
6.1	rim	patchy	722	43	0.06	0.42	137	0.1037	0.60	3.03	3.3	0.2194	3.2	.964	1,279	37	1,626	±16	21
7.1	grain	oscillatory	182	80	0.45	0.04	49.9	0.1088	0.86	4.78	3.4	0.3200	3.3	.965	1,787	51	1,774	±16	-1
8.1	rim	patchy	632	18	0.03	0.31	135	0.1027	0.53	3.42	3.3	0.2481	3.2	.977	1,429	41	1,624	±13	12
9.1	rim	unzoned	667	8	0.01	0.16	175	0.1057	0.55	4.38	3.3	0.3045	3.2	.981	1,714	48	1,703	±12	-1
10.1	grain	oscillatory	213	222	1.08	--	66.2	0.1141	0.71	5.71	3.3	0.3620	3.3	.977	1,994	56	1,868	±13	-7
11.1	core	growth-banding	262	167	0.66	0.14	76.7	0.1103	0.70	5.12	3.3	0.3410	3.3	.973	1,890	53	1,783	±14	-6
12.1	rim	oscillatory	707	28	0.04	0.17	149	0.1039	0.52	3.47	3.3	0.2456	3.2	.983	1,416	41	1,668	±11	15
13.1	grain	oscillatory	190	198	1.08	0.03	54.5	0.1098	0.81	5.03	3.4	0.3330	3.3	.968	1,855	53	1,791	±15	-4
14.1	grain	oscillatory	201	137	0.70	0.06	57.5	0.1099	0.78	5.01	3.3	0.3320	3.3	.972	1,847	52	1,790	±14	-3
15.1	grain	oscillatory	132	146	1.15	0.10	37.1	0.1101	0.97	4.92	3.5	0.3270	3.3	.959	1,823	53	1,786	±18	-2
16.1	grain	oscillatory	434	396	0.94	0.14	91.3	0.1092	0.62	3.64	3.3	0.2448	3.2	.971	1,412	41	1,764	±15	20
17	rim	unzoned	787	43	0	1	120	0.0931	1.2	2.16	3.6	0.1767	3.2	1	1,049	31	1,401	±32	25
18	grain	oscillatory	224	191	0.88	0.15	61.3	0.1090	0.74	4.71	3.4	0.3170	3.3	.962	1,777	51	1,761	±17	-1
Leucosome of Grt-Crd migmatite EC-727-18																			
1.1	grain	oscillatory	157	90	0.59	0.10	44.0	0.1113	0.86	4.96	1.9	0.3260	1.7	.872	1,819	26	1,807	± 17	-1
2.1	grain	oscillatory	180	109	0.63	2.25	45.0	0.1306	0.79	4.35	3.1	0.2841	2.1	.661	1,612	29	1,815	± 42	11
3.1	grain	metamict	4578	310	0.07	30.95	609	0.3870	0.48	1.72	19	0.1069	2.8	.153	655	18	1,904	±330	66
4.1	grain	metamict	1585	18	0.01	9.22	194	0.1617	0.49	1.49	6.5	0.1295	1.7	.258	785	12	1,279	±120	39
5.1	grain	oscillatory	3610	98	0.03	0.05	822	0.1025	0.21	3.73	1.6	0.2650	1.5	.989	1,516	21	1,661	± 4.2	9
5.2	grain	oscillatory	2267	21	0.01	0.03	527	0.1046	0.36	3.89	1.6	0.2707	1.6	.974	1,544	22	1,702	± 6.8	9
6.1	grain	metamict	2130	33	0.02	0.25	247	0.0852	0.40	1.54	1.6	0.1344	1.5	.933	813	12	1,271	± 12	36
7.1	grain	metamict	2776	131	0.05	0.19	649	0.1048	0.28	3.86	1.6	0.2717	1.6	.979	1,550	22	1,681	± 6.0	8
8	grain	oscillatory	2939	52	0.02	28.74	925	0.3823	0.16	4.70	26	0.2610	4.1	.156	1,496	55	2,090	±460	28
9.1	core	oscillatory	1320	95	0.07	39.54	162	0.4313	0.33	1.11	32	0.0864	3.7	.115	534	19	1,482	±610	64
10.1	grain	oscillatory	3274	65	0.02	0.51	366	0.0870	1.3	1.48	2.2	0.1296	1.5	.717	785	11	1,262	± 29	38
11.1	core	metamict	2588	57	0.02	0.23	314	0.0920	1.3	1.75	2.1	0.1409	1.6	.763	850	13	1,426	± 26	40
Grt-Bt migmatite B-394-1-99																			
1.1	grain	oscillatory	181	146	0.83	0.03	51.4	0.1117	0.76	5.09	1.8	0.3312	1.6	.902	1,844	26	1,823	± 14	-1
2.1	grain	oscillatory	129	66	0.53	0.01	36.6	0.1114	1.1	5.09	2.1	0.3312	1.7	.824	1,844	27	1,821	± 21	-1
3.1	grain	oscillatory	169	112	0.69	0.04	48.2	0.1125	0.82	5.13	1.9	0.3320	1.7	.893	1,848	27	1,835	± 15	-1
4.1	grain	sector	91	63	0.72	0.04	24.5	0.1130	1.1	4.88	2.3	0.3142	2.0	.854	1,761	31	1,842	± 22	4
5.1	rim	unzoned	3262	64	0.02	47.73	414	0.4455	0.25	0.61	71	0.0772	5.1	.072	480	24	520	±1500	7
5.2	core	oscillatory	304	157	0.53	4.12	79.0	0.1437	0.60	4.31	3.3	0.2898	1.6	.499	1,641	24	1,762	± 52	7
6.1	core	growth-banding	557	240	0.44	0.57	102	0.1086	0.60	3.03	1.9	0.2122	1.6	.846	1,240	18	1,691	± 18	27
7.1	core	oscillatory	300	169	0.58	0.02	80.4	0.1107	0.66	4.75	1.8	0.3117	1.6	.915	1,749	25	1,807	± 13	3
8.1	grain	oscillatory	282	123	0.45	0.12	79.7	0.1124	1.0	5.05	1.9	0.3293	1.6	.844	1,835	26	1,821	19	-1

TABLE 9

(continued)

Spot	Texture	Zoning	U (ppm)	Pb (ppm)	$^{232}Th/^{238}U$	$^{206}Pb_c$ (%)	$^{206}Pb^*$ (ppm)	Isotopic ratios $^{207}Pb^*/^{206}Pb^*$	±1s (%)	$^{207}Pb^*/^{235}U$	±1s (%)	$^{206}Pb^*/^{238}U$	±1s (%)	rho[a]	Ages (Ma) $^{206}Pb/^{238}U$ (Ma)	±1s	$^{207}Pb/^{206}Pb$ (Ma)	±1s	disc.[b]
Grt-Bt migmatite B-394-1-99																			
9.1	core	oscillatory	349	174	0.52	0.02	93.1	0.1098	0.77	4.69	1.8	0.3103	1.6	.902	1,742	25	1,794	± 14	3
10.1	rim	sector	1577	408	0.27	54.53	253	0.5520	2.3	1.03	67	0.0849	6.5	.097	525	33	1,380	±1300	62
11.1	rim	patchy	777	11	0.01	0.36	125	0.09757	0.54	2.43	1.7	0.1864	1.6	.894	1,102	16	1,518	± 15	27
12.1	grain	metamict	4675	463	0.10	2.73	352	0.08320	0.80	0.71	4.0	0.0852	1.7	.415	527	8.5	633	± 79	17
13.1	grain	sector	89	61	0.72	0.00	25.5	0.1121	1.1	5.17	2.1	0.3347	1.8	.834	1,861	29	1,833	± 21	-2
14.1	grain	sector	252	156	0.64	0.01	71.2	0.1125	0.69	5.09	1.8	0.3283	1.6	.919	1,830	26	1,839	± 13	0
15.1	core	oscillatory	222	164	0.77	0.09	55.1	0.1105	0.79	4.36	1.9	0.2885	1.7	.895	1,634	24	1,794	± 15	9
16.1	rim	unzoned	1546	269	0.18	27.81	181	0.3095	0.80	1.03	23	0.0983	2.5	.110	605	15	1,093	± 460	45
17.1	rim	unzoned	1817	33	0.02	8.52	145	0.1379	2.5	0.79	9.9	0.0853	1.7	.172	527	8.6	847	± 200	38
18.1	rim	sector	2159	54	0.03	30.12	292	0.3400	3.0	1.28	31	0.1101	2.9	.094	673	19	1,293	± 600	48
19.1	rim	unzoned	1715	403	0.24	8.40	133	0.1323	0.68	0.72	12	0.0829	1.8	.150	513	8.9	717	± 250	28
20.1	rim	patchy	958	17	0.02	3.88	86.9	0.0937	1.1	0.87	4.8	0.1015	1.6	.336	623	9.5	669	± 96	7
21.1	core	oscillatory	128	28	0.22	0.49	36.7	0.1173	1.1	5.19	2.8	0.3332	1.8	.639	1,854	29	1,848	± 39	0
Opx-Crd rock EC-722-18																			
1.1	grain	oscillatory	67	52	0.80	0.07	18.7	0.1124	1.6	5.04	3.5	0.3270	3.1	.880	1,823	49	1,828	±30	0
2.1	grain	oscillatory	149	112	0.78	0.07	41.5	0.1091	1.1	4.84	2.4	0.3236	2.1	.876	1,807	34	1,773	±21	-2
3.1	rim	unzoned	95	32	0.35	0.30	20.2	0.0992	1.8	3.28	3.1	0.2463	2.3	.750	1,420	29	1,559	±38	9
4.1	grain	growth-banding	76	54	0.73	0.18	20.8	0.1109	1.7	4.81	3.6	0.319	3.2	.866	1,785	49	1,788	±33	0
5.1	grain	oscillatory	166	180	1.12	0.06	44.9	0.1097	1.1	4.75	2.5	0.3151	2.2	.883	1,766	34	1,786	±21	1
6.1	rim	unzoned	109	19	0.18	0.26	24.4	0.0942	1.6	3.30	3.1	0.2599	2.3	.743	1,490	30	1,467	±39	-2
7.1	core	oscillatory	113	111	1.02	0.38	30.9	0.1090	1.4	4.64	3.0	0.3185	2.2	.748	1,783	35	1,726	±36	-3
8.1	grain	unzoned	110	18	0.17	0.07	25.8	0.0956	1.6	3.59	2.8	0.2740	2.2	.797	1,561	31	1,528	±32	-2
9.1	rim	unzoned	289	75	0.27	0.89	51.6	0.1009	1.4	2.64	3.3	0.2058	2.2	.652	1,206	24	1,492	±48	19
10.1	rim	unzoned	165	15	0.09	0.19	37.4	0.0943	1.3	3.36	2.6	0.2628	2.1	.836	1,504	29	1,481	±27	-2
10.2	core	growth-banding	133	101	0.79	0.39	33.8	0.1099	1.3	4.33	2.8	0.2952	2.2	.779	1,667	32	1,740	±32	4
11.1	inner rim	unzoned	92	49	0.55	0.00	24.6	0.1072	1.8	4.62	2.9	0.3128	2.3	.794	1,755	36	1,752	±33	0
11.2	core	growth-banding	85	79	0.96	0.26	23.6	0.1097	2.3	4.80	3.4	0.3237	2.3	.680	1,808	36	1,757	±45	-3
12.1	rim	sector	119	20	0.17	0.06	28.0	0.0962	1.5	3.61	2.7	0.2733	2.2	.818	1,558	31	1,541	±29	-1
13.1	rim	unzoned	192	14	0.07	0.30	43.6	0.0962	1.3	3.41	2.7	0.2644	2.1	.796	1,512	29	1,499	±31	-1
14.1	rim	unzoned	108	22	0.21	0.62	25.1	0.1025	1.6	3.59	3.4	0.2684	2.3	.669	1,533	31	1,569	±47	2
14.2	core	oscillatory	79	83	1.09	0.06	21.6	0.1094	1.5	4.79	2.8	0.3192	2.3	.822	1,786	26	1,780	±29	0
15.1	rim	unzoned	213	51	0.25	0.49	42.1	0.0986	1.3	2.98	2.9	0.2295	2.1	.736	1,332	35	1,514	±37	12
15.2	core	oscillatory	92	108	1.22	0.17	24.8	0.1113	1.4	4.76	2.7	0.3142	2.2	.821	1,761	36	1,796	±28	2
Grt-Bt-Sil migmatite EC-747-A-18																			
1.1	core	oscillatory	154	68	0.45	1.37	40.3	0.1173	0.87	4.36	2.7	0.3001	1.7	.646	1,692	26	1,722	±37	2
1.2	rim	unzoned	979	13	0.01	1.23	200	0.0938	2.7	2.70	4.6	0.2352	1.6	.343	1,362	20	1,278	±85	-7
2.1	core	oscillatory	159	114	0.75	0.74	42.1	0.11376	0.80	4.54	2.2	0.3071	1.7	.748	1,727	25	1,754	±27	2
2.2	rim	unzoned	1691	36	0.02	0.06	309	0.08654	0.37	2.53	1.6	0.2129	1.5	.958	1,244	17	1,339	± 8.9	7
3.1	core	oscillatory	41	20	0.51	1.51	10.1	0.1186	2.0	4.09	5.3	0.2814	2.0	.384	1,598	29	1,722	±90	7
4.1	rim	unzoned	1458	30	0.02	0.89	281	0.09378	0.33	2.64	1.8	0.2226	1.6	.898	1,295	19	1,343	±15	4
5.1	rim	sector	773	43	0.06	0.13	152	0.08666	0.48	2.70	1.7	0.2288	1.6	.942	1,328	19	1,327	±11	0
6.1	rim	unzoned	2072	35	0.02	0.01	418	0.08532	0.40	2.76	1.6	0.2350	1.6	.968	1,361	19	1,322	± 7.8	-3
7.1	grain	unzoned	1473	18	0.01	0.15	293	0.08669	0.33	2.72	1.6	0.2312	1.5	.967	1,341	19	1,324	± 7.9	-1
8.1	grain	unzoned	1936	37	0.02	0.07	391	0.08642	0.29	2.78	1.6	0.2352	1.6	.970	1,361	19	1,335	± 7.6	-2
9.1	grain	sector	286	3	0.01	0.05	53.3	0.08711	0.83	2.60	1.9	0.2171	1.7	.889	1,267	20	1,354	±17	6
10.1	rim	unzoned	1785	29	0.02	0.09	363	0.08630	0.31	2.79	1.6	0.2364	1.5	.974	1,368	19	1,327	± 6.9	-3
11.1	grain	sector	981	35	0.04	0.03	199	0.08647	0.43	2.81	1.6	0.2363	1.6	.963	1,367	19	1,344	± 8.4	-2
12.1	core	oscillatory	62	35	0.57	2.30	13.6	0.1245	1.4	3.57	4.5	0.2478	1.9	.422	1,427	24	1,706	±75	16
13.1	rim	unzoned	1685	31	0.02	--	319	0.08479	0.35	2.58	1.6	0.2202	1.5	.975	1,283	18	1,312	± 6.7	2
14.1	rim	sector	2556	41	0.02	0.01	503	0.08515	0.28	2.68	1.6	0.2289	1.5	.983	1,329	18	1,317	± 5.5	-1
15.1	core	oscillatory	180	72	0.41	0.15	45.4	0.10525	0.88	4.20	1.9	0.2932	1.6	.851	1,657	24	1,696	±19	2
16.1	rim	unzoned	1352	22	0.02	0.02	260	0.08570	0.38	2.64	1.7	0.2237	1.6	.972	1,301	19	1,327	± 7.6	2
17.1	core	oscillatory	269	157	0.60	0.60	66.4	0.10833	0.68	4.07	2.0	0.2862	1.6	.806	1,622	23	1,681	±22	3
18.1	core	sector	54	30	0.57	--	14.9	0.1099	1.5	5.03	2.8	0.3240	1.9	.685	1,809	31	1,841	±37	2
Leucosome of Grt-Bt-Sil migmatite EC-747-C-18																			
1.1	grain	oscillatory	387	13	0.03	0.16	77.8	0.0867	1.2	2.75	2.1	0.2337	1.6	.753	1,354	19	1,322	± 27	-2
2.1	grain	sector	579	19	0.03	0.02	117	0.08635	0.69	2.79	1.7	0.2346	1.6	.912	1,359	19	1,342	± 14	-1
3.1	grain	growth-banding	401	9	0.02	0.12	80.3	0.08648	0.68	2.74	1.8	0.2328	1.6	.895	1,349	19	1,327	± 15	-2
4.1	grain	growth-banding	479	8	0.02	--	94.8	0.08565	0.64	2.72	1.7	0.2303	1.6	.929	1,336	19	1,333	± 12	0
5.1	grain	growth-banding	553	4	0.01	0.03	110	0.08587	0.61	2.73	2.8	0.2312	2.7	.975	1,341	33	1,330	± 12	-1
6.1	grain	unzoned	351	11	0.03	0.21	67.9	0.08635	0.78	2.62	2.1	0.2246	1.6	.779	1,306	19	1,306	± 25	0
7.1	grain	oscillatory	350	18	0.05	0.28	68.9	0.08878	0.77	2.72	2.6	0.2285	2.4	.912	1,327	28	1,347	± 20	2
8.1	grain	oscillatory	351	12	0.03	0.29	68.2	0.08931	0.78	2.70	1.9	0.2254	1.7	.861	1,310	20	1,357	± 19	3
9.1	grain	oscillatory	366	4	0.01	1.79	66.2	0.10265	0.74	2.49	2.7	0.2066	1.6	.594	1,211	18	1,369	± 42	12
10.1	grain	growth-banding	317	4	0.01	0.04	60.5	0.08501	0.80	2.60	1.8	0.2224	1.6	.893	1,295	19	1,308	± 16	1
11.1	core	oscillatory	171	170	1.02	0.03	49.6	0.11341	0.79	5.26	1.9	0.3370	1.8	.911	1,872	29	1,851	± 14	-1

TABLE 9

(continued)

Spot	Texture	Zoning	U (ppm)	Pb (ppm)	$^{232}Th/^{238}U$	$^{206}Pb_c$ (%)	$^{206}Pb^*$ (ppm)	Isotopic ratios $^{207}Pb^*/^{206}Pb^*$	±1s (%)	$^{207}Pb^*/^{235}U$	±1s (%)	$^{206}Pb^*/^{238}U$	±1s (%)	rho[a]	Ages (Ma) $^{206}Pb/^{238}U$	±1s (Ma)	$^{207}Pb/^{206}Pb$	±1s (Ma)	disc.[b]
Grt-B Leucosome of Grt-Bt-Sil migmatite EC-747-C-18																			
9.1	core	oscillatory	349	174	0.52	0.02	93.1	0.1098	0.77	4.69	1.8	0.3103	1.6	.902	1,742	25	1,794	± 14	3
12.1	core	oscillatory	199	65	0.34	0.27	48.4	0.1048	1.3	4.00	2.3	0.2828	1.6	.724	1,605	23	1,670	± 29	4
12.2	rim	unzoned	597	18	0.03	0.14	121	0.0881	1.2	2.83	2.0	0.2362	1.6	.785	1,367	19	1,357	± 24	-1
13.1	rim	unzoned	366	4	0.01	0.01	71.6	0.08575	0.75	2.69	1.8	0.2279	1.6	.892	1,323	19	1,330	± 16	1
13.2	core	unzoned	432	5	0.01	0.08	85.8	0.08674	0.77	2.74	1.8	0.2310	1.6	.891	1,340	19	1,340	± 16	0
14.1	grain	oscillatory	677	7	0.01	0.03	134	0.08548	0.55	2.69	1.7	0.2293	1.6	.942	1,331	19	1,320	± 11	-1
15.1	core	oscillatory	254	189	0.77	0.10	59.6	0.09654	0.68	3.59	1.8	0.2724	1.7	.916	1,553	23	1,541	± 14	-1
16.1	core	oscillatory	67	47	0.73	5.58	17.2	0.1535	1.2	4.09	6.6	0.2825	2.0	.303	1,604	28	1,715	±110	6
17.1	core	oscillatory	60	33	0.56	0.13	14.9	0.1053	1.6	4.15	2.6	0.2887	1.9	.746	1,635	28	1,701	± 32	4
18.1	grain	oscillatory	194	146	0.78	0.08	50.5	0.10829	0.86	4.48	2.0	0.3022	1.7	.851	1,702	25	1,758	± 19	3
19.1	core	oscillatory	321	136	0.44	1.01	56.5	0.1102	1.7	2.84	3.3	0.2029	1.6	.497	1,191	18	1,651	± 53	28

$^{206}Pb_c$ represents the percentage of ^{206}Pb in common lead in the total ^{206}Pb.
* represents radiogenic. Common Pb corrected using measured ^{204}Pb.
[a] Error correlation, defined as $err^{206}Pb/^{238}U/err^{207}Pb/^{235}U$.
[b] Degree of concordance {=($^{206}Pb/^{238}U$ age*100)/($^{207}Pb/^{206}Pb$ age)}.

Leucosome of Grt-Crd migmatite EC-727-18.—Zircon is very rare in the metapelitic leucosome sample and 12 spots on 11 grains were analyzed. Two different populations of zircon occur. The first generation forms oscillatory-zoned long-prismatic grains and the cores of zoned grains with high luminescence (fig. 7G). The Th/U ratios are high (0.59–0.63, ignoring analyses of strongly metamict grains with high amount of common Pb (table 9). The zoned zircon yields Paleoproterozoic (*ca.* 1800 Ma) $^{207}Pb/^{206}Pb$ ages (again, ignoring analyses with high amounts of common Pb (table 9) and one near-concordant analysis defines a $^{207}Pb/^{206}Pb$ age of 1807 ± 17 Ma (figs. 7G and 8G; table 8). The second generation of zircon is CL dark and forms narrow unzoned to weakly zoned rims around the zoned grains (fig. 7G) or, more often, anhedral to subhedral, short- to long-prismatic grains (figs. 7H and 7I). The largely metamict rims and individual grains have very low Th/U ratios (0.01–0.07; fig. 9C) and locally preserve relics of an oscillatory zoning (fig. 7H). They yield strongly discordant data that define a Discordia with an upper intercept at 1722 ± 7.5 Ma and a lower intercept at 513 ± 13 Ma, respectively (fig. 8H).

Grt-Bt migmatite B-394-1-99.—Twenty-two spots on 21 zircon grains were analyzed. The data define a major age cluster at *ca.* 1800 Ma and a second one at *ca.* 500 Ma (fig. 8I). Most high to moderate luminescent grains are subhedral to euhedral with a long- to short-prismatic shape and oscillatory or sector zoning (figs. 7J and 7K). The predominantly near-concordant zoned grains have high Th/U ratios (0.22–0.83, fig. 9D) and yield a Discordia with an upper intercept at 1827 ± 12 Ma and a poorly defined lower intercept at 466 ± 130 Ma (fig. 8J). Seven analyses define a Concordia age of 1836 ± 7 Ma, close to the upper intercept age (fig. 8K).

Oscillatory-zoned zircon may also form resorbed cores that are surrounded by a narrow highly luminescent corona followed by usually narrow unzoned or patchy-zoned and weakly-luminescent rims (figs. 7K and 7L) with low Th/U ratios (0.01–0.27; fig. 9D). The rims locally resorb the cores (fig. 7L) and may contain high amounts of common Pb (table 9, analyses were deleted from fig. 8I). The data of the rims define a Discordia with a poorly defined upper intercept at 1706 ± 330 Ma and a lower intercept at 495 ± 130 Ma (fig. 8L). Two analyses define a Pan-African Concordia age of 521 ± 22 Ma.

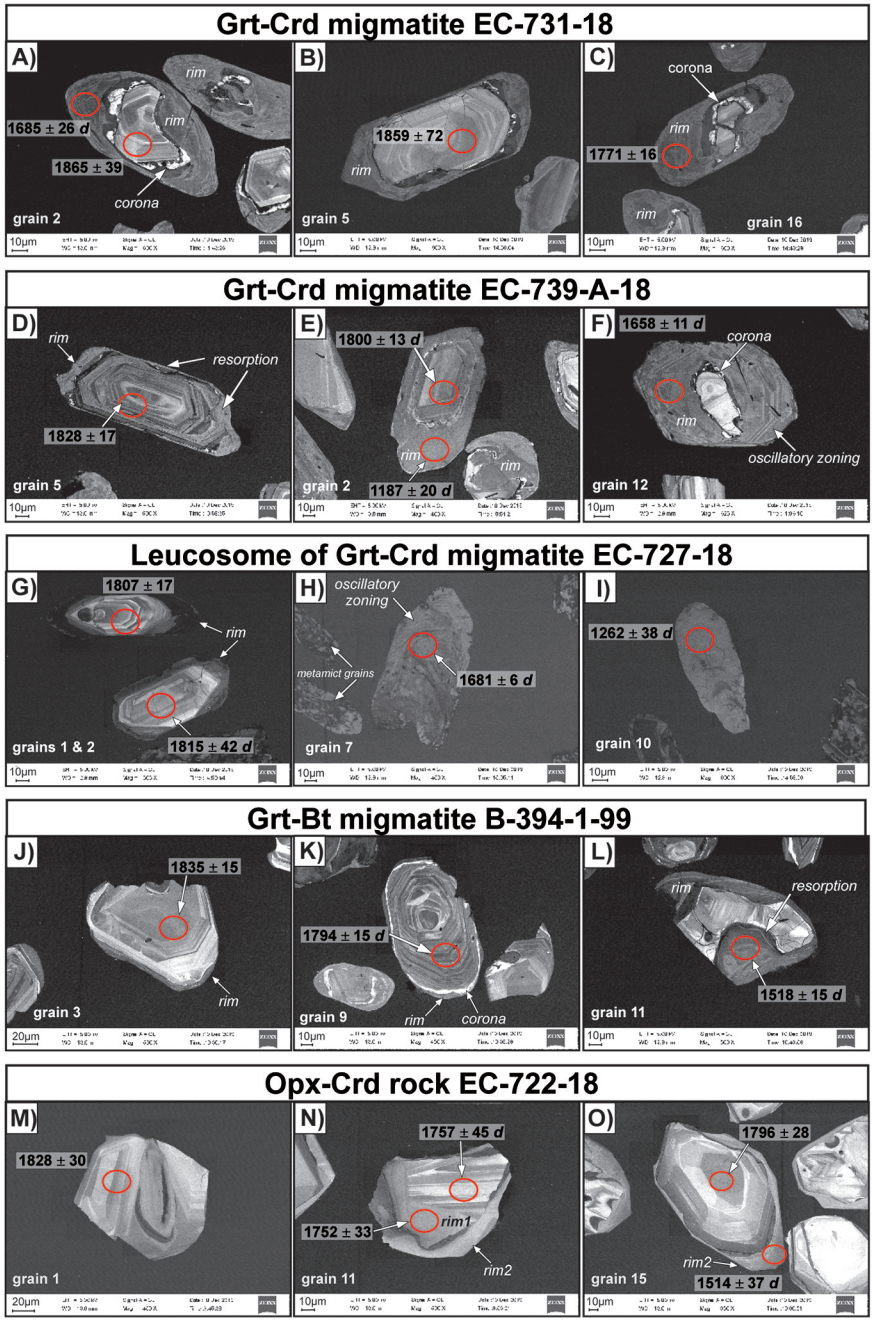

Fig. 7. Representative cathodoluminescence (CL) images of zircons extracted from the samples of the Epupa Complex. White circles mark the position of the analysis spot (scaled to size). Ages are presented as $^{207}Pb/^{206}Pb$ ages (in Ma) with 2_ sigma error. Discordant analyses (discordance > 2%) are marked with *d*. (A) Anhedral zircon with oscillatory-zoned core and broad rim. The zoning of the core is truncated and overgrown in an embayment by the rim that shows relics of sector zoning. A thin highly luminescent corona separates the core from the rim. (B) Subhedral zircon with large oscillatory-zoned core and narrow

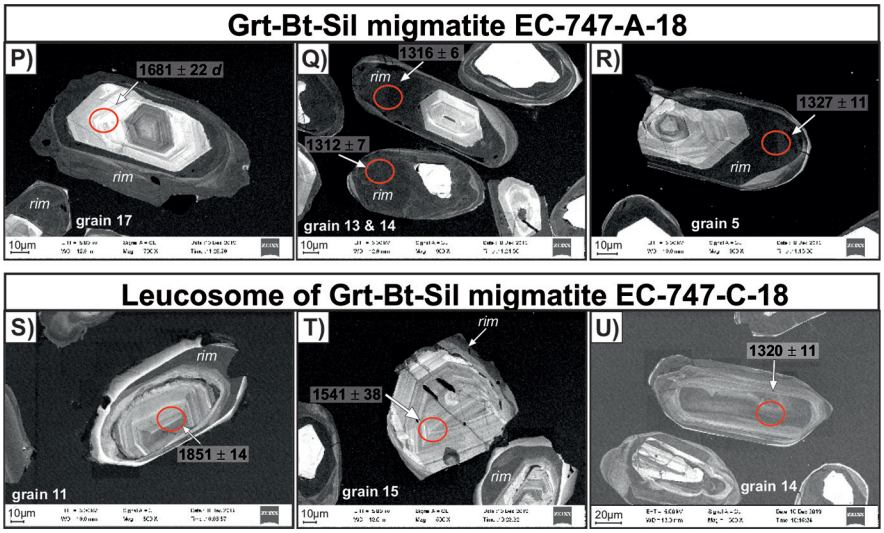

Fig. 7. continued unzoned rim. (C) Anhedral zircon with fractured and growth-banded core that is surrounded by a rim that preserves relics of sector zoning. A highly luminescent corona separates core and rim. (D) Subhedral oscillatory-zoned zircon. The grain is surrounded by a narrow rim of structureless zircon that also grows in an embayment into the resorbed core. (E) Subhedral zircon with oscillatory-zoned core and broad unzoned rim. (F) Subhedral short-prismatic zircon with small resorbed core and broad rim that shows relics of oscillatory zoning. A highly luminescent corona locally occurs between core and rim. (G) Euhedral oscillatory-zoned zircons with narrow unzoned rims. (H) Subhedral metamict zircon with relics of oscillatory zoning. (I) Subhedral metamict zircon. (J) Subhedral oscillatory-zoned zircon with narrow rim. (K) Subhedral oscillatory-zoned zircon surrounded by a narrow high-luminescent corona and a weakly luminescent rim. (L) Anhedral zircon with oscillatory-zoned core. The zoning of the core is truncated and overgrown in an embayment by patchy-zoned zircon. (M) Anhedral oscillatory-zoned zircon. (N) Anhedral zircon with growth-banded core and two generations of unzoned rims. An inner rim (rim1) is surrounded by a younger outer rim (rim2). (O) Subhedral zircon with euhedral oscillatory-zoned core and unzoned rim. (P) Subhedral zircon with anhedral to euhedral cores and broad unzoned rims. (Q) Subhedral zircon with euhedral oscillatory-zoned core and unzoned rim. (R) Anhedral zircon with oscillatory-zoned core and broad unzoned rim. (S) Subhedral zircon with resorbed oscillatory-zoned core and broad unzoned rim. (T) Subhedral oscillatory-zoned zircon with narrow unzoned rim. (U) Subhedral oscillatory-zoned zircon.

Opx-Crd rock EC-722-18.—A total of 19 spot analyses were made on 15 zircon grains. The data define two age cluster, at *ca.* 1800 Ma and at *ca.* 1500 Ma (fig. 7M). Bright, oscillatory-zoned or growth-banded grains with high Th/U ratios (0.73–1.22; fig. 9E) that may preserve their euhedral long- to short-prismatic shape (aspect ratios up to 1:4; fig. 7M-O) define the Paleoproterozoic cluster with $^{207}Pb/^{206}Pb$ ranging between 1828 and 1780 Ma (ignoring > 1% discordant grains). Concordant analyses define a Concordia age of 1784 ± 9 Ma (fig. 8N). One grain yielded an older concordant $^{207}Pb/^{206}Pb$ age of 1828 ± 14 Ma (figs. 7M and 8M). Unstructured or sector-zoned and weakly luminescent rims of variable size may surround the zoned grains and may resorb the core domains (figs. 7N and 7O). In addition, unzoned zircon may form individual subhedral grains. One broad rim with a Th/U ratio of 0.55, which is surrounded by a younger rim (fig. 7N), yielded a concordant Paleoproterozoic $^{207}Pb/^{206}Pb$ age of 1752 ± 33 Ma age. The other bright luminescence rims and individual grains have low Th/U ratios (0.07–0.35; fig. 9E) and record younger Mesoproterozoic ages (fig. 7M). Three concordant analyses define an age of 1533 ± 26 Ma (fig. 7O).

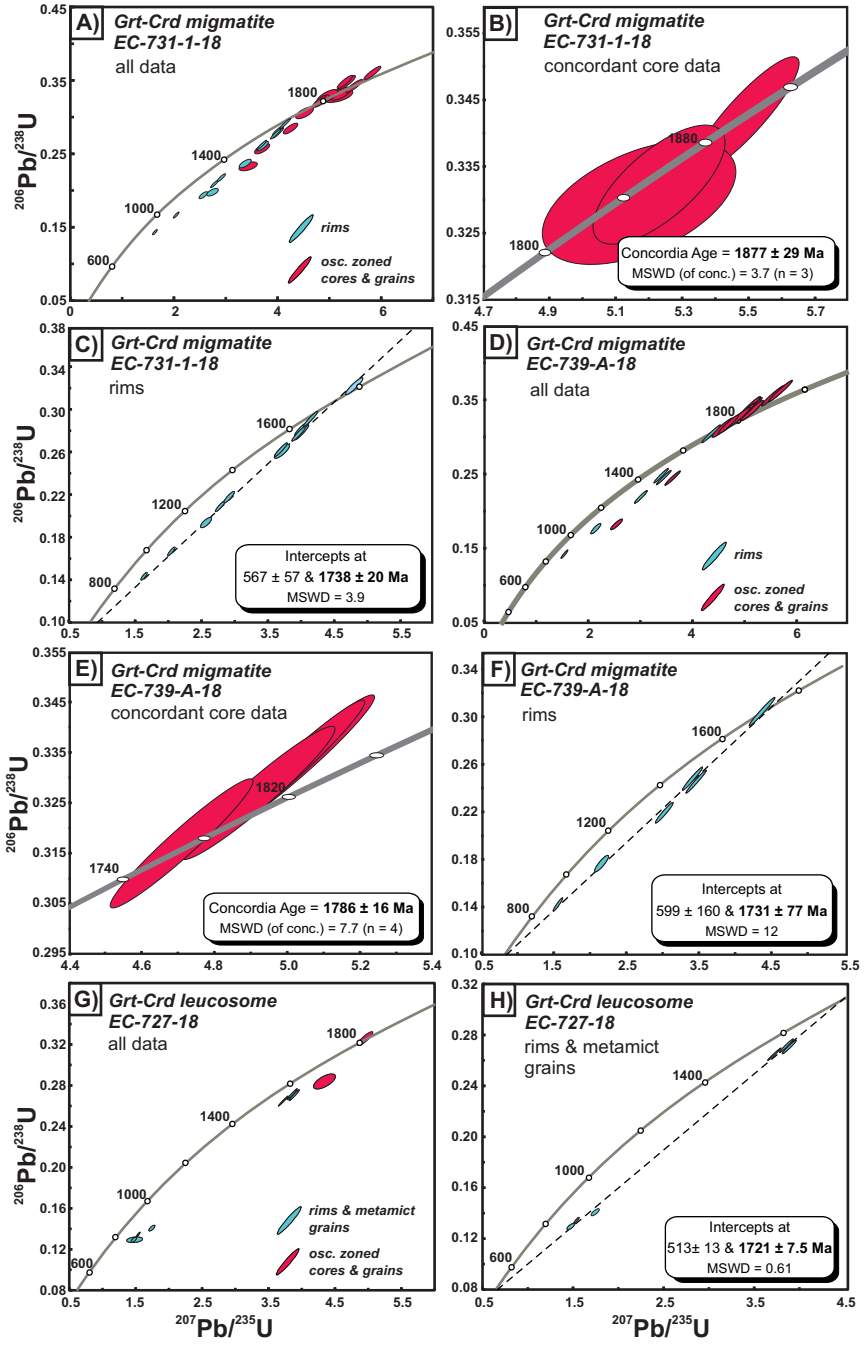

Fig. 8. U-Pb concordia diagrams for the pelitic migmatites and Opx-Crd rocks of the Epupa Complex. Concordia ages are given with 2σ standard uncertainties. Data-point error ellipses are 2σ.

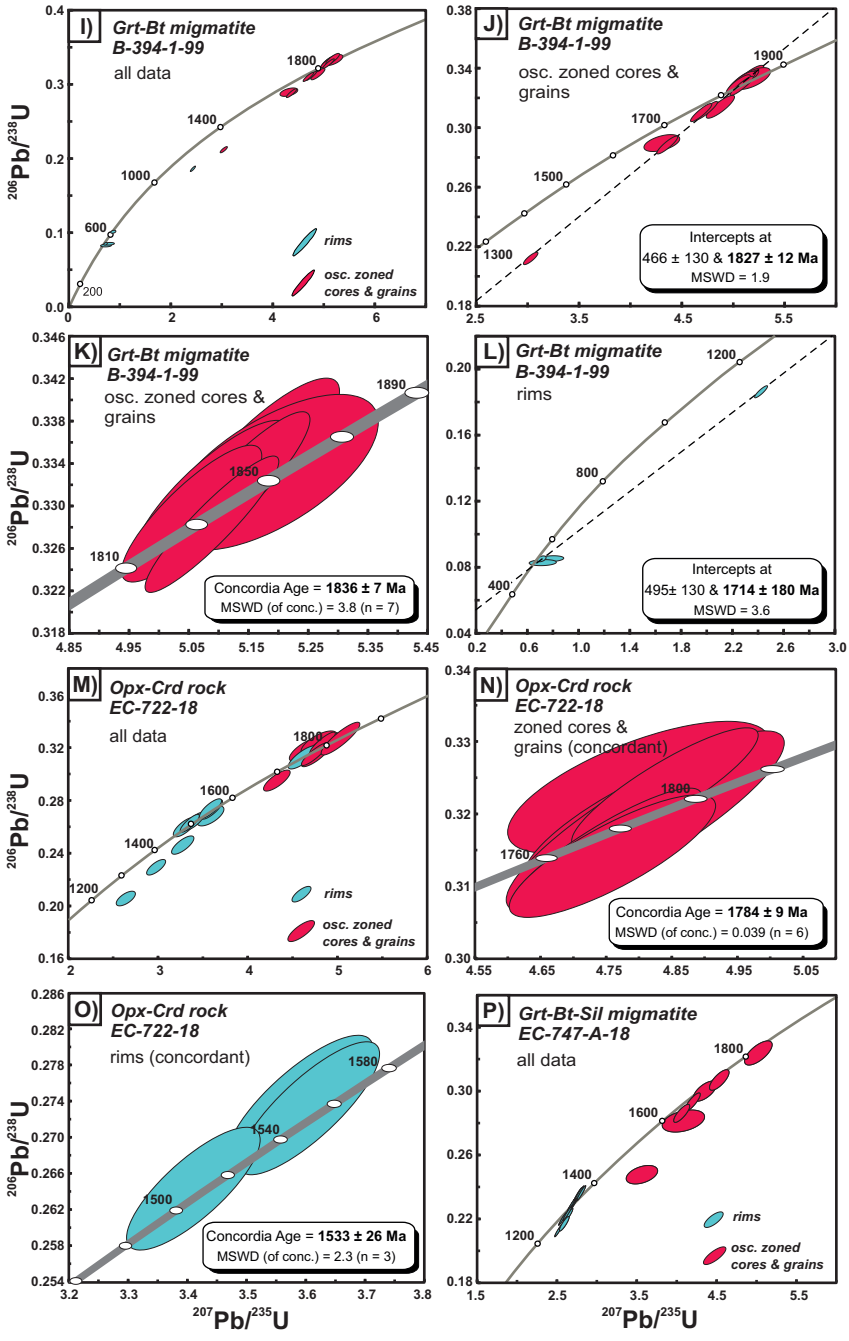

Fig. 8. Continued

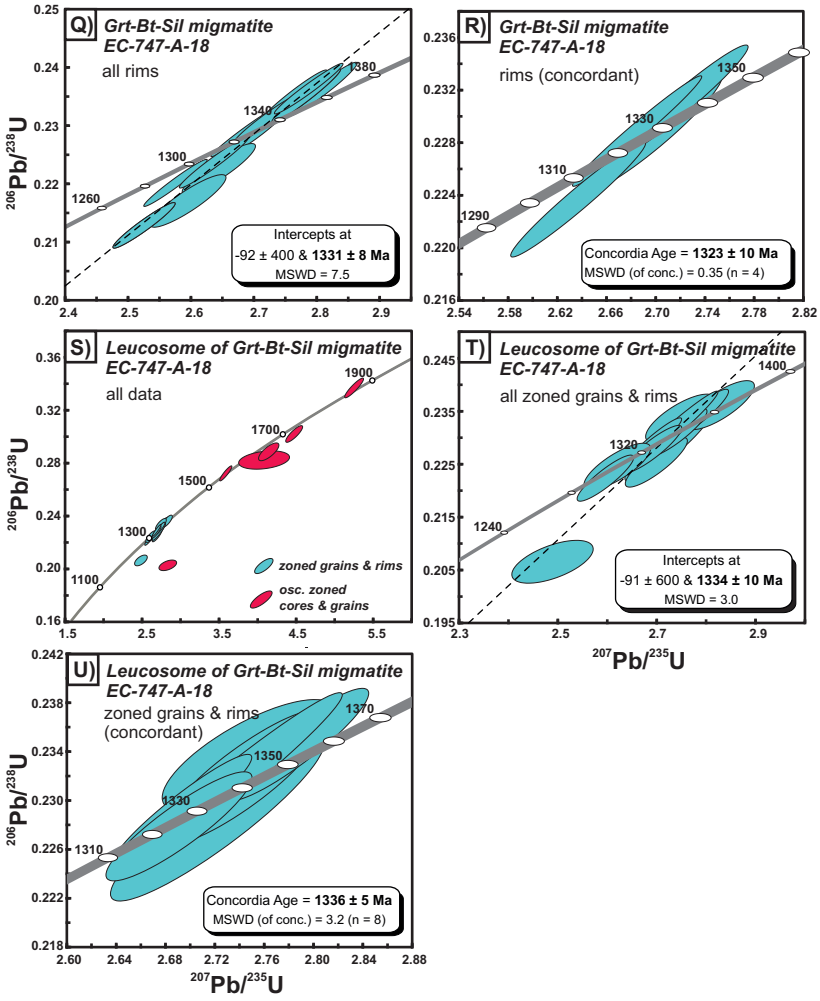

Fig. 8. Continued

Orue Unit

Grt-Bt-Sil migmatite EC-747-A-18.—Twenty spots on 18 grains were analyzed. All zircons of the sample show core-rim relationships (figs. 7P–7R). The cores that show oscillatory zoning or growth-banding, high Th/U ratios (0.41–0.75), and high or moderate luminescence reveal discordant $^{207}Pb/^{206}Pb$ ages between 1841 and 1696 Ma (ignoring > 2% discordant data, fig. 8P; table 9). They are surrounded by broad, very weakly luminescent and unzoned rims of zircon (figs. 7P–7R) that usually form conformable to the cores. Unzoned or sector zoned zircon also forms euhedral long- to short-prismatic grains without relic cores. The unzoned rims and grains have very low Th/U ratios (0.01–0.06) and define a Discordia with an upper intercept at 1331 ± 8 Ma and a meaningless lower intercept (fig. 8Q). Four concordant analyses yielded a slightly lower Concordia age of 1323 ± 10 Ma (fig. 8R).

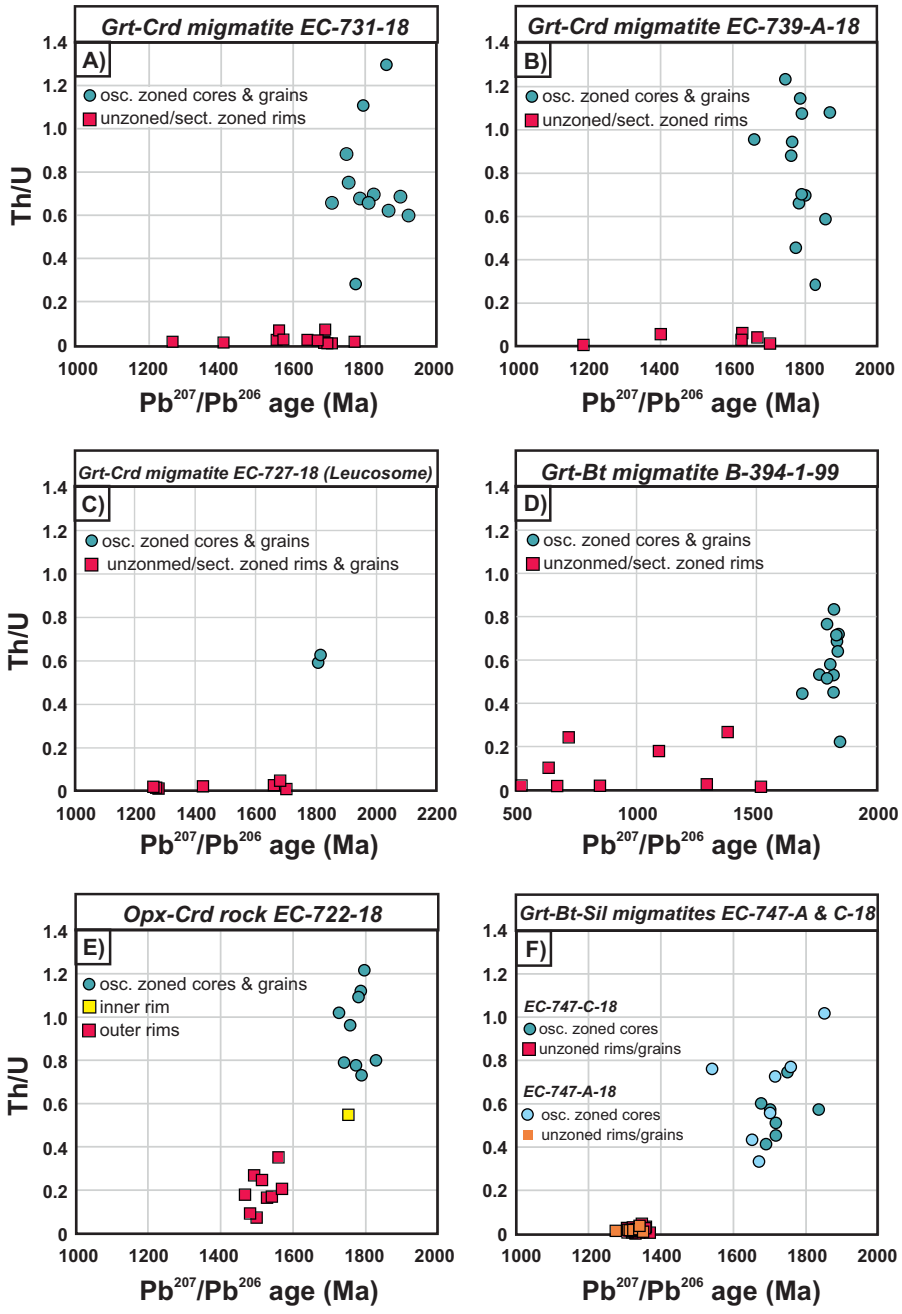

Fig. 9. Plots of Th/U versus Pb-Pb ages of spot analyses from zircon of the pelitic migmatites and Opx-Crd rocks of the Epupa Complex.

Leucosome of Grt-Bt-Sil migmatite EC-747-C-18.—Twenty-one spot analyses were made on 19 zircon grains. Like zircon of the associated migmatite sample, CL revealed core-rim relationships for several grains of the leucosome (fig. 7S). Highly to moderately luminescent cores with high Th/U ratios (0.34–1.02; fig. 9F) commonly show oscillatory-zoning and $^{207}Pb/^{206}Pb$ ages between 1851 to 1758 Ma (ignoring > 3% discordant data, figs. 7S and 8S; table 9). One oscillatory-zoned grain (Th/U ratio: 0.77) is exceptional with a near-concordant $^{207}Pb/^{206}Pb$ age of 1541 ± 14 Ma (fig. 7T). Most zircons of the leucosome are weakly luminescent, subhedral to euhedral and show oscillatory zoning or growth banding (fig. 7U). Such weakly luminescent zircon also forms coronas around the highly luminescent zoned cores (figs. 7S and 7T). The weakly luminescent rims and individual grains have very low Th/U ratios (0.01–0.05; fig. 9F), and yield a Discordia with a 1334 ± 10 Ma upper-intercept age and a meaningless lower intercept. Eight concordant analyses revealed a well-defined Concordia age of 1336 ± 5 Ma, consistent with the upper intercept age.

DISCUSSION

Interpretation of Zircon Structures and Composition

Zircon of the paragneiss samples from the Eyao Unit and the Orue Unit show clear core-rim relationships. The long to short-prismatic morphology, the common oscillatory zoning and the high Th/U ratios (0.28–1.30; fig. 9) suggest a magmatic formation for the cores (for example, Kirkland and others, 2015; Taylor and others, 2016), which are interpreted as detrital grains. Narrow highly-luminescent zircon coronas around detrital zircon cores, as described for the Eyao samples, were described in several studies and interpreted to result from fluid-driven solution-reprecipitation processes (for example, Geisler and others, 2007; Gerdes and Zeh, 2009; Taylor and others, 2016; Kunz and others, 2018), consistent with the observed local resorption of the detrital cores.

The following weakly-luminescent rims are usually interpreted to result from metamorphic new growth at amphibolite facies conditions (for example, Kunz and others, 2018) but may also result from alteration of early zircon (Gerdes and Zeh, 2009). The Th/U ratios of altered zircons overlap with the ratios of the original zircon (Gerdes and Zeh, 2009). Hence, the very low Th/U ratios of the rims (usually 0.01–0.07; figs. 9A–9D) in the Eyao Unit zircon document their metamorphic formation. Furthermore, the weak luminescence (U-rich) and uniform appearance in CL with lack of zoning or rare sector zoning are typical for anatectic zircon growth in the presence of a melt (for example, Vavra and others, 1996; Schaltegger and others, 1999; Rubatto and Gebauer, 2000; Corfu and others, 2003). Rarely preserved oscillatory zoning in subhedral to euhedral individual grains of the leucosome sample EC-727-18 and the migmatite sample EC-739-A-18, and the often observed resorption of the detrital cores support the interpretation of the formation of weak luminescent zircon in the anatectic melt (for example, Taylor and others, 2016; Kunz and others, 2018). Core-rim relationships that are dominated by the detrital cores with usually narrow metamorphic rims as observed for the Eyao samples are characteristic for mid-amphibolite facies conditions (Kunz and others, 2018), consistent with the peak *P-T* conditions constrained for the Eyao Unit.

In the Opx-Crd rock, two generations of highly-luminescent rims occur. Rare unstructured inner rims are surrounded by younger rims that may display sector zoning. The low Th/U ratios of the inner (0.55) and the outer rims (0.07–0.35; fig. 9E), and the zoning suggest metamorphic formation of both zircon rim generations in the Opx-Crd rock. The observed unzoned homogeneous grains with low Th/U ratios are

typical of metamorphic zircon that formed under granulite facies conditions (for example, Kunz and others, 2018).

The core-rim relationship also occurs in zircon of the Orue Unit samples: Detrital cores are surrounded by unzoned, dark luminescent rims. The very low Th/U ratios (0.01–0.06; fig. 9F), the dark CL-emission (U-rich), the subhedral to euhedral long-prismatic shape and the lack of zoning, or oscillatory zoning to growth banding, indicate the metamorphic formation of the weakly luminescent grains and rims in an anatectic melt (for example, Taylor and others, 2016; Kunz and others, 2018). However, in contrast to the Eyao Unit samples the core-rim proportion is dominated by the rims in the Orue Unit zircons; cores are usually very small or absent. Newly-grown grains without detrital grains are restricted to the Orue Unit and the granulite facies Opx-Crd rock. Structures and zoning patterns, as observed for the Orue Unit, are characteristic for zircon formation under upper-amphibolite facies conditions (for example, Kunz and others, 2018), and are in good agreement with *P-T* constraints for the Orue Unit samples. The higher degree of partial melting in the Orue Unit samples and the Opx-Crd rock caused the more intensive resorption of the detrital grains, ultimately resulting in the formation of thicker rims around relic detrital grains and of newly-grown zircon (for example, Rubatto and others 2001; Kelsey and others, 2008; Yakymchuk and Brown, 2014), consistent with the high amount of newly-grown metamorphic zircon in the leucosome sample of the Orue Unit.

Timing of Deposition of the Metasediments

Concordant $^{207}Pb/^{206}Pb$ zircon core ages (< 1% discordance) of the metasedimentary samples of the Eyao Unit scatter between 1898 ± 20 Ma and 1774 ± 16 Ma. Judging from the internal textures (oscillatory zoning or growth-banding), the commonly long-prismatic shape and the usually high Th/U ratios, we postulate a magmatic formation of these zircon cores. Kröner and others (2015) reported slightly older concordant Palaeoproterozoic $^{207}Pb/^{206}Pb$ ages between 2075 and 1820 Ma for detrital zircons from a migmatitic paragneiss sample of the Eyao Unit. Emplacement ages of granitoids exposed along the Kunene River in the Eyao Unit range between 1835 to 1775 Ma (*in situ* U/Pb zircon ages, Kröner and others, 2015). Hence, the age range of the detrital magmatic zircon in our studied metasediments overlaps with the emplacement of the granitoids that are therefore the most likely source rocks for the detrital zircons. Based on the zircon data we postulate that the Eyao Unit metasediments were deposited after 1774 Ma and incorporated detrital zircon from reworked granitoids, which were part of the Paleoproterozoic magmatic belt at the south-western Congo Craton margin. This model also explains the lack of Archean detrital zircon in the metasediments.

Kröner and others (2015) reported that the contacts between the paragneiss sequence and metagranitoids in the Eyao Unit are covered by sand. However, based on the age data for the detrital zircons these authors proposed broadly synchronous sedimentation and granite emplacement. We also did not find contacts between the metagranitoids and the metasediments, however our more extensive data set for the metasediments indicates that deposition was initiated later than 1774 Ma (youngest detrital magmatic grain), almost immediately after granite emplacement.

(Near)-concordant zircon cores in the pelitic migmatites of the western part of the Orue Unit (EC-747-A-18, EC-747-A-18) yielded a similar age range with Paleoproterozoic $^{207}Pb/^{206}Pb$ ages mainly scattering between 1851 ± 14 and 1696 ± 19 Ma. One grain yielded an exceptional young magmatic zircon core (near concordant $^{207}Pb/^{206}Pb$ age 1541 ± 14 Ma). The upper age limit of the Orue Unit data broadly overlaps with the Eyao zircon core data, but the lower limit is slightly younger, even when ignoring the Mesoproterozoic zircon. The zoning patterns, the low Th/U ratios

and the prismatic shape are consistent with magmatic growth of the zircon cores in the Orue samples. The age range of detrital magmatic zircon cores is broadly consistent with data of detrital zircon in other paragneisses of the Orue Unit (1997 ± 12 to 1731 ± 17 Ma, Seth and others, 2005) and of the UHT granulite facies Epembe Unit (1810 ± 11 to 1660 ± 14 Ma, Seth and others, 2003) and indicate a long-lasting deposition of sediments in the southern part of the Epupa Complex up until 1660 Ma or even 1540 Ma, considering the early-Mesoproterozoic zircon core.

Kröner and others (2010) reported U-Pb zircon emplacement ages of 1861 ± 3 to 1758 ± 3 Ma for granitoids from the southern part of the Epupa Complex. The emplacement ages fall into the age span of detrital magmatic zircon in the paragneisses (Epembe Unit and Orue Unit) of the southern part of the Epupa Complex (2000–1660 Ma; Seth and others, 2003, 2005, this study). The data suggest formation of the sediments through re-working of Paleoproterozoic granitoids like the formation of the metasediments of the Eyao Unit. The exceptional Mesoproterozoic zircon core may originate from re-worked Mesoproterozoic granitoids (1530–1520 Ma) that were recognized in the Epupa Complex (Kröner and others, 2015).

Timing of Metamorphic Events in the Epupa Complex

The studied pelitic migmatites record three phases of high-grade metamorphism and partial melting in the Epupa Complex, lasting from the late-Paleoproterozoic to mid-Mesoproterozoic (fig. 10).

Late Paleoproterozoic metamorphism.—The pelitic Grt-Crd migmatites of the Eyao Unit investigated here record the earliest high-grade metamorphic overprint and concomitant partial melting event in the Epupa Complex. This event is dated at 1740 to 1720 Ma by upper intercept ages defined by metamorphic rims around the Paleoproterozoic detrital zircon cores in migmatite samples EC-731-18 and EC-739-A-18, and individual anatectic zircon in the leucosome sample EC-727-18 (ignoring the poorly-defined upper-intercept data of B-394-1-99). These age data suggest that mid-amphibolite facies metamorphism and partial melting followed almost immediately on the deposition of the sediments, which is bracketed between 1774 Ma (youngest concordant detrital magmatic zircon core) and 1740 Ma (onset of metamorphism). The concordant Paleoproterozoic $^{207}Pb/^{206}Pb$ age of 1752 ± 33 Ma, obtained from a metamorphic rim around a detrital grain, suggests that the Opx-Crd rock was affected by the same event, but was later overprinted by younger Mesoproterozoic granulite facies metamorphism (see below).

The late Paleoproterozoic (1740–1720 Ma) timing of high-grade metamorphism and partial melting in the Eyao Unit is consistent with deformation and partial melting of the slightly older granitoids of this unit (emplaced between 1835–1775 Ma) and broadly agrees with the sparely documented *ca.* 1760 Ma high-temperature event as reported by Kröner and others (2010) for the south-westernmost part of the Epupa Complex. This event was constrained by a melt patch in a migmatitic gneiss and the anatectic Otjitanda Granite, both of which are exposed west of Etengwa (fig. 1A), yielding U-Pb zircon ages of 1762 ± 4 Ma and 1757 ± 4 Ma, respectively (Kröner and others, 2010). Linking the data of the north-western (Eyao Unit) and the south-western part of the Epupa Complex reveals a new regional-scale high-temperature metamorphic event that affected the western part of the complex. In the eastern part of the complex, south of the Kunene Anorthosite Complex, evidence for evidence for this event is absent.

Kröner and others (2015) reported a pre-1835 Ma migmatization event in the Eyao Unit that is constrained from field observations indicating the intrusion of a foliated granodiorite, emplaced at 1835 Ma, into migmatitic granite gneisses thereby cutting the compositional layering of the migmatite. We found deformed xenoliths of

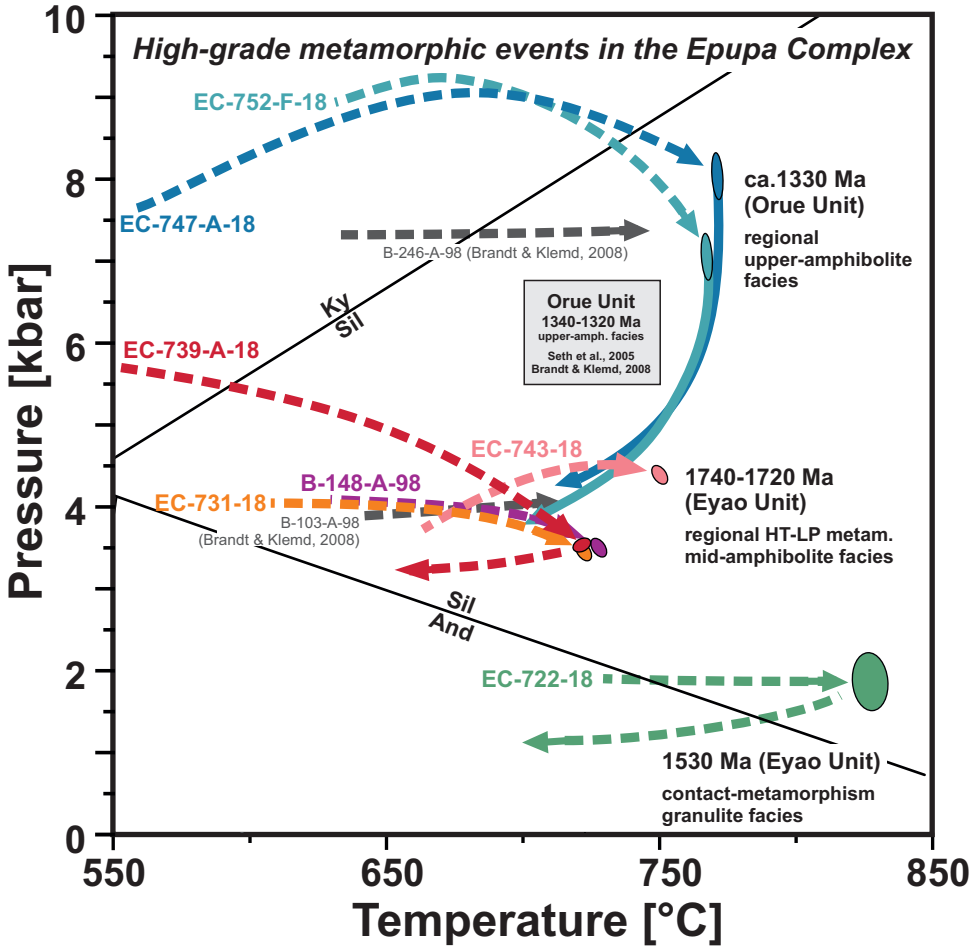

Fig. 10. Comparison of the *P-T* paths constrained in the present study with *P-T* paths and *P-T* conditions of the Orue Unit rocks presented in a previous study (Brandt and Klemd, 2008) and correlation of the *P-T* data with the new age data.

amphibolites and felsic gneisses in the Paleoproterozoic Eyao Unit metagranitoids, but did not study them in detail, since we focused on the metamorphic evolution of the metasediments, which were deposited < 1774 Ma and therefore do not record direct evidence for an older metamorphic event. However, some of the detrital zircon cores in the metasediments revealed concordant ages > 1835 Ma (for example the 1877 ± 29 Ma $^{207}Pb/^{206}Pb$ age of the concordant zircon in sample EC-731-A-18), older than the oldest granitoids, and thus may be related to this event. This interpretation is supported by sector zoning, typical of metamorphic zircon, of the oldest concordant grain (1898 ± 20 Ma $^{207}Pb/^{206}Pb$ age).

Early-Mesoproterozoic metamorphism.—Broad zircon overgrowths around Paleoproterozoic zircon cores of the Opx-Crd rock EC-722-18 record a second high-grade metamorphic event. The age of 1533 ± 26 Ma (fig. 7O), as defined by three concordant analyses, is interpreted as the timing of early-Mesoproterozoic granulite facies metamorphism. As evidence for this event only occurs in the Opx-Crd sample, it is interpreted as a local

metamorphic event that is apparently restricted to the western-most part of the Eyao Unit.

The occurrence of the Opx-Crd rocks in the vicinity of a large gabbro complex (fig. 1A) suggests a contact metamorphic formation of the Opx-Crd assemblages related to the gabbro emplacement. However, the lack of zircon in the prepared gabbro sample prevented our attempt to date the emplacement of the gabbro, and thus the timing of gabbro emplacement remains uncertain. Nevertheless, the 1530 Ma granulite facies event is coeval with the emplacement of the 'red granites' (1530–1520 Ma) exposed along the Kunene River (Kröner and others, 2015). Similar red granites also occur in the vicinity of the Opx-Crd rock sample EC-722-18 (fig. 1C) and the largest granite body is probably also host of a red granite sample (NA173) with an emplacement age of *ca.* 1520 Ma (Kröner and others, 2015). Consistently, paragneiss xenoliths in the granite (fig. 2A) document its emplacement subsequent to Paleoproterozoic metamorphism, recognizing the granites, apart from the gabbro, as additional heat source of HT-LP contact metamorphism. Early-Mesoproterozoic granulite facies metamorphism in the Eyao Unit is also coeval with UHT metamorphism in the Epembe Unit exposed south of the Kunene Intrusive Complex that was dated between 1530 to 1450 Ma (Seth and others, 2003). However, as the UHT rocks are 80 km distant from the Eyao Unit a direct cogenetic formation seems unlikely.

Mid-Mesoproterozoic metamorphism.—The two samples from the Orue Unit record the third high-grade metamorphic event, with associated melting, that culminated at upper-amphibolite facies conditions. Broad metamorphic zircon rims around detrital Paleoproterozoic cores in both samples and newly-grown metamorphic zircon in the leucosome sample revealed consistent mid-Mesoproterozoic upper-intercept and Concordia ages of *ca.* 1330 Ma. A sample from a near-by locality yielded almost the same Concordia age of 1336.6 + 6.1 Ma (sample 246-A, Seth and others, 2005). Our new age data matches the time-span of upper-amphibolite facies peak metamorphism in the Orue Unit, which was bracketed between 1340 and 1320 Ma (Seth and others, 2005). The absence of earlier metamorphic zircon growth suggests that the southern part of the Epupa Complex was not affected by the Paleoproterozoic high-temperature metamorphic event, which was recognized in the Eyao Unit and the south-western part of the Epupa Complex.

Pan African overprint.—All migmatite samples from the Eyao Unit show a strong re-setting of the U-Pb system and the discordant data yield crudely defined lower-intercept ages between 599 ± 160 and 466 ± 130 Ma. Re-setting affected both the detrital cores and, more intensively, the metamorphic rims. In sample B-394-1-99, the overprint caused rare new growth of *ca.* 520 Ma zircon. Although the overlying rocks of the Damara Group lack evidence for a Pan-African tectono-metamorphic overprint the age data indicate that the re-setting and limited growth of zircon is related to the Pan African orogeny that caused the formation of the Kaoko Belt of northern Namibia. The Kaoko Belt formed from the collision of the Congo Craton with the São Francisco Craton of Brazil between 780 and 520 Ma during the Gondwana assembly and runs parallel to the coast of the Atlantic Ocean (fig. 1B) with inland-decreasing metamorphic grade (for example, Goscombe and others, 2003). Therefore, re-equilibration is attributed to strong fluid activity during the hydrothermal overprint that caused the widespread alteration of the rocks. Pan African re-setting is absent in our two Orue Unit samples, but has been previously reported for a leucosome sample of the Orue Unit (Seth and others, 2005).

P-T-t Evolution of High-Grade Metamorphic Events in the Epupa Complex

The three high-grade metamorphic events that were recognized by zircon SHRIMP age data record distinct *P-T* paths that were reconstructed by linking the thermobarometric data with constraints from *P–T* pseudosection modeling (fig. 10).

Eyao Unit.—The Grt-Crd and Grt-Bt migmatites of the Eyao Unit that record regional late-Paleoproterozoic (1740–1720 Ma) high-grade metamorphism and partial melting are characterized by heating-cooling *P-T* paths, which culminate at high-temperature-low-pressure (HT-LP) peak conditions of *ca.* 720 °C and 4 kbar (fig. 10). Pseudosection modeling and thermobarometric calculations yield consistent mid-amphibolite facies *P-T* conditions of 720 to 750°C at 3.5 to 4.5 kbar and 700 to 730 °C at 3.5 to 5 kbar (table 6), respectively, for the formation of the peak assemblages. The slightly lower temperatures calculated from thermometry probably reflect re-equilibration of biotite. The HT-LP event is characterized by the formation of the peak-metamorphic assemblage Grt-Crd-Bt-Sil-Ilm-Kfs-Pl-Qz-melt in Fe-rich and Al-rich samples (EC-731-18, EC-739-A-18) and Grt-Crd-Bt-Ilm-Kfs-Pl-Qz-melt in more magnesian and less aluminous metapelites (EC-743-18). The garnet-free Crd-Bt-Ilm-Kfs-Pl-Qz-melt peak assemblage was formed at the same peak conditions in aluminous and magnesian metapelites (B-148-A-98). Constraints from melt-reintegrated pseudosections suggest that the prograde evolution of the metapelites is characterized by significant heating with minor decompression in the sillimanite-stability field, causing the complete to partial replacement of early white mica, sillimanite, and biotite by cordierite, garnet, and K-feldspar through melt-producing reactions. Due to the lack of suitable reaction textures, the retrograged evolution of the migmatites is poorly recorded, but near-isobaric cooling seems very likely due to the low peak-pressures, implying heating-cooling paths without significant pressure variations. Such near-isobaric *P-T* paths are a characteristic of HT-LP metamorphism (De Yoreo and others, 1991).

The peak-metamorphic conditions are close to the only previous *P-T* estimate of 750 °C at 4.5 kbar for the rocks of the Eyao Unit that had been constrained for a Grt-Crd-Bt migmatite sample (B-103-A-98) through geothermobarometry and pseudosection modeling (Brandt and Klemd, 2008, fig. 10). The minor difference is probably related to the calculation at that time, which was performed in the simple NCKFMASH system without adjustment of the very high H content (related to alteration) and the O content. Since at that time no age information was available for the sample, high-grade metamorphism had been attributed to Mesoproterozoic metamorphism of the Orue Unit, due to the similar peak-metamorphic conditions and similar structural relationships (Brandt and Klemd, 2008).

Opx-Crd rocks from the westernmost Eyao Unit recorded distinct peak *P-T* conditions that culminate at higher granulite facies temperatures and substantially lower pressures of 830 °C and 2 kbar (fig. 10) than in the main part of the Eyao Unit. The peak *P-T* conditions correspond to a very high geothermal gradient of 140 °C/km. The *P-T* path is characterized by heating and post-peak near-isobaric cooling.

Orue Unit.—The two studied pelitic Grt-Bt-Sil migmatites from the western part of the Orue Unit document that 1330 Ma regional upper-amphibolite facies metamorphism and anatexis is characterized by a clockwise *P-T* path. Constraints from melt-reintegrated pseudosections indicate that the prograde evolution of the metapelites is characterized by significant heating at mid- to lower-crustal levels of *ca.* 8 kbar, as displayed by the Ca-rich core composition of prograde zoned garnet and inclusions of kyanite, rutile, and white mica. Heating led to the transformation of kyanite to sillimanite, the replacement of white mica by K-feldspar-sillimanite, and the replacement of rutile by ilmenite as the stable Ti-phase of the matrix. Partial replacement of sillimanite and biotite during melt-producing reactions caused the formation of the peak

assemblage Grt-Bt-Sil-Ilm-Kfs-Pl-Qz-melt at upper-amphibolite facies conditions of *ca.* 770 °C at 7.5 kbar, as estimated by integrating thermobarometric data (760–840°C, 8 kbar) and the slightly lower *P-T* estimates derived from the pseudosections (760–770°C, 7–8 kbar). The retrograde evolution is characterized by the growth of cordierite and plagioclase coronas around garnet that document post-peak near-isothermal decompression to at least 5 kbar at still high temperatures.

The peak-metamorphic conditions are higher than those reported for the main part of the Orue Unit, but are similar to the peak *P-T* data (740 °C, 7.5 kbar) of a previously studied Grt-Bt-Sil migmatite sample (B-246-A-98; fig. 10), *ca.* 600 m away from the two newly studied outcrops (Brandt and Klemd, 2008). A simple heating-cooling path was constrained for this sample (fig. 10). However, the cordierite and plagioclase coronas resorbing garnet, which are absent in sample B-246-A-18, document significant post-peak decompression and, thus, imply a clockwise evolution of the 1330 Ma upper-amphibolite facies metamorphic event in the western part of the Orue Unit. Samples from the main, eastern part of the Orue Unit record simple heating-cooling paths (Brandt and Klemd, 2008).

Geodynamic Model

The studied high-grade metamorphic rocks of the Epupa Complex record a protracted evolution from the Paleoproterozoic to the early Cambrian that shed some light on the poorly-known geodynamic evolution of the south-western margin of the Congo Craton of central Africa.

Detrital magmatic zircon cores indicate the derivation of the studied metasediments of the Epupa Complex from re-worked granitoids of a Paleoproterozoic magmatic arc with granitoid emplacement ages between 1860 and 1760 Ma (Kröner and others, 2010, 2015) that formed along the active continental margin of the south-western Congo Craton (fig. 1B). The deposition of the metasediments in a back-arc basin between the arc and the craton margin seems very likely, as was also suggested by constraints from the bulk rock composition of the Epupa Complex metasediments (Brandt, ms, 2003). Shortly after the deposition, bracketed between 1774 Ma (youngest detrital core) to 1740 Ma (onset of HT-LP metamorphism), and subsequent subsidence into mid-crustal levels, the metasediments of the Eyao Unit in the northern-most part of the Epupa Complex were affected by regional near-isobaric HT-LP metamorphism and migmatization at shallow crustal levels (*ca.* 12 km depth) that is dated at 1740 to 1720 Ma. This event, which is restricted to the Eyao Unit, is characterized by an elevated geotherm (60 °C/km). Such conditions necessitate the presence of a large component of advective heat transfer and/or anomalously high basal heat flow during metamorphism (for example, De Yoreo and others, 1991). Heat supply from asthenospheric convection cells or from magmas intruding into a crust of normal thickness may produce elevated geotherms and periods of an isobaric thermal evolution (Hyndman and others, 2005), as constrained for the Eyao migmatites. The granitoids of the magmatic arc would represent an adequate heat source for HT-LP metamorphism in the Eyao Unit, but since they were reworked into the sediment, this can be excluded. Therefore, HT-LP metamorphism is attributed to heating of the Eyao Unit metasediments in a back-arc basin through magmatic accretion of uprising basic melt resulting from partial melting of the subducting slab. This model can also explain the moderate pressure decrease during heating (fig. 10).

The further geodynamic evolution of the Epupa Complex is characterized by its transition from a convergent plate margin that was involved in the Eburnean Orogeny to an intracratonic setting. We link the two determined Mesoproterozoic high-grade metamorphic events (1530 Ma and 1330 Ma) to widespread magmatic activity and extensional tectonics in southern Africa that are associated with the early-stage

separation of the Congo and the southern Kaapvaal-Zimbabwe Cratons. Local 1530 Ma HT-LP contact metamorphism recorded by the Opx-Crd rocks of the Eyao Unit slightly predates the emplacement of the older generation of anorthosites of the Kunene Intrusive Complex (KIC) that were recently dated at *ca.* 1500 Ma (Bybee and others, 2019). The formation of the massif-type KIC is related to asthenospheric up welling during crustal extension in an extensional belt that formed during the separation of the Congo and the Kaapvaal-Zimbabwe Cratons (Drüppel and others, 2001, 2007). Accretion of basic melt that acted as the source for the anorthosites was interpreted to cause regional UHT metamorphism in the Epembe Unit (Brandt and others, 2007) south of the KIC and the new 1500 Ma emplacement age for the older anorthosites supports this cogenetic model. However, the large distance between the Eyao Unit and the Epembe Unit and the different peak conditions (*ca.* 1000 °C, 9.5 kbar) and different counter-clockwise *P-T* paths of the UHT granulites (Brandt and others, 2003, 2007) preclude a direct link to 1530 Ma granulite facies contact metamorphism at shallow crustal levels (830 °C at 2 kbar) in the Eyao Unit. Nevertheless, massif-type anorthosites are usually associated with granite formation (Drüppel and others, 2007) and the formation of the 1530 to 1520 Ma granites in the Eyao Unit, which probably acted as heat source for contact metamorphism, was presumably related to regional crustal heating induced by the basic melts of the KIC.

The third high-grade metamorphic event at *ca.* 1330 Ma is related to the emplacement of the second generation of anorthosites between 1385 to 1319 Ma. Mid-Mesoproterozoic upper-amphibolite facies metamorphism with near-isobaric heating-cooling paths was previously reported for the main part of the Orue Unit and interpreted to result from mid-crustal regional-scale contact metamorphism induced by the emplacement of the anorthosites (Brandt and Klemd, 2008). The two samples from the western part of the Orue Unit record similar upper-amphibolite facies peak conditions, but are exceptional as they document significant decompression and uplift from lower crustal levels. The clockwise *P-T* paths are interpreted to reflect extensional collapse of the magmatically thickened crust that was heated to upper-amphibolite facies conditions by the basic melts.

In the early Cambrian (*ca.* 520 Ma) the rocks of the Eyao Unit were affected by an intense hydrothermal overprint, suggesting that the westernmost part of the Epupa Complex was involved in the Pan African orogeny.

ACKNOWLEDGMENTS

We thank Anna Nguno of the Ministry of Mines and Energy in Windhoek, Namibia, for the logistic support of our field campaign. We also thank Ewereth Muvangua and Jason Indongo of the Ministry of Mines and Energy in Windhoek, Namibia, for their company and support during fieldwork in the Epupa Complex. This paper is dedicated to Alfred Kröner. Constructive comments of Richard Palin and an anonymous reviewer considerably improved the paper.

APPENDIX

Analytical Methods

Electron Probe Micro-Analysis (EPMA).—Mineral chemical data (tables 2–5) were obtained at the GeoZentrum Nordbayern (GZN), Erlangen University using a JEOL JXA-8200 microprobe. The instrument is equipped with five wavelength-dispersive spectrometers (WDS). For all measured elements in various minerals an acceleration voltage of

15 kV, a probe current of 15 nA and a probe diameter of 3 μm were used. Both natural and synthetic mineral standards were used for calibration. Matrix corrections were conducted using a ZAF procedure. Estimation of ferric iron in spinel is based on charge balance, assuming ideal stoichiometry.

X-Ray Fluorescence (XRF) Spectroscopy.—Analyses of the bulk-rock major elements as well as selected trace elements (Ba, Co, Cr, Cu, Ga, Nb, Ni, Pb, Rb, Sr, Th, U, V, Y, Zn, Zr) were conducted by X-ray fluorescence spectrometry (XRF) on fused glass discs using a Spectro Xepos energy dispersive X-ray spectrometer (Spectro Analytical Instruments GmbH) at the GZN in Erlangen. Loss on ignition (LOI) was determined prior to major element analysis using a pre-ignition method after heating the samples (1 g) for 12 h at 1300 °C. Precision and accuracy were generally better than 1% (2σ) for the major elements and 0–5% for most trace elements.

SHRIMP II Zircon Dating.—Heavy mineral concentrates obtained from crushing and magnetic separation were further purified by panning, and zircons were then handpicked and mounted in epoxy resin together with chips of the zircon standards TEMORA (Black and others, 2004) and M257 (Nasdala and others, 2008) in the Beijing SHRIMP Centre, Chinese Academy of Geological Sciences. The mounts were ground down and polished so that the zircon interiors were exposed, and zircons were photographed under cathodoluminescence (CL) to enable easy and best location on the mount during SHRIMP analysis. CL imaging was performed on a Hitachi S-3000N scanning electron microscope (accelerating voltage 9 kV, beam current 109 mA, pixel time 200; for high-resolution images of figure 7, pixel time of 400 was used).

Zircon isotopic analyses were performed on the SHRIMP II sensitive high-resolution ion-microprobe of the Beijing SHRIMP Center, and the analytical procedures are detailed in Williams (1998). The intensity of the primary O_2 ion beam was ~3 nA, and a Köhler aperture of 100 μm diameter was used, giving a slightly elliptical spot size of about 30 μm. Each analytical site was rastered for 2.5 min prior to analysis to remove surface common Pb. Five scans through the mass stations were made for each age determination. Reference zircons M257 (U = 840 ppm, Nasdala and others, 2008) and TEMORA 2 ($^{206}Pb/^{238}U$ age = 416.8 Ma, Black and others, 2004) were used for U-elemental abundance and calibration of $^{206}Pb/^{238}U$, respectively. Peak resolution at 1% peak height was between 4600 and 5200, enabling clear separation of the Pb peaks from interference peaks. Sensitivity was about 20 cps/ppm/nA Pb on the standard. Analyses of samples and standards were alternated to allow assessment of Pb+/U+ discrimination. The 1-sigma error of the $^{206}Pb/^{238}U$ ratio during analysis of all standard zircons during this study was between 0.8 and 1.1%. Common-Pb corrections were applied using the ^{204}Pb-correction method, and because of very low counts on ^{204}Pb in most samples it was assumed that common lead is surface-related (Kinny, 1986). Therefore, the isotopic composition of Broken Hill lead was used for correction. Data processing was carried out using the SQUID and ISOPLOT programs (Ludwig, 2001, 2003). Uncertainties in the isotopic ratios of individual analyses in table 9 are given at 1σ, whereas uncertainties for ages on the concordia diagrams are quoted at 2σ.

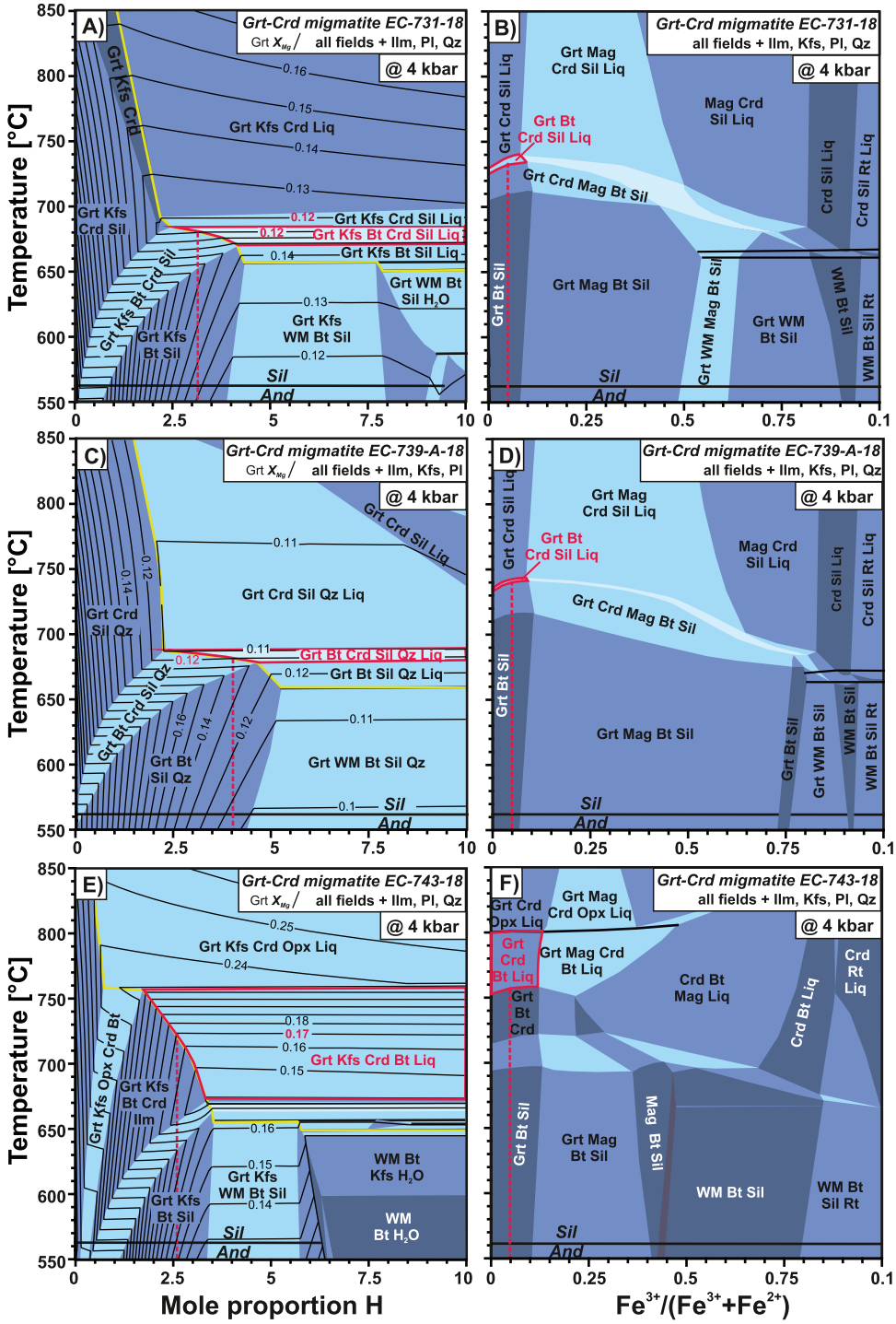

Fig. A1. *T-H* sections and *T-*M_{Fe2O3} sections at 4 kbar (Eyao Unit: fig. A1.A–H), 2 kbar (Opx-Crd rock of the Eyao Unit: figs. A1.I and J) or 8 kbar (Orue Unit: fig. A1.K–N). The *P–T* fields of the peak-assemblages are outlined by a bold red line. The estimated H values used in the *T-*M_{Fe2O3} and the *P-T* sections are indicated by a bold and dashed red line. The bold yellow line marks the solidus in the *T-H* sections. In the *T-*M_{Fe2O3} sections the estimated Fe_2O_3/Fe_{tot} ratios used with equivalent O values in the *P-T* sections are indicated by a bold and dashed red line.

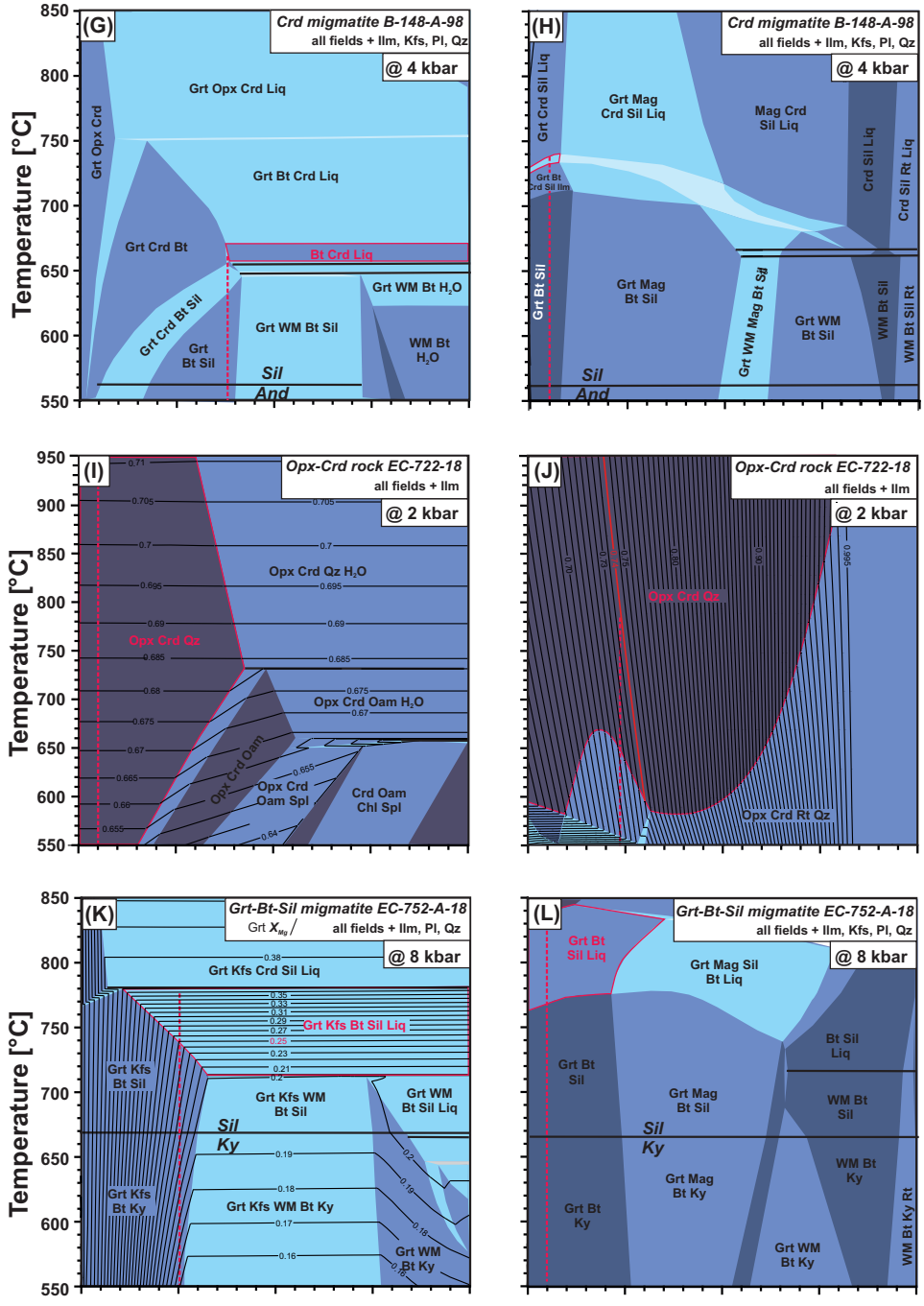

Fig. A1. Continued

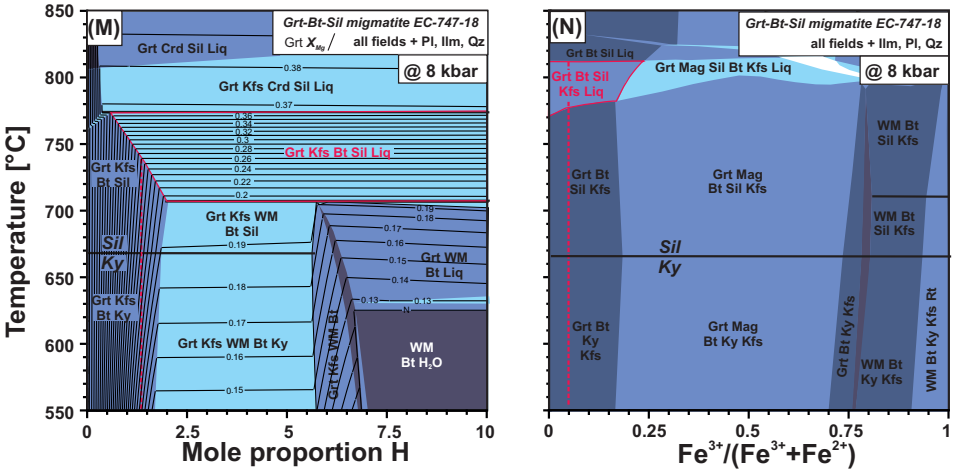

Fig. A1. Continued

TABLE A1

Bulk rock XRF data of metasediments of the Epupa Complex

Rock Unit	Eyao Unit							Orue Unit	
Rock type	Opx-Crd rock		Grt-Crd migmatite			Crd migmatite	Grt-Bt migmatite	Grt-Bt-Sil migmatite	
Sample	EC-722-18	B-284-C-98	EC-731-18	EC-739-A-18	EC-743-18	B-148-A-98	EC-744-18-D	EC-747-18-A	EC-752-18-F
wt.%									
SiO_2	45.74	48.42	65.09	56.01	65.15	61.93	69.10	75.82	66.98
TiO_2	1.61	0.80	0.67	1.00	0.67	0.85	0.35	0.25	0.47
Al_2O_3	22.46	14.46	16.81	21.70	15.98	17.68	15.50	12.72	17.74
Fe_2O_3	9.50	12.53	6.33	8.90	4.60	5.39	3.44	2.58	4.47
MgO	13.31	12.90	1.69	1.73	1.61	1.55	1.17	0.96	1.70
CaO	0.84	0.72	0.77	1.09	1.99	1.15	1.79	0.43	1.21
Na_2O	0.70	1.22	1.85	1.71	3.51	2.72	4.58	2.83	2.21
K_2O	1.60	3.33	3.66	5.26	3.16	5.92	3.00	2.99	3.40
LOI [(1)]	3.34	4.96	2.58	1.78	2.85	1.26	0.66	1.05	1.41
MnO	0.11	0.12	0.22	0.35	0.06	0.06	0.10	0.04	0.08
P_2O_5	0.61	0.25	0.09	0.12	0.18	0.05	0.10	0.07	0.10
total	99.84	99.72	99.76	99.66	99.76	98.56	99.79	99.76	99.78
X_{Mg}	0.74	0.67	0.35	0.28	0.41	0.36	0.40	0.42	0.43

REFERENCES

Ashwal, L. D., and Twist, D., 1994, The Kunene complex: Geological Magazine, v. 131, n. 5, p. 579–591, https://doi.org/10.1017/S0016756800012371

Bartoli, O., 2017, Phase equilibria modelling of residual migmatites and granulites: An evaluation of the melt-reintegration approach: Journal of Metamorphic Geology, v. 35, n. 8, p. 919–942, https://doi.org/10.1111/jmg.12261

Bhattacharya, A., Mohanty, L., Maji, A., Sen, S. K., and Raith, M., 1992, Non-ideal mixing in the phlogopite-annite binary: Constraints from experimental data on Mg−Fe partitioning and a reformulation of the biotite-garnet geothermometer: Contributions to Mineralogy and Petrology, v. 111, p. 87–93, https://doi.org/10.1007/BF00296580

Bial, J., Büttner, S. H., Schenk, V., and Appel, P., 2015, The long-term high-temperature history of the central Namaqua Metamorphic Complex: Evidence for a Mesoproterozoic continental back-arc in southern Africa: Precambrian Research, v. 268, p. 243–278, https://doi.org/10.1016/j.precamres.2015.07.012

Black, L. P., Kamo, S. L., Allen, C. M., Davis, D. W., Aleinikoff, J. N., Valley, J. W., Mundil, R., Campbell, I. H., Korsch, R. J., Williams, I. S., and Foudoulis, C., 2004, Improved $^{206}Pb/^{238}U$ microprobe geochronology by the monitoring of a trace-element-related matrix effect; SHRIMP, ID–TIMS, ELA–ICP–MS and oxygen isotope documentation for a series of zircon standards: Chemical Geology, v. 205, n. 1–2, p. 115–140, https://doi.org/10.1016/j.chemgeo.2004.01.003

Brandt, S, ms, 2003, "Metamorphic evolution of ultrahigh-temperature granulite and upper amphibolite facies rocks of the Proterozoic Epupa Complex", NW Namibia: Würzburg, Germany, University of Würzburg, Germany, Ph. D. thesis, 289 p.

Brandt, S., and Klemd, R., 2008, Upper–amphibolite facies partial melting of paragneisses from the Epupa Complex, NW Namibia, and relations to Mesoproterozoic anorthosite magmatism: Journal of Metamorphic Geology, v. 26, n. 9, p. 871–893, https://doi.org/10.1111/j.1525-1314.2008.00793.x

Brandt, S., Klemd, R., and Okrusch, M., 2003, Ultrahigh-temperature metamorphism and multistage evolution of garnet–orthopyroxene granulites from the Proterozoic Epupa Complex, NW Namibia: Journal of Petrology, v. 44, n. 6, p. 1121–1144, https://doi.org/10.1093/petrology/44.6.1121

Brandt, S., Will, T. M., and Klemd, R., 2007, Magmatic loading in the proterozoic Epupa Complex, NW Namibia, as evidenced by ultrahigh-temperature sapphirine-bearing orthopyroxene–sillimanite–quartz granulites: Precambrian Research, v. 153, n. 3–4, p. 143–178, https://doi.org/10.1016/j.precamres.2006.11.016

Brandt, S., Schenk, V., Raith, M. M., Appel, P., Gerdes, A., and Srikantappa, C., 2011, Late Neoproterozoic clockwise *P-T* evolution of HP-UHT granulites from the Palni Hills (South India): New constraints from phase diagram modelling and LA-ICP-MS zircon dating combined with *in-situ* EMP monazite dating: Journal of Petrology, v. 52, n. 9, p. 1813–1856, https://doi.org/10.1093/petrology/egr032

Bybee, G. M., Hayes, B., Owen-Smith, T. M., Lehmann, J., Ashwal, L. D., Brower, A. M., Hill, C. M., Corfu, F., and Manga, M., 2019, Proterozoic massif-type anorthosites as the archetypes of long-lived (≥100 Myr) magmatic systems—New evidence from the Kunene Anorthosite Complex (Angola): Precambrian Research, v. 332, p. 105393, https://doi.org/10.1016/j.precamres.2019.105393

Cahen, L., Snelling, N. J., Delhal, J., and Vail, J. R., 1984, The geochronology and evolution of Africa: Oxford, United Kingdom, Clarendon Press, 512 p.

Clark, C., Fitzsimons, I. C. W., Healy, D., and Harley, S. L., 2011, How does the continental crust get really hot?: Elements, v. 7, n. 4, p. 235–240, https://doi.org/10.2113/gselements.7.4.235

Corfu, F., Hanchar, J. M., Hoskin, P. W. O., and Kinny, P., 2003, Atlas of Zircon Textures: Reviews in Mineralogy and Geochemistry, v. 53, p. 469–500, https://doi.org/10.2113/0530469

de Capitani, C., and Brown, T. H., 1987, The computation of chemical equilibrium in complex systems containing non-ideal solutions: Geochimica et Cosmochimica Acta, v. 51, n. 10, p. 2639–2652, https://doi.org/10.1016/0016-7037(87)90145-1

De Carvalho, H., Tassinari, C., Alves, P. H., Guimarães, F., and Simões, M. C., 2000, Geochronological review of the Precambrian in western Angola: Links with Brazil: Journal of African Earth Sciences, v. 31, n. 2, p. 383–402, https://doi.org/10.1016/S0899-5362(00)00095-6

De Yoreo, J. J., Lux, D. R., and Guidotti, C. V., 1991, Thermal modelling in low-pressure/high-temperature metamorphic belts: Tectonophysics, v. 188, n. 3–4, p. 209–238, https://doi.org/10.1016/0040-1951(91)90457-4

Drüppel, K., von Seckendorff, V., and Okrusch, M., 2001, Subsolidus reaction textures in the anorthositic rocks of the southern part of the Kunene Intrusive Complex, NW Namibia: European Journal of Mineralogy, v. 13, n. 2, p. 289–309, https://doi.org/10.1127/935-1221/01/0013-0289

Drüppel, K., Littmann, S., Romer, R. L., and Okrusch, M., 2007, Petrology and isotope geochemistry of the Mesoproterozoic anorthosite and related rocks of the Kunene Intrusive Complex, NW Namibia: Precambrian Research, v. 156, n. 1–2, p. 1–31, https://doi.org/10.1016/j.precamres.2007.02.005

Druppel, K., Elsasser, L., Brandt, S., and Gerdes, A., 2013, Ultrahigh-temperature metamorphism in Rogaland, Norway: New evidence from in-situ LA-ICPMS geochronology and pseudosection modelling of sapphirine-bearing and associated granulites: Journal of Petrology, v. 54, p. 305–350, https://doi.org/10.1093/petrology/egs070

Frost, B. R., and Chacko, T., 1989, The granulite uncertainty principle: Limitations on thermobarometry in granulites: The Journal of Geology, v. 97, n. 4, p. 435–450, https://doi.org/10.1086/629321

Geisler, T., Schaltegger, U., and Tomaschek, F., 2007, Re-equilibration of zircon in aqueous fluids and melts: Elements, v. 3, n. 1, p. 43–50, https://doi.org/10.2113/gselements.3.1.43

Gerdes, A., and Zeh, A., 2009, Zircon formation versus zircon alteration – New insights from combined U-Pb and Lu-Hf *in-situ* LA-ICP-MS analyses, and consequences for the interpretation of Archean zircon

from the Central Zone of the Limpopo Belt: Chemical Geology, v. 261, n. 3–4, p. 230–243, https://doi.org/10.1016/j.chemgeo.2008.03.005

Goscombe, B., Hand, M., Gray, D., and Mawby, J., 2003, The metamorphic architecture of a transpressional orogen: The Kaoko Belt, Namibia: Journal of Petrology, v. 44, n. 4, p. 679–711, https://doi.org/10.1093/petrology/44.4.679

He, Q., Zhang, S. B., and Zheng, Y. F., 2018, Evidence for regional metamorphism in a continental rift during the Rodinia breakup: Precambrian Research, v. 314, p. 414–427, https://doi.org/10.1016/j.precamres.2018.06.009

Henry, D. J., Guidotti, C. V., and Thomson, J. A., 2005, The Ti-saturation surface for low-to-medium pressure metapelitic biotites: Implications for geothermometry and Ti-substitution mechanisms: American Mineralogist, v. 90, n. 2–3, p. 316–328, https://doi.org/10.2138/am.2005.1498

Holdaway, M., 2000, Application of new experimental and garnet Margules data to the garnet-biotite geothermometer: American Mineralogist, v. 85, p. 881–892, https://doi.org/10.2138/am-2000-0701

Holdaway, M. J., 2001, Recalibration of the GASP geobarometer in light of recent garnet and plagioclase activity models and versions of the garnet-biotite geothermometer: American Mineralogist, v. 86, n. 10, p. 1117–1129, https://doi.org/10.2138/am-2001-1001

Holland, T., and Powell, R., 2003, Activity–composition relations for phases in petrological calculations: An asymmetric multicomponent formulation: Contributions to Mineralogy and Petrology, v. 145, p. 492–501, https://doi.org/10.1007/s00410-003-0464-z

——— 2011, An improved and extended internally consistent thermodynamic dataset for phases of petrological interest, involving a new equation of state for solids: Journal of Metamorphic Geology, v. 29, n. 3, p. 333–383, https://doi.org/10.1111/j.1525-1314.2010.00923.x

Hyndman, R. D., Currie, C. A., and Mazzotti, S. P., 2005, Subduction zone backarcs, mobile belts, and orogenic heat: GSA Today, v. 15, n. 2, p. 4–10, https://doi.org/10.1130/1052-5173(2005)015<4:SZBMBA>2.0.CO;2

Indares, A., White, R. W., and Powell, R., 2008, Phase equilibria modelling of kyanite-bearing anatectic paragneiss from the central Grenville Province: Journal of Metamorphic Geology, v. 26, n. 8, p. 815–836, https://doi.org/10.1111/j.1525-1314.2008.00788.x

Jelsma, H., McCourt, S., Perritt, S., and Armstrong, R., 2018, The geology and evolution of the Angolan shield, Congo craton, *in* Siegesmund, S., Basei, M. A. S., Oyhantçabal, P., and Oriolo, S., editors, Geology of Southwest Gondwana: Cham, Switzerland, Springer, Regional Geology Reviews, p. 217–239, https://doi.org/10.1007/978-3-319-68920-3_9

Jung, S., Brandt, S., Bast, R., Scherer, E. E., and Berndt, J., 2019, Metamorphic petrology of a high-T/low-P granulite terrane (Damara belt, Namibia) – Constraints from pseudosection modelling and high-precision Lu-Hf garnet-whole rock dating: Journal of Metamorphic Geology, v. 37, n. 1, p. 41–69, https://doi.org/10.1111/jmg.12448

Kelsey, D. E., and Hand, M., 2015, On ultrahigh temperature crustal metamorphism: Phase equilibria, trace element thermometry, bulk composition, heat sources, timescales and tectonic settings: Geoscience Frontiers, v. 6, n. 3, p. 311–356, https://doi.org/10.1016/j.gsf.2014.09.006

Kelsey, D. E., Clark, C., and Hand, M., 2008, Thermobarometric modelling of zircon and monazite growth in melt-bearing systems: Examples using model metapelitic and metapsammitic granulites: Journal of Metamorphic Geology, v. 26, n. 2, p. 199–212, https://doi.org/10.1111/j.1525-1314.2007.00757.x

Kinny, P. D., 1986, 3820 Ma zircons from a tonalitic Amitsoq gneiss in the Godthåb district of southern West Greenland: Earth and Planetary Science Letters: Earth and Planetary Science Letters, v. 79, n. 3–4, p. 337–347, https://doi.org/10.1016/0012-821X(86)90190-1

Kirkland, C. L., Smithies, R. H., Taylor, R. J. M., Evans, N., and McDonald, B., 2015, Zircon Th/U ratios in magmatic environs: Lithos, v. 212–215, p. 397–414, https://doi.org/10.1016/j.lithos.2014.11.021

Kleemann, U., and Reinhardt, J., 1994, Garnet – biotite thermometry revisited: The effect of Al^{IV} and Ti in biotite: European Journal of Mineralogy, v. 6, n. 6, p. 925–941, https://doi.org/10.1127/ejm/6/6/0925

Kleinhanns, I. C., Fullgraf, T., Wilsky, F., Nolte, N., Fliegel, D., Klemd, R., and Hansen, B. T., 2015, U–Pb zircon ages and (isotope) geochemical signatures of the Kamanjab Inlier (NW Namibia): Constraints on Palaeoproterozoic crustal evolution along the southern Congo craton, *in* Roberts, N. M. W., Van Kranendonk, M., Parman, S., Shirey, S., and Clift, P. D., editors, Continent formation through time. Geological Society, London, Special Publications, v. 389, p. 165–195, https://doi.org/10.1144/SP389.1

Korhonen, F. J., Saito, S., Brown, M., and Siddoway, C. S., 2010, Modeling multiple melt loss events in the evolution of an active continental margin: Lithos, v. 116, n. 3–4, p. 230–248, https://doi.org/10.1016/j.lithos.2009.09.004

Köstlin, E.C., ms, 1967, "The Geology of Part of the Kunene Basic Complex", Kaokoveld, South West Africa: Cape Town, South Africa, University of Cape Town, MSc Thesis, 92 p.

Koziol, A. M., and Newton, R. C., 1988, Redetermination of the anorthite breakdown reaction and improvement of the plagioclase-garnet-Al_2SiO_5-quartz geobarometer: American Mineralogist, v. 73, n. 3–4, p. 216–223.

Kröner, A., Rojas-Agramonte, Y., Hegner, E., Hoffmann, K.-H., and Wingate, M. T. D., 2010, SHRIMP zircon dating and Nd isotopic systematics of Palaeoproterozoic migmatitic orthogneisses in the Epupa Metamorphic Complex of northwestern Namibia: Precambrian Research, v. 183, n. 1, p. 50–69, https://doi.org/10.1016/j.precamres.2010.06.018

Kröner, A., Rojas-Agramonte, Y., Wong, J., and Wilde, S., 2015, Zircon reconnaissance dating of Proterozoic gneisses along the Kunene River of northwestern Namibia: Tectonophysics, v. 662, p. 125–139, https://doi.org/10.1016/j.tecto.2015.04.020

Kunz, B. E., Regis, D., and Engi, M., 2018, Zircon ages in granulite facies rocks: Decoupling from geochemistry above 850°C: ?: Contributions to Mineralogy and Petrology, v. 173, article number p. 26 https://doi.org/10.1007/s00410-018-1454-5

Ludwig, K. R., 2001, Squid 1.02: A user's manual: Berkeley Geochronology Centre: Special Publication, v. 2, p. 19.

——— 2003, Isoplot 3.00: A geochronological toolkit for microsoft excel: Berkeley Geochronology Centre, Special Publication, v. 4, p. 70.

Mayer, A., Hofmann, A. W., Sinigoi, S., and Morais, E., 2004, Mesoproterozoic Sm–Nd and U–Pb ages for the Kunene anorthosite complex of SW Angola: Precambrian Research, v. 133, n. 3–4, p. 187–206, https://doi.org/10.1016/j.precamres.2004.04.003

McCourt, S., Armstrong, R. A., Jelsma, H., and Mapeo, R. B. M., 2013, New U-Pb SHRIMP ages from the Lubango region, SW Angola: Insights into the Palaeoproterozoic evolution of the Angolan Shield, southern Congo Craton: Journal of the Geological Society, London, v. 170, p. 353–363, https://doi.org/10.1144/jgs2012-059

Menge, G. F. W., 1998, The antiformal structure and general aspects of the Kunene Complex, Namibia: Zeitschrift der Deutschen Geologischen Gesellschaft, p. 431–448, https://doi.org/10.1127/zdgg/149/1998/431

Nasdala, L., Hofmeister, W., Norberg, N., Martinson, J. M., Corfu, F., Dörr, W., Kamo, S. L., Kennedy, A. K., Kronz, A., Reiners, P. W., Frei, D., Kosler, J., Wan, Y., Götze, J., Häger, T., Kröner, A., and Valley, J. W., 2008, Zircon M257 - a homogeneous natural reference material for the ion microprobe U-Pb analysis of zircon: Geostandards and Geoanalytical Research, v. 32, n. 3, p. 247–265, https://doi.org/10.1111/j.1751-908X.2008.00914.x

Newton, R. C., and Haselton, H. T., 1981, Thermodynamics of the garnet—plagioclase—Al_2SiO_5—quartz geobarometer: New York, New York, Springer, Thermodynamics of Minerals and Melts, p. 131–147, https://doi.org/10.1007/978-1-4612-5871-1_7

Palin, R. M., Weller, O. M., Waters, D. J., and Dyck, B., 2016, Quantifying geological uncertainty in metamorphic phase equilibria modelling; a Monte Carlo assessment and implications for tectonic interpretations: Geoscience Frontiers, v. 7, n. 4, p. 591–607, https://doi.org/10.1016/j.gsf.2015.08.005

Perchuk, L., and Lavrent'eva, I. (1983).Experimental investigation of exchange equilibria in the system cordierite-garnet-biotite: New York, New York, Springer, Kinetics and Equilibrium in Mineral Reactions, p. 199–239

Powell, R., and Holland, T. J. B., 1988, An internally consistent dataset with uncertainties and correlations: 3. Application to geobarometry, worked examples, and a computer program: Journal of Metamorphic Geology, v. 6, n. 2, p. 173–204, https://doi.org/10.1111/j.1525-1314.1988.tb00415.x

Raith, M. M., Brandt, S., Sengupta, P., Berndt, J., John, T., and Srikantappa, C., 2016, Element mobility and behaviour of zircon during HT metasomatism of ferroan basic granulite at Ayyarmalai, South India: Evidence for polyphase Neoarchaean crustal growth and multiple metamorphism in the north-eastern Madurai Province: Journal of Petrology, v. 57, n. 9, p. 1729–1774, https://doi.org/10.1093/petrology/egw057

Robinson, P. R., Hollocher, K. T., Tracy, R. J., and Dietsch, C. W., 1982, High grade Arcadian regional metamorphism in south-central Massachusetts, *in* Joesten, R., and Quarrier, S. S., editors, Guidebook for Fieldtrips in Connecticut and South-Central Massachusetts: NEIGC 74th Annual Meeting of the State Geological and Natural History Survey of Connecticut, University of Connecticut, Storrs, Connecticut, p. 289–339, https://doi.org/10.1007/978-1-4612-5587-1_7

Rubatto, D., and Gebauer, D., 2000, Use of cathodoluminescence for U–Pb zircon dating by ion microprobe: Some examples from the Western Alps, *in* Pagel, M., Barbin, V., Blanc, P., and Ohnenstetter, D., editors, Cathodoluminescence in Geosciences: Heidelberg, Springer, p. 373–400, https://doi.org/10.1007/978-3-662-04086-7_15

Rubatto, D., Williams, I. S., and Buick, I. S., 2001, Zircon and monazite response to prograde metamorphism in the Reynolds Range, central Australia: Contributions to Mineralogy and Petrology, v. 140, p. 458–468, https://doi.org/10.1007/PL00007673

Schaltegger, U., Fanning, C. M., Günther, D., Maurin, J. C., Schulmann, K., and Gebauer, D., 1999, Growth, annealing and recrystallization of zircon and preservation of monazite in high-grade metamorphism: conventional and *in-situ* U–Pb isotope, cathodoluminescence and microchemical evidence: Contributions to Mineralogy and Petrology, v. 134, p. 186–201, https://doi.org/10.1007/s004100050478

Seth, B., Armstrong, R. A., Brandt, S., Villa, I. M., and Kramers, J. D., 2003, Mesoproterozoic U–Pb and Pb–Pb ages of granulites in NW Namibia: Reconstructing a complete orogenic cycle: Precambrian Research, v. 126, n. 1–2, p. 147–168, https://doi.org/10.1016/S0301-9268(03)00193-1

Taylor, R. J. M., Kirkland, C. L., and Clark, C., 2016, Accessories after the facts: Constraining the timing, duration and conditions of high-temperature metamorphic processes: Lithos, v. 264, p. 239–257, https://doi.org/10.1016/j.lithos.2016.09.004

Trompette, R., 1994, Geology of Western Gondwana (2000–500 Ma). Pan-African-Brasiliano Aggregation of South America and Africa: Rotterdam, The Netherlands, Balkema, 350 p.

Vavra, G., Gebauer, D., Schmid, R., and Compston, W., 1996, Multiple zircon growth and recrystallization during polyphase Late Carboniferous to Triassic metamorphism in granulites of the Ivrea Zone (Southern Alps): An ion microprobe (SHRIMP) study: Contributions to Mineralogy and Petrology, v. 122, p. 337–358, https://doi.org/10.1007/s004100050132

White, R. W., Powell, R., and Clarke, G. L., 2002, The interpretation of reaction textures in Fe-rich metapelitic granulites of the Musgrave Block, central Australia: Constraints from mineral equilibria calculations in the system K_2O-FeO-MgO-Al_2O_3–SiO_2–H_2O-TiO_2–Fe_2O_3: Journal of Metamorphic Geology, v. 20, n. 1, p. 41–55, https://doi.org/10.1046/j.0263-4929.2001.00349.x

White, R. W., Powell, R., and Holland, T. J. B., 2007, Progress relating to calculation of partial melting equilibria for metapelites: Journal of Metamorphic Geology, v. 25, n. 5, p. 511–527, https://doi.org/10.1111/j.1525-1314.2007.00711.x

White, R. W., Powell, R., and Johnson, T. E., 2014a, The effect of Mn on mineral stability in metapelites revisited: New *a-x* relations for manganese-bearing minerals: Journal of Metamorphic Geology, v. 32, n. 8, p. 809–828, https://doi.org/10.1111/jmg.12095

White, R. W., Powell, R., Holland, T. J. B., Johnson, T. E., and Green, E. C. R., 2014b, New mineral activity-composition relations for thermodynamic calculations in metapelitic systems: Journal of Metamorphic Geology, v. 32, n. 8, p. 261–286, https://doi.org/10.1111/jmg.12071

Whitney, D. L., and Evans, B. W., 2010, Abbreviations for names of rock-forming minerals: American Mineralogist, v. 95, n. 1, p. 185–187, https://doi.org/10.2138/am.2010.3371

Williams, I. S., 1998, U-Th-Pb geochronology by ion microprobe, *in* McKibben, M. A., Shanks, W. C. III, and Ridley, W. I., editors, *Applications of Microanalytical Techniques to Understanding Mineralizing Processes: Reviews in Economic Geology*, v. 7, p. 1–35, https://doi.org/10.5382/Rev.07.01

Wu, C.-M., Zhang, J., and Ren, L.-D., 2004, Empirical garnet-biotite-plagioclase-quartz (GBPQ) geobarometry in medium- to high-grade metapelites: Journal of Petrology, v. 45, n. 9, p. 1907–1921, https://doi.org/10.1093/petrology/egh038

Yakymchuk, C., and Brown, M., 2014, Behaviour of zircon and monazite during crustal melting: Journal of the Geological Society, London, v. 171, n. 4, p. 465–479, https://doi.org/10.1144/jgs2013-115

Zheng, Y.-F., and Chen, R.-X., 2017, Regional metamorphism at extreme conditions: Implications for orogeny at convergent plate margins: Journal of Asian Earth Sciences, v 145, p. 46–73, https://doi.org/10.1016/j.jseaes.2017.03.009